Characterization of the Effect of Dopamine on the Neural Coding of Reward-Based Learning and Decision-Making

Angela M Ianni

Merton College
University of Oxford

A thesis submitted for the degree of Doctor of Philosophy

Trinity 2017

Abstract

Dopamine has an important role in normal cognition and reward processing, both of which are impaired in disorders involving dopamine dysfunction such as addiction, schizophrenia, and Parkinson's disease. However, our understanding of the interplay between different aspects of the dopamine system and reward-guided behavior in humans is limited. Food is an important type of reward that is critical for survival and impacts the decisions we make every day. Here, we characterize the relationship between two food-reward related phenotypes and dopamine synthesis capacity (related to tonic dopamine) as well as dopamine D_1 and D_2 receptor availability in healthy humans.

First, we examined the link between dopamine synthesis and receptor availability and body mass regulation in 117 individuals with body mass index (BMI) values ranging from normal to obese. We found that current BMI was related to a pattern of increased dopamine synthesis in the hypothalamus, a region important for homeostatic control of appetite, but decreased dopamine D_2 receptor availability in the midbrain, where D_2 autoreceptors regulate dopamine release throughout the brain. This suggests that increased BMI is related to a dopamine imbalance between homeostatic drivers of appetite and reward system regulatory control mechanisms that could result in an overactive, unregulated intake of food.

Building on this finding, we studied the link between dopamine synthesis capacity and receptor availability and an important food-reward related behavior, foraging. Fifty-seven healthy volunteers completed a computer-based foraging task where we measured their threshold for leaving one group of rewards to search for another in four different reward environments varying from a low to high rate of reward receipt. We found that two particular patterns of dopamine synthesis and receptor availability in the anterior cingulate cortex and basal ganglia were linked to the amount that individuals changed their threshold based on the reward rate of the environment.

Finally, since the prefrontal cortex is known to be important for reward-guided behavior, we implemented two methodological advancements aimed to address limitations that make it difficult to measure cortical dopamine in humans with PET imaging. The first method involves partial volume correction and surface-based smoothing in order to increase the signal to noise in the cortex. The second method is a data-driven PET data parcellation and automated reference region selection algorithm to optimize the voxels included in the reference region.

In conclusion, we have characterized the dopaminergic contribution of two different food-reward guided phenotypes and have developed two techniques that will aid future research on the role of cortical dopamine. Understanding the neural mechanisms underlying these reward-guided behaviors helps us to not only understand normal behavior, but also serves as a reference for comparison when studying related pathological states.

Characterization of the Effect of Dopamine on the Neural Coding of Reward-Based Learning and Decision-Making



Angela M Ianni

Merton College
University of Oxford

A thesis submitted for the degree of
Doctor of Philosophy

Trinity 2017

Acknowledgements

Personal

First of all, I must acknowledge the amazing amount of support that my family has given me during the course of my DPhil studies. My husband, Andrew, provided endless emotional support in addition to being an amazing and very involved father to our daughter, Ilaria, who was born in March of 2016. My parents and in-laws have also been essential during this time as they have generously helped to take care of Ilaria while Andrew and I completed our studies. I also need to thank Ilaria herself for the constant smiles and love that she provides daily as well as her tendency to sleep through the night from a very early age.

Second, I would like to thank my two wonderful DPhil mentors, Tim Behrens and Karen Berman for their guidance and support over the past four years. Both Tim and Karen have taught me the invaluable skills needed to become an independent researcher such as how to formulate research questions and projects that logically follow from the current body of knowledge and how to effectively present my work at scientific meetings. In addition, they have both been extremely understanding and accommodating for my seemingly constant journeys over the pond moving between Oxford and the NIH as well as my decision to start a family in the middle of my PhD. I honestly could not have asked for better mentors.

Finally, the work contained in this thesis would not be possible without my wonderful research families in both of these labs. Specifically, Daniel Eisenberg at the NIH and Erie Boorman in Oxford have helped me out tremendously as secondary mentors. In addition, all of the other graduate students, senior researchers, post-docs, and research assistants in both labs have helped in one way or another by assisting with data collection, engaging in wonderful scientific discussions, and providing moral support along the way. When I started this collaborative DPhil program and knew that I had to split my time between Oxford and the NIH, I worried that I would feel like a visitor in each lab. However, my experience has been the exact opposite and I feel blessed to be part of two amazing groups of scientists.

Institutional

I am extremely grateful for the opportunities that I have been presented with through the NIH MD/PhD Partnership Training Program. Being a part of this program has allowed me to pursue my passion for both helping individual people as a physician and helping advance the field as a researcher. Along the same lines, I am also very thankful to the University of California San Diego Medical Scientist Training Program for their acceptance and support during the medical training as well as the NIH Oxford-Cambridge Scholars Program, the National

Institutes of Health, and The University of Oxford for the excellent research training. All of these institutions have invested in my training in many ways in addition to the financial support that they have provided.

The data included here was supported by the Intramural Research Program, National Institute of Mental Health, National Institutes of Health, Bethesda, MD, 20892. In addition, I would like to thank the staff of the NIH PET Center and the staff of the Clinical and Translational Neuroscience Branch for their assistance in data acquisition.

Technical

This work (especially Section 6.3) utilized the computational resources of the NIH HPC Biowulf supercomputing cluster (http://hpc.nih.gov). Numerous software packages were essential to this work including Matlab (www.mathworks.com) for the model-fitting and generation of many of the figures contained in this document, FSL (www.fmrib.ox.ac.uk/fsl), SPM (www.fil.ion.ucl.ac.uk/spm), and AFNI (https://afni.nimh.nih.gov) for general image analysis tools, and Freesurfer (https://surfer.nmr.mgh.harvard.edu/) and SUMA (https://afni.nimh.nih.gov/Suma) for surface-based image analysis. Lastly, many people have provided technical support including my mentors and lab mates mentioned above as well as the Wellcome Centre For Integrative Neuroimaging (formerly known as FMRIB) for the MRI physics and image analysis training through the FMRIB Graduate Programme.

Table of Contents

List of Figures viii

List of Tables xi

List of Abbreviations xii

1. Introduction 1
1.1 Motivation 1
1.2 Thesis Contribution and Structure 3
1.3 Originality and Individual Role 5
1.4 Prior Publications 6

2. Background 8
2.1 Introduction 8
2.2 Reward-Guided Behavior 9
2.2.1 Types of Reward-Guided Behavior 9
2.2.2 Neural Circuitry Underlying Reward-Guided Behavior 10
2.3 The Dopamine System 12
2.3.1 Basic Biology of the Dopamine System 12
2.3.2 Types of Dopamine Receptors 14
2.3.3 Tonic vs. Phasic Dopamine 14
2.4 Role of Dopamine in Reward-Guided Behavior 15
2.4.1 Reward Prediction Errors and Associative Learning 16
2.4.2 Tonic Dopamine and Average Reward Rate 18
2.4.3 Role of D_1 and D_2 Dopamine Receptors 19
2.4.4 Dopamine and Food-Related Behavior 20

3. Methods for Measuring Dopamine Synthesis and Receptor Availability in Humans 21
3.1 Introduction 21
3.2 Positron Emission Tomography 22
3.3 PET Tracers of the Dopamine System 23
3.4 PET Data Acquisition 25
3.5 PET Data Analysis 26

4. Dopamine Synthesis and Receptor Profile Are Associated with Body Mass Index in Humans 30
4.1 Introduction 31
4.2 Experimental Procedures 34
4.2.1 Participants 34
4.2.2 BMI Quantification 35
4.2.3 Imaging Data Acquisition 36
4.2.4 Imaging Data Analysis 36
4.3 Results 37
4.3.1 Demographics and Effects of Age and Gender 37
4.3.2 Dopaminergic PET Correlations with Current BMI 39
4.3.3 Dopaminergic PET Associations with Prior BMI Change 41

4.4 Discussion 43

5. Dopamine Synthesis and Receptor Profile Association with Foraging Behavior in Humans 48
5.1 Introduction 49
5.1.1 Marginal Value Theorem 50
5.1.2 Neural Circuit Implicated in Foraging Behavior 51
5.1.3 Implication of Dopamine in Foraging Behavior 53
5.1.4 Dissociation of Neural Mechanisms Encoding Reward Timing and Magnitude 55
5.2 Methods 56
5.2.1 Study Participants 56
5.2.2 Patch Foraging Behavioral Task 56
5.2.3 Behavioral Measures of Interest 58
5.2.4 PET Imaging Methods 59
5.2.5 Principal Component Analysis of PET Data 59
5.2.6 Statistical Analyses 60
5.3 Results 62
5.3.1 Behavioral Results 62
5.3.2 PET Data PCA Results 63
5.3.3 Correlations Between Foraging Behavior and Dopamine PET Data Principal Components 65
5.3.4 Correlations Between Total Change in Patch Leaving Threshold and Individual Dopamine PET Tracer Data 67
5.4 Discussion 70

6. Limitations and Development of PET Methods 75
6.1 Introduction 76
6.1.1 Limitations of Cortical PET Data 76
6.1.2 Partial Volume Effects 77
6.2 Surface-Based PET Imaging Methods 79
6.2.1 Introduction 79
6.2.2 Methods 80
6.2.3 Results 86
6.2.4 Discussion 89
6.3 Data-Driven PET Parcellation: Application for Automated Optimal Reference Region Delineation 91
6.3.1 Introduction 91
6.3.2 Methods 94
6.3.3 Results 101
6.3.4 Discussion 115
Chapter 6 Appendix 120
A. Surface Smoothing and Partial Volume Correction Additional Results. 120
B. Example Voxel Model-Fitting Additional Results 120

7. Future Work 125
7.1 Overview of Future Work 125

7.2 Optimization and Implementation of PET Methodological Advancements 126
7.3 Validation of Dopamine PCA Results 128
7.4 Role of Dopamine in Other Types of Reward-Guided Behavior..... 130

Conclusions..... 131

Appendices..... 137
A. Partial Volume Correction Methods for PET Data Analysis **..... 138**
A.1 Geometric Transfer Matrix Methods for Partial Volume Correction of Region of Interest Data 138
A.2 "Modified" Muller-Gartner Algorithm for Partial Volume Correction of Voxelwise Data..... 140
B. Validity of Simplified Reference Tissue Model (SRTM) for Calculating [^{11}C]-NNC112 and [^{18}F]-Fallypride BP_{ND} **..... 143**
B.1 Assumptions of the SRTM Model 143
B.2 Validity of the SRTM Model for [^{11}C]-NNC112..... 146
B.3 Validity of the SRTM Model for [^{18}F]-Fallypride 147

References..... 150

List of Figures

Figure 1: Schematic of brain regions involved in reward-guided behavior..... 12
Figure 2: Schematic of the dopamine pathways in the brain. 12
Figure 3: Reward prediction error signal in midbrain dopamine neurons..... 17
Figure 4: Depiction of the decay of a radiopharmaceutical and subsequent annihilation event. 22
Figure 5: Schematic of dopamine synapse and commonly used PET radioligands. 24
Figure 6. Schematic of a two-tissue reference region model..... 27
Figure 7: Native-space basal ganglia regions of interest. 28
Figure 8: Negative correlation between current BMI and D_2 receptor BP_{ND} in the dopaminergic midbrain (r=-0.341, p=0.008). 40
Figure 9: Positive correlation between current BMI and dopamine presynaptic synthesis capacity in the bilateral hypothalamus..... 40
Figure 10: Increased dopamine synthesis capacity in individuals who gained weight compared to those who lost weight prior to the PET scan in the ventral striatum and midbrain. 42
Figure 11. ACC neural activity in non-human primates during foraging..... 51
Figure 12. ACC BOLD fMRI activation associated with the search value of the foraging environment. 52
Figure 13: Schematic of patch foraging task. 58
Figure 14: Anterior cingulate cortex region of interest. 59
Figure 15: Foraging Behavioral Results. 63
Figure 16: Correlation of behavioral sensitivity to change reward magnitude decay rate compared to change in travel time (r=0.137, p=0.314)..... 64
Figure 18: Results of dopamine PCA analysis. 65
Figure 19: Component correlations with total change in patch leaving threshold 66
Figure 20: Correlation between component 1 and change in exit threshold due to travel time changes and decay rate changes. 67
Figure 21. Positive correlations between [^{18}F]-FDOPA K_i and total change in exit threshold. 68
Figure 22. Trend towards positive correlation between [^{18}F]-FDOPA K_i in the ACC (-2,40,16) and total change in patch leaving threshold ($p_{uncorrected}$=0.0086). 68
Figure 23. Positive correlations between total change in patch leaving threshold and D_2 receptor availability in the putamen, caudate nucleus, and left OFC (circled). 69
Figure 24. Positive correlations between total change in patch leaving threshold and D_1 receptor availability in regions including the bilateral ventral striatum and OFC (circled). 70
Figure 25: Schematic of cortical sampling along the middle 80% of the cortical ribbon. 82
Figure 26: Schematic of the compared PET methods. 83

Figure 27: Cortical regions of interest in standard surface space. 84
Figure 28: Cortical regions in 3D volumetric space. 85
Figure 29. Effects of partial volume correction (PVC). 86
Figure 30. Effects of surface smoothing and PVC on parameter values and CoV in the DLPFC 88
Figure 33: Example error weighting vector for one subject for an [^{18}F]-FDOPA scan. 96
Figure 34: Large cerebellum mask to spatially constrain voxel selection. 97
Figure 35: Schematic of the distance metric assignment for each of the three fitted parameters. 99
Figure 36: Example T1 MRI images for (a) cohort 1 (good quality) and (b) cohort 2 (poor quality) 100
Figure 37: [^{18}F]-FDOPA whole brain map of α values (rate of tracer uptake) for example subject. 103
Figure 38: [^{11}C]-NNC112 whole brain map of α values (rate of tracer uptake) for example subject. 103
Figure 39: [^{18}F]-Fallypride whole brain map of α values (rate of tracer uptake) for example subject. 104
Figure 41: [^{11}C]-NNC112 whole brain map of β values (rate of tracer decay) for example subject. 105
Figure 42: [^{18}F]-Fallypride whole brain map of β values (rate of tracer decay) for example subject. 105
Figure 43: [^{18}F]-FDOPA whole brain map of γ values (maximal tracer uptake) for example subject. 106
Figure 44: [^{11}C]-NNC112 whole brain map of γ values (maximal tracer uptake) for example subject. 106
Figure 45: [^{18}F]-Fallypride whole brain map of γ values (maximal tracer uptake) for example subject. 107
Figure 46: Model-fitting results from example voxels for one subject (all three PET tracers: a. location of example voxels, b. [^{18}F]-FDOPA, c. [^{11}C]-NNC112, d. [^{18}F]-Fallypride). Additional images with actual data and model fits are in Chapter 6 Appendix B 108
Figure 47: [^{18}F]-FDOPA histogram of parameter values for an example subject. 109
Figure 48: [^{11}C]-NNC112 histogram of parameter values for an example subject. 110
Figure 49: [^{18}F]-Fallypride histogram of parameter values for an example subject. 110
Figure 50: [^{18}F]-FDOPA tracer example reference regions of various sizes ranging from 3,000 (red) to 15,000 (blue) for example subject, unconstrained (whole-brain). 111
Figure 51: [^{18}F]-FDOPA tracer example reference regions of various sizes ranging from 3,000 (red) to 15,000 (blue) for example subject, constrained to the cerebellum with a spatial mask. 111

Figure 52: [^{11}C]-NNC112 tracer example reference regions of various sizes ranging from 3,000 (red) to 15,000 (blue) for example subject, unconstrained (whole-brain). 111
Figure 53: [^{11}C]-NNC112 tracer example reference regions of various sizes ranging from 3,000 (red) to 15,000 (blue) for example subject, constrained to the cerebellum with a spatial mask. 111
Figure 54: [^{18}F]-Fallypride tracer example reference regions of various sizes ranging from 3,000 (red) to 15,000 (blue) for example subject, unconstrained (whole-brain). 112
Figure 55: [^{18}F]-Fallypride tracer example reference regions of various sizes ranging from 3,000 (red) to 15,000 (blue) for example subject, constrained to the cerebellum with a spatial mask. 112
Figure 56: Individuals with good quality MRI scans: intraclass correlation coefficient (ICC) values for [^{18}F]-FDOPA putamen K_i values for all methods tested. 113
Figure 57: Individuals with good quality MRI scans: Absolute percent difference (APD) mean values and standard error for [^{18}F]-FDOPA putamen K_i values for all methods tested. 113
Figure 58: Individuals with good quality MRI scans: Standard error of measurement (SEM) for [^{18}F]-FDOPA putamen K_i values for all methods tested. 114
Figure 59: Test-retest metrics for individuals with poor quality MRI scans. 115
Figure 60. Effects of surface smoothing and PVC on parameter values and CoV in the ACC. 121
Figure 61. Effects of surface smoothing and PVC on parameter values and CoV in the OFC. 122
Figure 62. Effects of surface smoothing and PVC on mean values and CoV in occipital cortex. 123
Figure 63. Data and model-fitting results for an example subject. 124
Figure 64. Compartment model for SRTM method 144
Figure 65. Correlation between SRTM and MRTM methods for [^{11}C]-NNC112. 147
Figure 66. Correlation between SRTM and MRTM methods for [^{18}F]-Fallypride. 149

List of Tables

Table 1: BMI Analysis Participant Demographics 38
Table 2: BMI Analysis Region of Interest Results* 39
Table 3: BMI Analysis Voxelwise Results* 39

List of Abbreviations

AADC	.....	Aromatic amino acid decarboxylase
ACC	.....	Anterior cingulate cortex
APD	.....	Absolute percent difference
BMI	.....	Body mass index
BOLD	.....	Blood-oxygen-level dependent (refers to functional MRI signal of brain activity)
BP_{ND}	.....	Non-displaceable binding potential, related to receptor availability (PET measure for [^{11}C]-NNC112 and [^{18}F]-Fallypride)
CSF	.....	Cerebrospinal fluid
CoV	.....	Coefficient of variation
DLPFC	.....	Dorsolateral prefrontal cortex
fMRI	.....	Functional magnetic resonance imaging
GPCR	.....	G-protein coupled receptor
ICC	.....	Intraclass correlation coefficient
K_i	.....	Specific uptake rate (PET measure for [^{18}F]-FDOPA)
MG	.....	Muller-Gartner (algorithm for voxelwise partial volume correction of PET data)
MVT	.....	Marginal value theorem
OFC	.....	Orbitofrontal cortex
PCA	.....	Principal component analysis
PET	.....	Positron emission tomography
PSF	.....	Point spread function (related to spatial resolution of a PET scanner)
PVC	.....	Partial volume correction
ROI	.....	Region of interest
RPE	.....	Reward prediction error
SEM	.....	Standard error of measurement
SN	.....	Substantia nigra
SRTM	.....	Simplified reference tissue model
vmPFC	.....	Ventromedial prefrontal cortex
VTA	.....	Ventral tegmental area

1

Introduction

Contents

1.1 Motivation
1.2 Thesis Contribution and Structure
1.3 Originality and Individual Role
1.4 Prior Publications

1.1 Motivation

Human behavior is heavily influenced by the drive to attain rewards. Primary rewards, which are necessary for survival (e.g. food and reproduction), are inherently valuable to the brain's reward system. Other rewards, however, gain value through learning from experience. Learning of value occurs when decisions are made and outcomes are observed and compared to personal expectations. In addition to the value of individual actions or cues themselves, other aspects of the environment as a whole as well as the state of the individual can greatly influence reward-guided behavior. For example, food rewards may have heightened value when hungry compared to satiated. In addition, the optimal strategy to forage for food rewards varies depending on the average rate at which rewards are received in a given environment [1].

The neuromodulator dopamine has an important role in the neural coding of value that is required for reward-based learning [2, 3]. In addition, disorders involving perturbations in the dopamine system such as Parkinson's disease, schizophrenia, and addiction result in specific reward-guided behavioral deficits [4-6]. While previous studies have examined the role of dopamine in reward-guided behavior [7-9], they typically investigate only one aspect of the dopamine system at a time (e.g. genetic variation in dopamine-related genes, dopamine D_2 receptors, dopamine presynaptic synthesis capacity, etc.), potentially because of the challenge and cost of collecting multiple measures in the same individuals. Furthermore, knowledge of dopamine's role in the neural network controlling food-seeking behavior, a reward-guided behavior that is crucial for survival, is limited. Lastly, although the prefrontal cortex is known to be essential for reward-guided learning and decision-making [10-12], we lack an understanding of the role of cortical dopamine in reward-guided behavior due to the methodological limitations of measuring cortical dopamine in humans. Therefore, quantitative description of the neural circuit involved in food-seeking behavior, including a comprehensive measurement of various aspects of dopamine function, is important for understanding how perturbations affect the system and may provide a framework in the search for biomarkers for disease and response to treatment. In addition, methodological improvements for measuring cortical dopamine in humans are needed to evaluate the role of both subcortical and cortical dopamine in reward-guided behavior.

1.2 Thesis Contribution and Structure

The contribution of this thesis is threefold. First, I explore the role of dopamine synthesis and receptor availability on body mass regulation, a phenotype that is directly related to food-reward based behavior (**Chapter 4**). Specifically, I measure correlations with body mass index and three aspects of dopamine function: dopamine presynaptic synthesis capacity along with dopamine D_1 and D_2 receptor availability. This is the largest study to examine the dopaminergic bases of increased body mass in humans and the first to look at it from a three-pronged approach (dopamine synthesis plus D_1 and D_2 receptor availability).

Next, I quantify the relationship between dopamine function and foraging behavior, which drives food-seeking decisions in many natural settings (**Chapter 5**). Specifically, I use a principal component analysis to reduce the dimensionality of the three-scan dopamine PET data into four patterns of variation. I then examine how those patterns of dopamine variation are related to changes in foraging behavior that occur due to changes in the reward environment (time it takes to get from one group of rewards to another and how quickly each group of rewards depletes).

Lastly, I identify limitations in the current methods available for measuring dopamine in vivo in humans and present two different methods that I've developed to improve the signal of PET imaging data in the prefrontal cortex in order to fill the gap in knowledge on the role of cortical dopamine in various aspects of reward-guided behavior (**Chapter 6**). These methodological

advancements target two aspects of PET image analysis that should theoretically improve the signal to noise ratio of the data.

The first method is a cortical surface-based data processing pipeline that reduces loss of valuable cortical signal into the surrounding cerebral spinal fluid and white matter (**Section 6.2**). In that section, I describe the pipeline for sampling the PET data to the cortical surface and performing 2D spatial smoothing along the surface, along with applying partial volume correction methods. The resulting data are compared to the typical 3D volume-smoothed PET data processing pipeline by calculating metrics such as the mean parameter value and the coefficient of variation in various cortical regions of interest (dorsolateral PFC, orbitofrontal cortex, anterior cingulate cortex, and occipital cortex).

The second method aims to improve the PET parameter model-fitting procedure by optimizing the voxels selected for the reference region (**Section 6.3**). The PET timecourse data at each voxel are fit to a descriptive model with three parameters: total amount of tracer uptake, rate of tracer uptake, and rate of tracer decay. An algorithm I developed for using these three parameters to automatically select an ideal reference region is described. Lastly, this method is compared to other reference region selection methods by calculating test-retest metrics for a group of individuals who completed one of our PET scans at two separate times. The test-retest comparison of reference region methods was done for both healthy volunteer data who had high-quality MRI scans collected by our group as well as data from patients with Gaucher's disease and their

relatives with poor-quality MRI scans collected by a collaborator's group. Also highlighted in this chapter are other potential advantages of this method such as eliminating the need to acquire an MRI scan for manual reference region delineation and the potential for defining image-derived arterial input functions.

1.3 Originality and Individual Role

This thesis contains my original work; however, many collaborators helped with various aspects of the projects presented. For the methods-related chapters, all data processing and computer coding are my own work. PET and behavioral data collection was done by myself and numerous colleagues in Karen Berman's lab. All PET parameter modeling and basic preprocessing of dicom images were a collaborative effort with a group of individuals in Karen Berman's lab including Daniel Eisenberg, Philip Kohn, and Catherine Hegarty. In addition to the ongoing advice of my direct mentors, Karen Berman and Tim Behrens, various collaborators helped with certain aspects of the work contained here. Specifics are listed below.

Chapter 4 All analyses were done by myself. Body mass index data was collected by NIH clinical center staff and queried from the electronic medical record by myself.

Chapter 5 The computer-based patch foraging task was developed by a collaborator, Sara Constantino, who shared her code with me and gave her permission to collect data. Data analysis was completed by myself. Discussion of analyses and results along with feedback on poster presentations was

provided by Tim Behrens, Karen Berman, Erie Boorman, Sara Constantino, and Daniel Eisenberg.

Chapter 6, Section 6.2 The methods described in this chapter were developed by myself, based on published literature and consultation with collaborators. Specifically, Daniel Eisenberg provided ongoing advice throughout all stages of the project. Shane Kippenhan helped with implementing the surface-sampling and smoothing methods.

Chapter 6, Section 6.3 All code, written in Matlab, was generated by myself. Tim Behrens helped me to come up with the descriptive model to which the PET time-activity data was fit. Michael Gregory helped to get the code running on the NIH supercomputing cluster (biowulf). Daniel Eisenberg provided ongoing advice.

Authorship This document is my original work and I am the sole author. All figures were produced by me, unless otherwise noted in the caption citation. Feedback and edits were provided by Karen Berman, Tim Behrens, Daniel Eisenberg, and Andrew Gerlach.

1.4 Prior Publications

Much of the work presented in this thesis is currently being prepared for publication. In addition, preliminary analyses have been presented at numerous conferences, the specifics of which are listed below.

The work presented in Chapter 4, Dopamine Synthesis and Receptor Profile are Associated with Body Mass Index in Humans, has already been prepared for publication and is undergoing final edits prior to submission.

In addition, manuscripts for the results presented in Chapter 5, Dopamine Synthesis and Receptor Profile Association with Foraging Behavior in Humans, and the method described in Section 6.3, Data-Driven PET Parcellation: Application for Automated Optimal Reference Region Definition, are both currently being prepared.

The work described in Chapter 5 has been presented as an oral presentation at the Computational Psychiatry Satellite Meeting associated with the Society for Biological Psychiatry Annual Meeting in May 2017.

Lastly, preliminary analyses of the data contained in Chapters 4 and 5 have been presented as posters at a number of conferences:

Chapter 4: Organization for Human Brain Mapping (2015, travel award), Molecular Psychiatry Meeting (2015, travel award), and American College of Neuropsychopharmacology (2015)

Chapter 5: The Multi-Disciplinary Conference on Reinforcement Learning and Decision Making (2015, travel award), Society of Biological Psychiatry (2016, travel award, 2017), and American College of Neuropsychopharmacology (2016)

2

Background

Contents

2.1 Introduction
2.2 Reward-Guided Behavior
  2.2.1 Types of Reward-Guided Behavior
  2.2.2 Neural Circuitry Underlying Reward-Guided Behavior
2.3 The Dopamine System
  2.3.1 Basic Biology of the Dopamine System
  2.3.2 Types of Dopamine Receptors
  2.3.3 Tonic vs. Phasic Dopamine
2.4 Role of Dopamine in Reward-Guided Behavior
  2.4.1 Reward Prediction Errors and Associative Learning
  2.4.2 Tonic Dopamine and Average Reward Rate
  2.4.3 Role of D_1 and D_2 Dopamine Receptors
  2.4.4 Dopamine and Food-Related Behavior

2.1 Introduction

This chapter provides an overview of the concepts that are discussed throughout this document. First is an introduction to the different types of reward-guided behavior and what is known about the underlying neural circuitry. Next is a description of the dopamine system from the basic biology to the types of receptors and release patterns. Third, the core concepts that are well known about dopamine's role in reward-guided behavior are introduced including reward

prediction errors, the role of tonic dopamine, and differential effects of dopamine D_1 and D_2 receptors.

2.2 Reward-Guided Behavior

2.2.1 Types of Reward-Guided Behavior

All animals that can move must weigh the associated costs and dangers of leaving home with the potential benefits in order to survive. This is the way that animals evolved, and only those who could successfully find food and reproductive partners survived. The basic processes that promoted survival and reproduction are likely the same ones that guide our everyday decisions [13]. From an evolutionary standpoint, a very important reward-guided behavior that is critical for survival is foraging, where animals make decisions about whether to keep searching for rewards (food or reproductive mates) in their current environment, or leave and search elsewhere.

Another essential reward-guided behavior for learning about the newly encountered environment is associative learning. One mechanism for associative learning to occur is via Pavlovian conditioning in which neutral stimuli are paired with rewards, causing the neutral stimuli to evoke the same innate response originally isolated to the reward itself. Instrumental conditioning is another form of associative learning in which an animal learns which actions it takes are more likely to result in rewards. Here, the action itself gains the value of the resulting reward. Associative learning requires an ability to credit an outcome with a specific stimulus or action that caused it. This precise credit

assignment can be difficult in the real world when rewards may not always immediately follow a cue or action in time, or when multiple cues and actions are encountered in quick succession. For this reason, the brain has numerous mechanisms for assigning credit at various levels of precision [14, 15].

2.2.2 Neural Circuitry Underlying Reward-Guided Behavior

Due to its role in a wide range of behaviors from movement to goal-directed action planning, there are many regions in the brain involved in reward-guided behavior including the striatum, midbrain dopamine neurons, orbitofrontal cortex (OFC), anterior cingulate cortex (ACC), ventral medial prefrontal cortex (vmPFC), dorsal lateral prefrontal cortex (DLPFC), amygdala, and hippocampus [16] (see **Figure 1**). The main process by which reward-guided behavior occurs is by first learning (through experience) to associate value to actions and stimuli. Subsequently, when it is time to make a decision or develop an action plan, the values and associations that were stored during the learning phase are evaluated and a decision is made. In addition, during foraging behavior when the choice is not between two or more actions or stimuli, but rather between either continuing to look for rewards in the current environment or leave and search elsewhere, the brain must also evaluate how good the current environment is and what the costs associated with searching would be.

We have learned a tremendous amount about the basics of the brain's reward circuit through rodent pharmacological and self-stimulation paradigms. In self-stimulation paradigms, first developed by Olds and Milner in 1954, rodents press a lever to stimulate an electrode in their brain [17]. Pharmacological

studies involve microinjections of a pharmaceutical into a specific region of the brain. Both of these methods have implicated the nucleus accumbens in the ventral striatum and the ventral tegmental area (VTA) in the midbrain as key hubs of the reward circuit [18-20]. The ventral striatum receives inputs from other subcortical regions including the amygdala and the hippocampus, regions that play an important role in emotion [21, 22] and the formation of an internal model of the reward environment [23].

Furthermore, cortical regions such as the OFC, vmPFC, and ACC also send strong afferent projections to the ventral striatum. This is important because these regions are implicated in crucial aspects of reward processing such as value encoding and comparison. Specifically, neural activity in the medial OFC and vmPFC reflects the reward value of choices and outcomes [24, 25]. In addition, the medial OFC has also been shown to focus attention on the relevant goal-directed decision [26]. The lateral OFC, on the other hand, is more involved in reward-guided learning and is essential for crediting outcomes to specific actions or stimuli [15, 24]. Lastly, the ACC plays a key role in integrating value and goal information into a choice. In comparative decision-making paradigms, neural activity in the ACC reflects the probability of selecting the correct choice [24, 27]. Furthermore, the ACC has also been implicated in encoding information about the reward environment such as volatility of changes in reward-associations [28] and the average value of the foraging environment [29, 30].

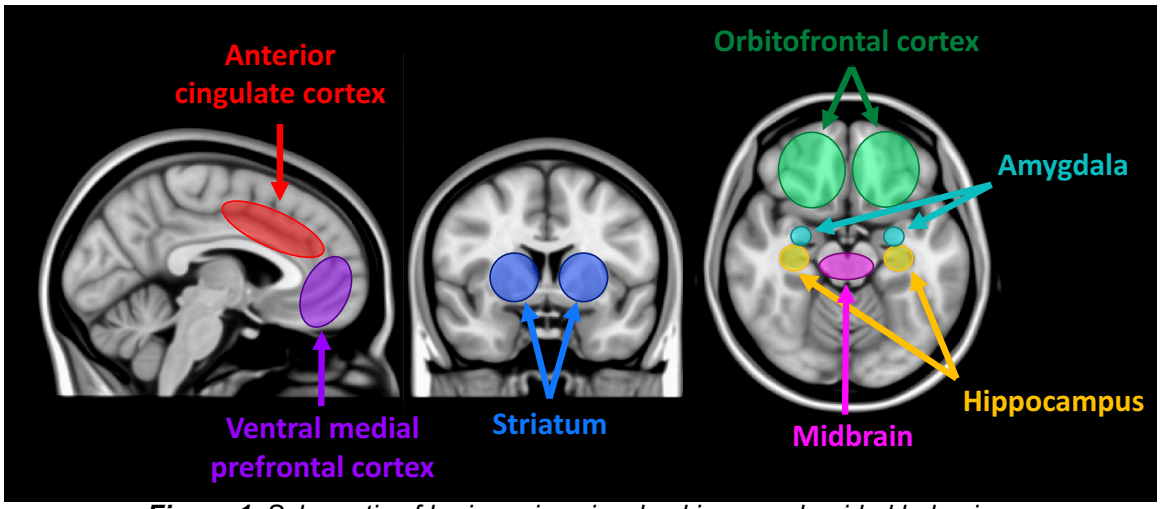


***Figure 1**: Schematic of brain regions involved in reward-guided behavior.*

2.3 The Dopamine System

2.3.1 Basic Biology of the Dopamine System

Dopamine is a neurotransmitter that belongs to the catecholamine family along with epinephrine and norepinephrine. As a neuromodulator, dopamine plays a role in regulating diverse populations of neurons and is important for a number of behaviors including movement, cognition, attention, and reward [31].

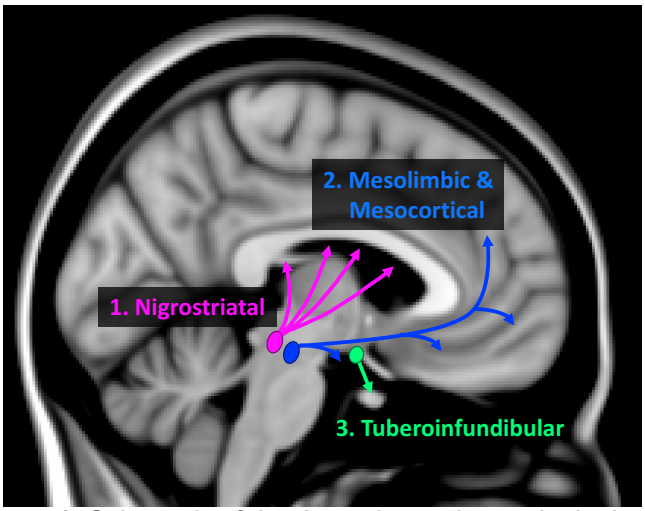


***Figure 2**: Schematic of the dopamine pathways in the brain.*

Dopaminergic cell bodies originate in the midbrain and hypothalamus. The midbrain cell bodies are located in the substantia nigra pars compacta (SN) and the VTA. Neurons originating in the SN primarily project to the caudate nucleus and putamen in the dorsal striatum, forming the nigrostriatal pathway that is essential for motor control. The neurons from the VTA innervate the nucleus accumbens in the ventral striatum, amygdala, hippocampus, hypothalamus, and prefrontal cortex, forming the mesolimbic and mesocortical pathways important for motivation, reward processing, and cognition. In addition, the tuberoinfundibular pathway consists of dopamine cell bodies originating in the hypothalamus that play a role in pituitary development and function (for reviews see [32], [33], and [34]). A schematic of the dopamine pathways in the brain is shown in **Figure 2**.

Dopamine exerts its effects through modulation of cortico-basal ganglia loops, which in turn also play a role in regulating the dopamine system [35-37]. Each functional region in the frontal cortex is connected to a specific region in the basal ganglia. For example, reward-based behaviors, which are known to be modulated by the mesolimbic dopamine pathway, are mediated by cortical regions including the ACC and OFC, which project to the ventral striatum. The ventral striatum, in turn, projects to the ventral pallidum, the VTA, and the SN [36]. Therefore, it is important to keep in mind that dopamine synthesis or receptor availability in the basal ganglia may in turn affect the entire cortico-basal ganglia reward network.

2.3.2 Types of Dopamine Receptors

There are five known types of dopamine receptors in the brain: D_1, D_2, D_3, D_4, and D_5. Dopamine receptors are G-protein-coupled receptors (GPCRs) divided into two main groups depending on their downstream effects. The D_1-like receptor group (D_1 and D_5) are G_s-coupled GCPRs and their activation results in an increase in intracellular levels of cAMP while the D_2-like receptor group (D_2, D_3, and D_4) are $G_{i\alpha}$-coupled GPCRs and their activation results in a decrease in intracellular cAMP. Of the D_1-like group, D_1 receptors are found in the striatum and neocortex while D_5 receptors are expressed in the hippocampus and hypothalamus [38]. For the D_2-like family, D_2 receptors are present in the striatum, substantia nigra and ventral tegmental area of the midbrain, the pituitary, and the neocortex, D_3 receptors are found in the nucleus accumbens, olfactory tubercle, and hypothalamus, and D_4 receptors are located in the frontal cortex, medulla, and midbrain [38].

2.3.3 Tonic vs. Phasic Dopamine

Dopamine neurons have two distinct firing modes: tonic and phasic [39]. The tonic firing mode involves spontaneous single spike activity driven by an intrinsic pacemaker potential [40] and is thought to underlie the baseline dopamine concentrations in the striatum [39]. Phasic dopamine release is a result of burst spike firing that leads to a local increase in dopamine in specific synapses and results in a transient effect. Phasic dopamine release occurs in response to unexpected rewards or cues predicting reward and plays a key role in learning specific associations [41]. Likewise, a transient suppression of

dopamine cell firing occurs when an expected reward is omitted [42]. In contrast, tonic dopamine levels have widespread extrasynaptic effects and change on a much slower timescale than phasic levels, enabling a variety of cognitive, motor, and motivational processes [43].

Tonic and phasic dopamine levels have differential effects on dopamine receptors and afferent inputs to the striatum. For example, in the nucleus accumbens, phasic dopamine activates D_1 receptors and facilitates limbic inputs to the nucleus accumbens while tonic dopamine release has bidirectional effects with increases in tonic DA stimulation at D_2 receptors attenuating PFC afferent inputs and decreases in tonic DA stimulation at D_2 receptors facilitating PFC inputs [44]. Furthermore, tonic and phasic dopamine levels differentially activate the two classes of dopamine receptors due to differences in their affinities for dopamine. Specifically, since D_1 receptors have a lower affinity for dopamine than D_2 receptors, it was thought that large phasic dopamine bursts primarily act through dopamine D_1 receptors while background tonic dopamine levels exert their effects primarily through D_2 receptors [37]. However, more recent work has shown that D_2 receptors are in fact sensitive to both phasic and tonic dopamine levels, likely due to the two different affinity states in which they can exist [45, 46].

2.4 Role of Dopamine in Reward-Guided Behavior

While self-stimulation paradigms yielding insight into the function of the brain's reward system were pioneered in the 1950s [17], it took two decades to

discover the key role of dopamine in this network. The first observations were that dopamine antagonists attenuated the rewarding effects of brain stimulation [47] and psychomotor stimulants [48]. Shortly thereafter, it was also found that dopamine antagonists had a similar blunting of food reward-related behavior [49]. Interestingly, these early observations were made in the search for the 'neuroleptic receptor' and it was not until 1979 that the classification of dopamine receptors was established [50, 51]. Other studies around this time established the major dopaminergic pathways as well as the direct and indirect pathways involved in the initiation and inhibition of the motor cortex. Another major breakthrough in learning about dopamine's role in reward-guided behavior came with electrophysiological studies of dopamine neurons in the 1990s, yielding information about dopamine's role in learning through encoding differences between reward predictions and actual outcomes, termed "reward prediction errors".

2.4.1 Reward Prediction Errors and Associative Learning

The seminal work by Wolfram Schultz, Peter Dayan, and Read Montague recording midbrain dopamine neural activity in non-human primates showed that dopamine neurons signal errors in the predictions of future salient events. Specifically, Schultz and colleagues found that dopamine neurons increase their firing rate after receipt of an unexpected reward or cue predicting a reward, signaling a positive reward prediction error (RPE) since they receive more reward than expected. On the other hand, dopamine neurons decrease their firing rate when an expected reward is omitted, resulting in a negative RPE [2] (see **Figure**

3). Later work found that the size of the increase in dopamine neuron firing rate to an unexpected reward is proportional to the difference in magnitude between the expected and received reward [3]. RPEs were also observed when directly measuring dopamine release in the ventral striatum with fast scan cyclic voltammetry [52].

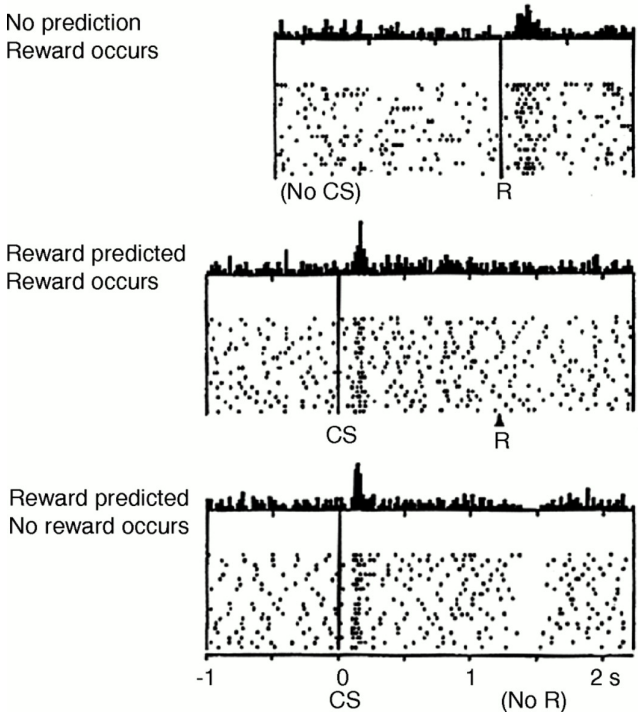


***Figure 3**: Reward prediction error signal in midbrain dopamine neurons. Midbrain dopamine neurons encode changes in predictions of salient events such a receipt of an unexpected reward (R, top), a conditioned stimulus (CS) that predicts future reward receipt (middle), and the omission of an expected reward (No R, bottom) (from [2]).*

The increase in dopamine neuron firing rate or dopamine release that is observed with RPEs is termed “phasic” or transient dopamine release. Much work has been done to elucidate the mechanism underlying phasic dopamine release [39] and RPE formation. Specifically, RPEs require input from cortical structures like the OFC [53] and habenula [54] and are altered by GABAergic neuron activation in the VTA [55]. In both electrophysiological and voltammetry

studies, it was shown that the amount of dopamine neural firing or dopamine release in response to a reward reduces as the animal learns an association between a cue (conditioned stimulus) and reward receipt [2, 52]. Through this learning process the dopamine response shifts to the cue, which becomes the salient event that signals future receipt of a reward. More recent work with optogenetics has confirmed the link between RPEs and associative learning such that positive RPEs drives associative learning [56] and negative RPEs drive extinction [57].

2.4.2 Tonic Dopamine and Average Reward Rate

In addition to transient reward prediction errors, tonic dopamine also plays a key role in reward-guided behavior. Tonic dopamine release is thought to account for the background levels of extracellular dopamine that affects the baseline level of dopamine receptor activation and thus the responsivity of the system [58]. Computational work has posited that tonic dopamine levels may reflect the long-run average reward rate of the environment, which should invigorate an organism to act more quickly to attain rewards [59]. This model was shown to successfully reproduce rodent behavior in free-operant tasks, where the rate at which an animal presses a lever to receive food is proportional to the rate of food delivery. Furthermore, another computational model demonstrated that tonic dopamine in the striatum plays a role in modifying the decision between exploring potential new rewards and exploiting well known sources of reward (explore-exploit trade-off) [60]. However, there is still a need for experimental evidence to support the predictions of these models.

2.4.3 Role of D_1 and D_2 Dopamine Receptors

It has long been known that both dopamine D_1 and D_2 type receptors play an important role in reward-guided behavior. Similar to the well described direct and indirect pathways of motor control, where dopamine binding at D_1 receptors releases thalamic inhibition and facilitates movement while binding at D_2 receptors strengthens thalamic inhibition and inhibits movement [61], dopamine receptors have been shown to differentially affect learning from positive and negative feedback. Learning from positive feedback, termed "Go" learning, is thought to rely more on D_1 receptors while learning from negative feedback, termed "NoGo" learning, relies more on D_2 receptors. This model has been supported by optogenetic studies in animals [62] and genetic and PET studies in human [63, 64]. However, this model is likely an oversimplification since it has also been shown that learning actually requires synergy between both D_1 and D_2 receptors since application of either D_1 or D_2 receptor antagonists impair learning [65-67].

Other than their potentially divergent roles in approach and avoidance learning, dopamine D_1 and D_2 receptors are also proposed to have different roles in learning from phasic compared to tonic dopamine signals. This theory is supported by the fact that D_1 and D_2 receptors have different affinities for dopamine which could allow D_1 receptors to respond more readily to large phasic increases in dopamine and D_2 receptors to be more sensitive to smaller tonic changes in dopamine levels [46]. In addition, during associative learning, transient increases in dopamine acting at D_1 receptors in the ventral striatum is

necessary for response strategy learning while suppression of tonic dopamine stimulation at D_2 receptors in the ventral striatum is required for switching response strategies as the environment changes [68, 69].

2.4.4 Dopamine and Food-Related Behavior

Much of what is known about dopamine and the reward network is also applicable to food-related behavior since food is a primary reward and is a commonly used reinforcer in animal experiments. Food reward and associated stimuli have been shown to increase dopamine levels in the ventral striatum, similar to dopamine elevating drugs of abuse such as cocaine [70, 71]. In rats, the reinforcing effects of sucrose administration is proportional to the amount of resulting dopamine release in the ventral striatum [72]. Furthermore, connections between the hypothalamus, a key region for homeostatic control of appetite, and the VTA encode learning of reward-seeking actions and have been linked to compulsive food-seeking behavior [73]. Repetitive or compulsive food-seeking behavior can also be induced by a genetic knock-out of the dopamine transporter gene, which leads to an accumulation of dopamine in the synapse [74]. Finally, dopamine is also involved in normal food-seeking behavior. In fact, mice genetically lacking tyrosine hydroxylase, a necessary enzyme for the synthesis of dopamine, fail to eat or seek food normally, despite the motor capacity to do so. Normal foraging behavior can be restored with administration of endogenous dopamine [75].

3

Methods for Measuring Dopamine Synthesis and Receptor Availability in Humans

Contents

3.1 Introduction
3.2 Positron Emission Tomography (PET)
3.3 PET Tracers of the Dopamine System
3.4 PET Data Acquisition
3.5 PET Data Analysis

3.1 Introduction

In this chapter, the current methods used for measuring dopamine synthesis and receptor availability in humans are introduced. Positron emission tomography (PET) imaging is introduced along with an overview of tracers used to measure the dopamine system. PET data acquisition and analysis methods are described in the last two sections. A more detailed review of the relevant literature is included at the beginning of each of the subsequent chapters.

3.2 Positron Emission Tomography

PET is a type of nuclear medicine imaging technique that is used to observe metabolic processes in vivo. PET imaging involves administering a radioactively labeled tracer, which decays over time and emits positrons. When an emitted positron collides with an electron an annihilation occurs, resulting in the emission of two 511 keV photons 180 degrees apart. The simultaneous detection of two photons 180 degrees apart is called a coincidence event, or prompt (**Figure 4**). Prompts are picked up by the PET scanner and reconstructed into an image.

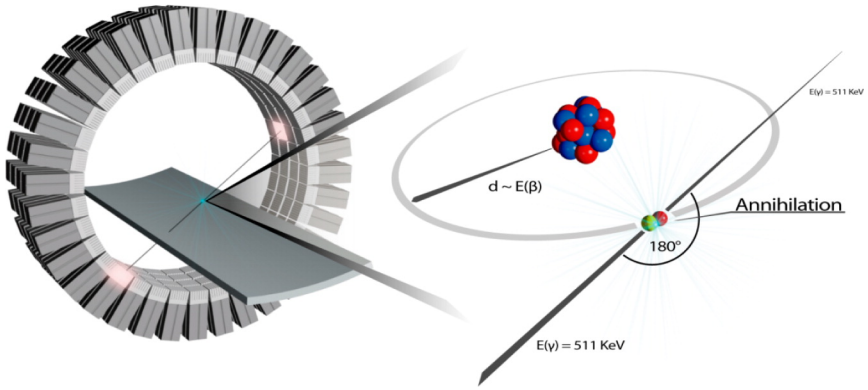


Figure 4*: Depiction of the decay of a radiopharmaceutical and subsequent annihilation event. Figure adapted from [76].*

Radioactive isotypes used in PET imaging are called radionuclides. Commonly used radionuclides include ^{15}O (2.04 min half-life), ^{11}C (20.39 minute half-life), ^{13}N (10.0 minute half-life), ^{18}F (109.8 minute half-life), ^{76}Br (16.0 hour half-life), and ^{124}I (4.17 day half-life) [76]. The decision of which radionuclide to use is primarily based on the chemistry of the pharmaceutical compound of interest to which the radionuclide will be attached, creating a radiopharmaceutical.

PET imaging has many advantages compared to other imaging modalities. First of all, it has very high sensitivity, allowing for the administration of very low doses of radiopharmaceuticals that do not have a biological effect [77]. Second, because there are a wide variety of radionuclides available, many different types of biological targets can be imaged. There are disadvantages to PET imaging as well, however. These include limited spatial resolution compared to MRI imaging (typically around 7mm or 3mm depending on the type of PET scanner used), exposure to radioactivity, and higher cost associated with the production of the radiopharmaceutical.

3.3 PET Tracers of the Dopamine System

PET imaging can be used to measure the function of the dopamine system at various levels: (1) presynaptic synthesis, (2) vesicular monoamine uptake, (3) oxidative deamination of dopamine by monoamine oxidase (MAO), (4) presynaptic dopamine transporter binding, and (5) dopamine receptor binding [76-78] (see **Figure 5**). Presynaptic function is assessed with the tracers [^{18}F]-FDOPA or [^{18}F]-FMT, which both assess the function of the rate-limiting enzyme in the conversion of [^{18}F]-FDOPA to [^{18}F]-dopamine, aromatic amino acid decarboxylase (AADC). The vesicular monoamine transporter type 2 (VMAT2) facilitates with the movement of dopamine from the cytosol into synaptic vesicles, ready to be released. Although VMAT2 is expressed by all monoaminergic neurons, in the striatum over 95% are associated with dopaminergic terminals. PET tracers for quantifying VMAT2 include [^{11}C]-dihydrotetrabenazine (DTBZ)

and [^{18}F]-FP-DTBZ [77]. The dopamine transporter (DAT) is the primary means by which dopamine is cleared from the synaptic cleft in the striatum. There are a number of PET tracers that assess the availability of DAT including [^{11}C]-CFT, [^{18}F]-CFT, [^{18}F]-FP-CIT, and [^{11}C]-PE2I.

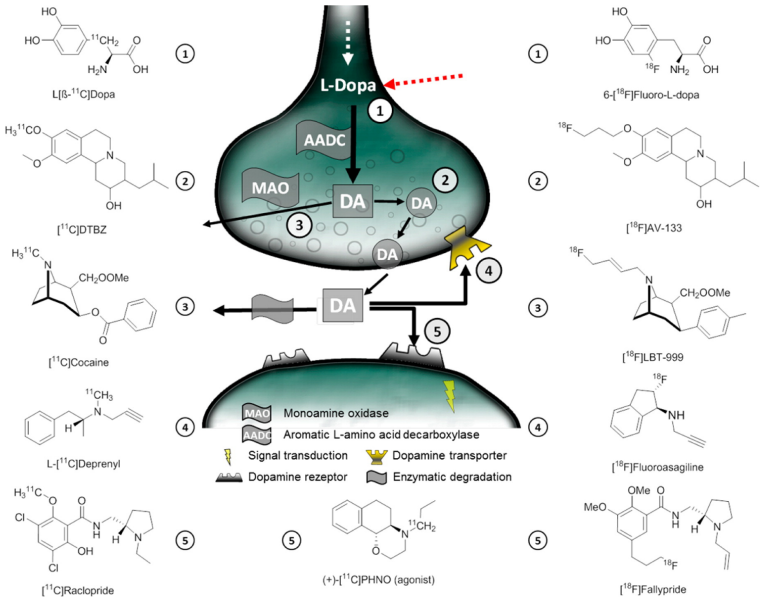


Figure 5*: Schematic of dopamine synapse and commonly used PET radioligands. Figure adapted from [76].*

Lastly, a number of tracers (or ligands) exist for measuring both D_1-like and D_2-like dopamine receptors. These tracers are generally receptor antagonists with varying degrees of displaceability. Since they are administered at such a low dose, they do not have a physiological effect. For D_1-like receptors, commonly used ligands include [^{11}C]-NNC112 and [^{11}C]-SCH 23390. For D_2-like receptors, three commonly used tracers include [^{11}C]-Raclopride, [^{11}C]-FLB 457, and [^{18}F]-Fallypride. However, all of the dopamine receptor tracers have affinity for multiple receptor types (e.g. D_1 receptor ligands often have high affinity for serotonin receptors as well and D_2 receptor ligands often

cannot differentiate between D_2 and D_3 receptors) and no tracers exist to differentially evaluate D_3, D_4, and D_5 dopamine receptors [78, 79].

In the studies included in this thesis, the three PET tracers used to quantify the dopamine system in vivo in humans include [^{18}F]-FDOPA, to assess dopamine presynaptic synthesis capacity, [^{11}C]-NNC112 to measure D_1 receptor availability, and [^{18}F]-Fallypride to measure D_2 receptor availability. [^{11}C]-NNC112 and [^{18}F]-Fallypride were chosen as the dopamine receptor ligands because of their relatively better signal in the prefrontal cortex compared to other options [79].

3.4 PET Data Acquisition

The PET scans are collected on a GE Advance 3D scanner ([^{18}F]-FDOPA) and Siemens high-resolution research tomograph (HRRT) scanner ([^{18}F]-Fallypride and [^{11}C]-NNC112). Following an eight-minute transmission scan, dynamically binned emission scans are collected for one and a half hours ([^{18}F]-FDOPA and [^{11}C]-NNC112) and four hours ([^{18}F]-Fallypride) after tracer injection. The target tracer doses are 16mCi for [^{18}F]-FDOPA, 5mCi for [^{18}F]-Fallypride, and 20mCi for [^{11}C]-NNC112. Caffeine and nicotine are restricted for four hours and food (for [^{18}F]-FDOPA only, to reduce competition for transport of the tracer into the brain) for six hours preceding the scan. Subjects are pretreated with 200mg carbidopa one hour prior to injection for the [^{18}F]-FDOPA scan to reduce peripheral degradation of the tracer. All scans are collected while subjects rest with their eyes open. To improve tolerability and wakefuleness during the [^{18}F]-

Fallypride scan, which involves a 4-hour acquisition, participants were permitted to listen to music. Subjects also complete a T1-weighted magnetic resonance imaging (MRI) scan used for registration and brain segmentation.

3.5 PET Data Analysis

All PET images undergo attenuation correction, reconstruction, and registration to align all timepoints. We then typically perform both native-space region of interest (ROI) analyses within the basal ganglia and exploratory voxelwise standard-space analyses. For both methods, we use non-invasive reference input compartmental models for PET parameter modeling, implemented with the PMOD software (http://www.pmod.com/web/). The [^{18}F]-FDOPA uptake rate (K_i) is calculated with the graphical linearization Gjedde-Patlak method [80, 81], while [^{11}C]-NNC112 and [^{18}F]-Fallypride binding potential (BP_{ND}) is calculated with the simplified reference tissue model (SRTM) method [82] (see Appendix B for justification of SRTM model validity for these tracers). BP_{ND} is a measure of receptor availability and is equal to the ratio of the rate constants k_3/k_4 in a two-tissue compartment model (**Figure 6**). The rate constant k_3 is the rate of association of the PET ligand with the specific binding sites (i.e. the dopamine receptors). This parameter is related to the concentration of available binding sites. The k_4 rate constant, or dissociation rate of the receptor-ligand complex, is thought to be invariant (http://doc.pmod.com/PDF/PKIN.pdf).

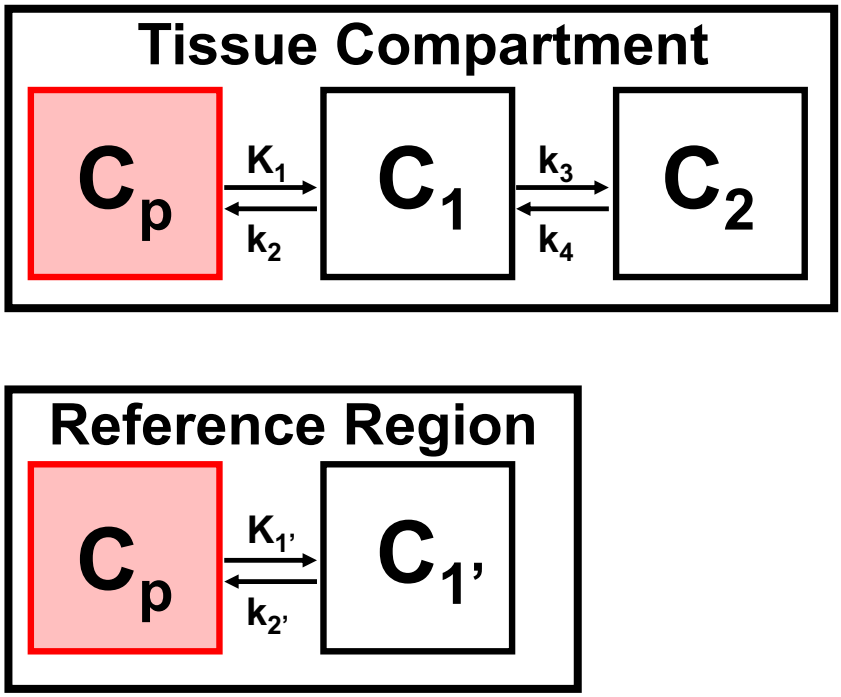


***Figure 6**. Schematic of a two-tissue reference region model*

The cerebellum is used as a reference region, delineated on individual native space MRI scans, hand-edited to remove any non-brain voxels, and trimmed to exclude the vermis and lateral and superior parasinus regions using in-house scripts. Specifically, after the MRI has been AC-PC aligned, 15mm is trimmed from the lateral boundaries of the cerebellum, 13mm in each direction from the midline, and anterior and lateral boundaries are set at y greater than 39mm and z less than 35mm. The boundary values were determined from empirical testing and visual inspection.

For ROI analyses, native-space MRI scans are segmented using Freesurfer (https://surfer.nmr.mgh.harvard.edu/) and manual adjustments to generate standard ROIs of the basal ganglia, where dopamine projections and

receptors are most abundant: dorsal putamen, dorsal caudate nucleus, ventral striatum, and dopaminergic midbrain (see **Figure 7**).

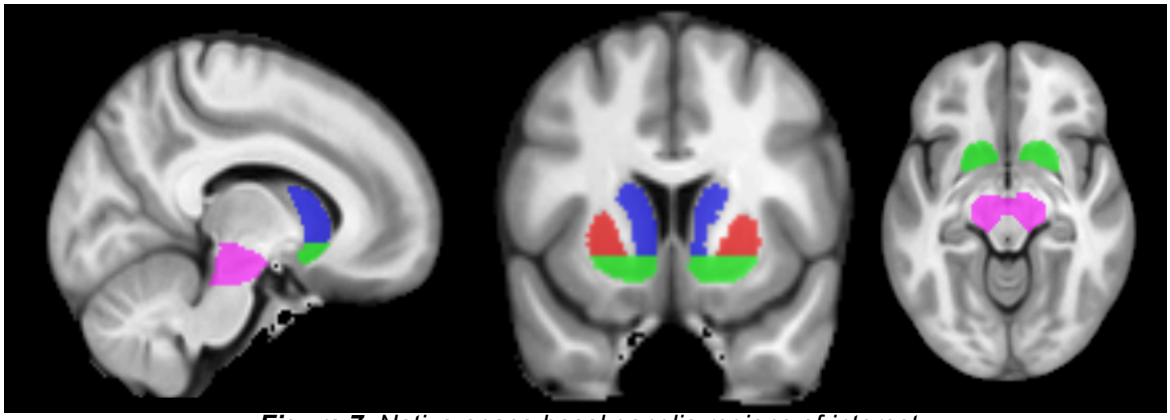


***Figure 7**: Native-space basal ganglia regions of interest.*
Regions include the dorsal putamen (red), dorsal caudate nucleus (blue), ventral striatum (green) and dopaminergic midbrain (magenta).

PET images are corrected for inter-scan motion and realigned using FLIRT (http://fsl.fmirb.ox.ac.uk/fsl/). MRI images are registered to native space mean PET images and time-activity curves are extracted for each of the ROIs. For voxelwise analyses, each individual's coregistered anatomical MRI image is warped to a common space (MNI) template using ANTS software (http://stnava.github.io/ANTs/) and the resulting transformation matrix is applied to the PET images. Common space PET images are smoothed using a three-dimensional Gaussian kernel of 10mm^3 before undergoing modeling in PMOD.

Statistical correction for multiple comparisons is done using a false discovery rate (FDR) level of 0.05 (or 5%) as described by Benjamini and Hochberg [83]. Specifically, for ROI analyses, FDR correction was implemented by hand by ranking the p-values of all correlations tested (n) within each specific tracer from lowest to highest (ranking = i, with the least significant p-value having

a value of 1). The critical p-value for each correlation is calculated as (1/i)*0.05. The highest p-value that is smaller than the critical value is identified and all correlations with lower p-values are considered significant. For voxelwise analyses, FDR correction is implemented using the same procedure with built-in functions of the neuroimaging analysis software used (i.e. SPM [www.fil.ion.ucl.ac.uk/spm/software/] or FSL [https://www.fmrib.ox.ac.uk/fsl]). We use FDR correction rather than familywise error rate (FWER) correction because of its increased sensitivity to any signal present in the data [84]. In comparison to FWER methods which control for the chance of any false positives and have relative poor power and high risk of false negatives, FDR correction controls the proportion of false positive among the reported results (those that differ from the null hypothesis). The result is increased power to detect true signal while still maintaining control of false positives [85].

4

Dopamine Synthesis and Receptor Profile Are Associated with Body Mass Index in Humans

Contents

Abstract
4.1 Introduction
4.2 Experimental Procedures
4.2.1 Participants
4.2.2 BMI Quantification
4.2.3 Imaging data acquisition
4.2.4 Imaging data analysis
4.3 Results
4.3.1 Demographics and Effects of Age and Gender
4.3.2 Dopaminergic PET Correlations with Current BMI
4.3.3 Dopaminergic PET Associations with Prior BMI Change
4.4 Discussion

Chapter 4 Abstract

Obesity is a worldwide epidemic that involves dysfunction of the dopaminergic reward system. However, we lack a detailed, systems-level understanding of interactions between aspects of the dopamine system and body mass regulation. To address this question, we used PET imaging to directly measure dopamine synthesis capacity (with [^{18}F]-FDOPA) and dopamine

receptor availability (D_1 and $D_{2/3}$ receptors with [^{11}C]-NNC112 and [^{18}F]-Fallypride, respectively) in 117 individuals with body mass index (BMI) values ranging from normal to moderately obese. We found that elevated BMI was associated with heightened dopamine synthesis capacity in the hypothalamus, a key region for homeostatic appetite control, and lower $D_{2/3}$ receptor availability in the midbrain, where D_2 receptors play an important role in the autoregulation of striatal dopamine release. In addition, we found that weight gain in the 1-2 years before scanning was associated with greater dopamine synthesis capacity in the ventral striatum and midbrain. These data suggest that aberrant body mass regulation is related to dopamine hypersynthesis in reward- and homeostatic-related regions coupled with deficient autoregulation.

4.1 Introduction

The obesity epidemic affects about 13% of the adult population worldwide and up to 33% in developed countries such as the United States, a burden that has more than doubled in the past 30 years when sedentary lifestyles and Western diets have increasingly predominated [86, 87]. It is clear from extensive prior scientific work that activity and consumption behaviors underlying body mass adaptations rely on homeostatic and motivational neurocircuitry. The regulation of eating behaviors, for instance, involves a number of factors including peripheral signals that are transported to the brain (e.g. ghrelin, leptin, insulin), energy homeostatic mechanisms occurring in the hypothalamus, and function of the reward system [88]. Dopaminergic mechanisms are thought to be

involved in all of these factors including interactions with peripheral signals [89-91], regulation of appetitive neurotransmission in the hypothalamus [92, 93], and, most prominently, a central role in the mesolimbic reward system (i.e., the ventral tegmental area of the midbrain and its projections, including the ventral striatum) [2, 3, 94]. Accordingly, substantial evidence has supported a direct link between dopamine and weight control, with the mesolimbic system being most frequently implicated in human studies [95-97].

Abnormalities of the mesolimbic dopamine system have been implicated in both the development of obesity [98, 99] and obesity progression [100-105], although the results of studies to date have been mixed. Some find that obese individuals have decreased striatal fMRI blood-oxygen-level dependent (BOLD) activity during food consumption [99, 106, 107] but increased striatal BOLD response to food versus neutral cues [108] in a manner that forecasts future weight gain [101]. However, other studies have failed to replicate these striatal findings during food consumption [109], report reduced activation in areas other than the striatum (e.g. left dorsolateral prefrontal cortex) [110, 111], or report increased activation in extra-striatal regions related to somatosensory, gustatory, and reward valuation processes [109]. The findings of increased activation to food anticipation have also been inconsistent, with a number of extra-striatal regions implicated including those important for reward processing, habit learning, taste, and emotion [108, 112-118], although the opposite pattern has also been reported in reward-related regions [107, 117-119], and there is still controversy over whether physiological states (i.e. hunger vs. satiety) affect

these patterns. Additionally, increased BMI has also been linked to structural alterations in reward-related brain regions such as the vmPFC [120].

Due to the implication of the reward system in obesity, a number of studies have also investigated changes in dopamine $D_{2/3}$ receptors. A seminal study by Wang et al. showed that morbidly obese individuals show decreased dopamine $D_{2/3}$ receptor levels throughout the striatum [98]. This finding has been replicated in a subsequent human PET study [121] as well as in rodents where it was also correlated with future weight gain and food seeking-behavior [100]. However, many other studies have failed to replicate this finding [122-126], have shown the opposite pattern [106, 127-129], or have found a more complicated pattern such as a negative correlation between BMI and $D_{2/3}$ receptor binding potential in the ventromedial striatum but a positive correlation in the dorsolateral striatum [130].

As highlighted in the previous two paragraphs, the evidence supporting the role of dopamine and the reward system in the obesity epidemic has been fairly inconsistent, which has led to competing theories of the primary dopaminergic abnormalities in obesity. For instance, both dopaminergic hypofunction, 'reward-deficiency', [131-133] and dopaminergic hyperfunction, 'reward surfeit' [134, 135] models have been proposed, as well as a model of imbalance between motivational and inhibitory circuits [97]. Furthermore, only select aspects of the multifaceted dopamine system have been explored thusfar, and the lack of an integrated understanding of particular dopaminergic system characteristics in relation to states of body mass maintenance remains a barrier

to better insight into the neural mechanisms most relevant to the obesity epidemic and to development of targeted pharmacological treatments.

To address this knowledge gap, we studied a cohort of healthy humans in the normal to obese BMI range and not only assessed $D_{2/3}$ receptor availability, but also dopamine synthetic capacity and D_1 receptor availability in the basal ganglia and hypothalamus, key regions in the reward and homeostatic networks. We tested the hypothesis that increased body mass is associated with a model of diminished dopamine receptors, disinhibited appetitive drive and diminished consumptive reward in obesity. We predicted that increased BMI or previous weight gain would be related to heightened dopamine synthesis capacity, consistent with previous studies showing increased reward function during the anticipation of food consumption in obese individuals and those susceptible to future weight gain [101]. Furthermore, we expected to replicate previous human and rodent studies showing a link between obesity and diminished dopamine D_2 receptors [98, 100]. Taken together, we predicted that aberrant weight regulation would be linked to increased dopamine synthesis coupled with decreased sensitivity to and regulation of dopamine release, reflected as fewer dopamine receptors.

4.2 Experimental Procedures

4.2.1 Participants

One hundred and seventeen healthy adult volunteers with body mass indices ranging from normal to moderately obese were recruited from the local

community and screened by physician-administered physical and neurological examination, standardized clinical interview (SCID) [136], laboratory tests, and structural MRI read by a radiologist to rule out psychiatric, neurological, and major medical illness. Of the 117 participants, 113 completed the [^{18}F]-FDOPA PET scan, 76 completed the [^{11}C]-NNC112 scan, and 76 completed the [^{18}F]-Fallypride scan. All participants provided informed consent and were compensated for their participation. Study procedures were approved by the NIH Combined Neurosciences Institutional Review Board and Radiation Safety Committee.

4.2.2 BMI Quantification

Body mass index was calculated using height and weight measurements taken by nursing staff around the time of the PET scan ([^{18}F]-FDOPA: mean 0.05±0.26 years before scan; [^{11}C]-NNC112: mean 0.02±0.13 years before scan; [^{18}F]-Fallypride: mean 0.01±0.17 years before scan). In addition, for a subset of subjects, BMI was measured 1-2 years prior to the PET scan ([^{18}F]-FDOPA: 59 subjects, mean prior BMI measurement date 1.43±0.24 years before PET scan; [^{11}C]-NNC112: 42 subjects, mean prior BMI measurement date 1.51±0.22 years before PET scan; [^{18}F]-Fallypride: 42 subjects, mean prior BMI measurement date 1.49±0.25 years before PET scan), and subjects were placed into weight gain or loss groups based on their change in BMI between the prior value and value at the time of the PET scan. Additionally, we determined the rate of BMI change leading up to the scan (calculated as the difference in BMI values before and at the time of the scan divided by the time between measurements) and ran

linear regression analyses with the PET ROI and voxelwise measures that yielded very similar results to those when comparing weight gain and loss groups.

4.2.3 Imaging Data Acquisition

On separate days, subjects completed three positron emission tomography (PET) scans to assess dopamine presynaptic synthesis capacity (with [^{18}F]-FDOPA), and D_1 and $D_{2/3}$ receptor binding potential (with [^{11}C]-NNC112 and [^{18}F]-Fallypride, respectively) while resting with their eyes open. The PET scans were collected as described in Section 3.4. The target (and actual) tracer doses were 16mCi for [^{18}F]-FDOPA (actual dose received range: 12.9-16.9mCi), 5mCi for [^{18}F]-Fallypride (actual dose received range: 4.54-5.31mCi), and 20mCi for [^{11}C]-NNC112 (actual dose received range: 15.16-20.27mCi).

4.2.4 Imaging Data Analysis

Imaging data were analyzed as described in Section 3.5 with the modification that the voxelwise standard-space analyses were restricted to localized results within our predefined networks of interest: the basal ganglia (reward network) and the hypothalamus (homeostatic network). Region of interest analyses were performed using a Pearson correlation (for BMI correlations) and Univariate General Linear Model (for BMI change group comparisons) implemented in SPSS (IBM SPSS Statistics for Macintosh, Version 22.0). Significance was assessed using a threshold of $p<0.05$, FDR-corrected for multiple comparisons across the four ROIs, after controlling for age and gender

effects (see Section 3.5 for details on FDR-correction methods used and justification for why the FDR method was chosen). For voxelwise analyses, PET images were spatially normalized to Montreal Neurological Institutes space and smoothed at 10mm^3 before undergoing modeling in PMOD. The basal ganglia mask was created using a similar method to the native-space ROI creation, except performing the Freesurfer segmentation on an average T1-weighted MRI created from 152 healthy volunteers and including regions from the striatum and dopaminergic midbrain. The hypothalamus mask was created using the WFU PickAtlas software (Wake Forest University, Winston-Salem, NC, USA) and dilated volumetrically by 2 voxels. SPM5 (Wellcome Trust Centre for Neuroimaging, University College London) was used to implement voxel-wise general linear model analyses to assess for correlations with BMI and differences between BMI change groups. A statistical threshold of $p<0.05$, FDR-corrected (with a basal ganglia and hypothalamus small volume correction applied, in two separate analyses with either the basal ganglia or hypothalamus mask applied individually) after controlling for age and gender, was used to assess significance.

4.3 Results

4.3.1 Demographics and Effects of Age and Gender

One hundred and seventeen healthy volunteers aged 18.7 to 52.1 years (mean 34.3, 60 females) with body mass indices ranging from 18.3 to 36.1 (mean

25.1) participated in this study. Demographic information for the subset of participants who completed each PET scan is contained in **Table 1**.

Table 1: BMI Analysis Participant Demographics

Analysis	Number of Subjects	Gender (F/M)	Age range (mean ± std dev)	BMI range (mean ± std dev)
All	117	60/57	18.7-52.1 (34.3±8.9)	18.3-36.1 (25.1±3.7)
Current BMI				
[^{18}F]-DOPA: ROI	110	56/54	18.7-49.9 (32.8±8.4)	18.5-34.8 (25.1±3.7)
[^{18}F]-DOPA: Voxelwise	113	58/55	18.7-49.9 (32.9±8.4)	18.5-34.8 (25.1±3.7)
[^{18}F]-Fallypride: ROI	76	39/37	18.7-54.1 (35.4±9.2)	19.7-36.1 (25.2±3.7)
[^{18}F]-Fallypride: Voxelwise	70	35/35	18.7-54.1 (35.3±9.3)	19.8-36.1 (25.3±3.4)
[^{11}C]-NNC112: ROI	76	41/35	18.7-54.1 (34.8±9.0)	18.3-35.9 (25.0±3.8)
[^{11}C]-NNC112: Voxelwise	75	40/35	18.7-54.1 (34.8±9.1)	18.3-35.9 (25.0±3.8)
Prior BMI change				
[^{18}F]-DOPA: ROI	Total: 57 Gained weight: 32 Lost weight: 25	30/27	20.2-48.9 (32.4±8.2)	
[^{18}F]-DOPA: Voxelwise	Total: 59 Gained weight: 33 Lost weight: 26	32/27	20.2-48.9 (32.5±8.3)	
[^{18}F]-Fallypride: ROI	Total: 41 Gained weight: 22 Lost weight: 19	25/16	20.8-48.3 (34.5±8.3)	
[^{18}F]-Fallypride: Voxelwise	Total: 42 Gained weight: 22 Lost weight: 20	25/17	20.8-48.3 (34.6±8.2)	
[^{11}C]-NNC112: ROI	Total: 42 Gained weight: 21 Lost weight: 21	25/17	20.9-48.8 (34.1±7.6)	
[^{11}C]-NNC112: Voxelwise	Total: 42 Gained weight: 21 Lost weight: 21	25/17	20.9-48.8 (34.1±7.6)	

The group consisted of 102 participants of Caucasian descent, nine African Americans, four participants of Asian descent, and two who identified as mixed race. Age was not correlated with current BMI, but there was an age difference between the prior BMI change groups in the [^{18}F]-FDOPA analysis only: $F=4.455$, $p=0.039$; weight loss group mean age 35.0±8.8 years, weight gain group mean age 30.6±7.4 years. There were no age-by-BMI interaction effects for any of the PET measures. There was an effect of gender on current BMI for the [^{11}C]-NNC112 analysis only ($p=0.029$). There were no gender effects on current BMI for the [^{18}F]-FDOPA or [^{18}F]-Fallypride scans nor gender differences between the BMI change groups for any of the PET scans. We controlled for age and gender

effects in the region of interest and voxelwise PET results reported below, which are listed in **Table 2** and **Table 3**.

Table 2: BMI Analysis Region of Interest Results*

Contrast	Region	Statistical Measure	Uncorrected p-value*
[^{18}F]-Fallypride Negative Correlation with Current BMI	Midbrain	Pearson r=-0.341	0.008
[^{18}F]-DOPA K_i: Weight gain subjects > Weight loss subjects	Ventral striatum	F=7.268	0.009

*Results meet correction for multiple comparisons in four regions of interest at FDR p<0.05.

Table 3: BMI Analysis Voxelwise Results*

Contrast	Small Volume Correction Region	Region	Peak voxel coordinate (MNI)	Peak voxel FDR corrected p-value	Peak T value	Cluster size
[^{18}F]-DOPA K_i Positive Correlation with Current BMI	Hypothalamus	Right hypothalamus	(9,0,-16)	0.00833	4.30	152
[^{18}F]-DOPA K_i Positive Correlation with Current BMI	Hypothalamus	Left hypothalamus	(-9,0,-15)	0.0444	2.80	4
[^{18}F]-DOPA K_i: Weight gain subjects > Weight loss subjects	Basal ganglia	Right ventral striatum	(21,6,-14)	0.00347	4.84	1074
[^{18}F]-DOPA K_i: Weight gain subjects > Weight loss subjects	Basal ganglia	Midbrain	(-2,-30,-24)	0.00430	4.23	424
[^{18}F]-DOPA K_i: Weight gain subjects > Weight loss subjects	Basal ganglia	Left ventral striatum	(-21,14,-12)	0.0125	3.27	815

*Search volume restricted to indicated small volume correction region (basal ganglia or hypothalamus). Voxel-wise FDR corrected p<0.05.

4.3.2 Dopaminergic PET Correlations with Current BMI

In the native-space basal ganglia ROI analysis, we found that BMI correlated negatively with $D_{2/3}$ receptor BP_{ND} in the midbrain (r=0.341, p=0.008; **Figure 8**) as well as a trend in the ventral striatum in the same direction (r=-0.202, p=0.096). In the voxelwise a prior networks of interest analysis, we found that presynaptic dopamine synthesis capacity in the bilateral hypothalamus correlated positively with current BMI (right (9, 0, -10): $p_{uncorrected}$=1.9e-5, p_{FDR}=0.00833; left (-9, 0, -15): $p_{uncorrected}$=0.0031, p_{FDR}=0.0444; see **Figure 9**).

Current BMI did not correlate with D_1 receptor BP_{ND} in any of the ROIs or voxelwise a priori networks of interest.

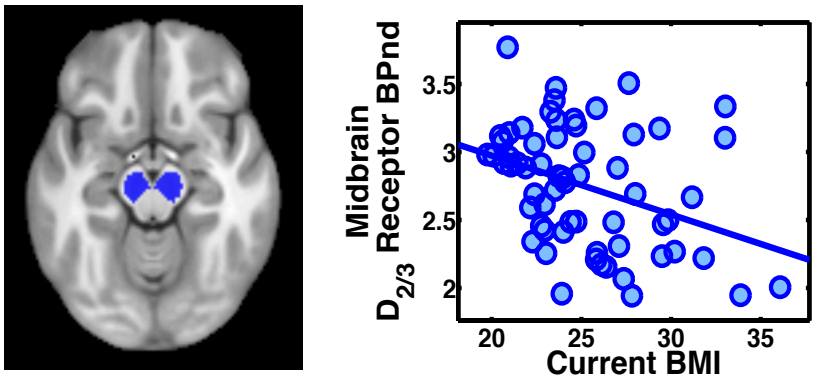


***Figure 8**: Negative correlation between current BMI and D_2 receptor BP_{ND} in the dopaminergic midbrain (r=-0.341, p=0.008).*

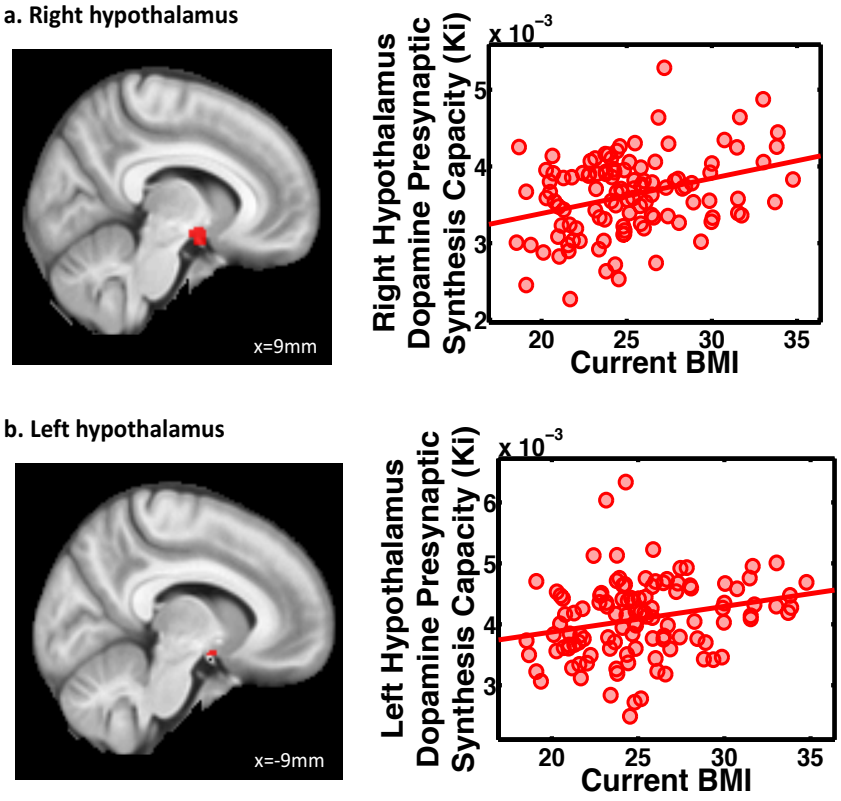
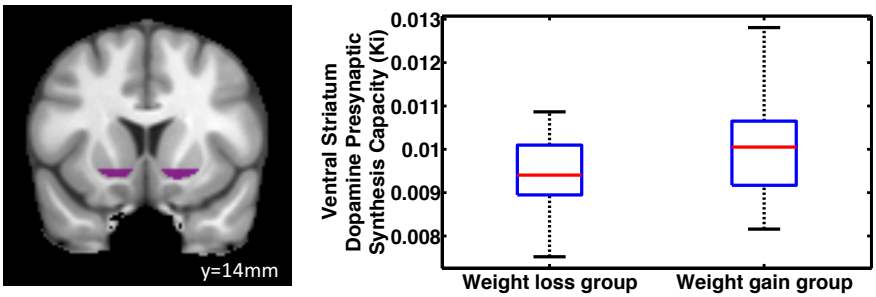


***Figure 9**: Positive correlation between current BMI and dopamine presynaptic synthesis capacity in the bilateral hypothalamus.*
(a) Right hypothalamus, MNI peak-voxel coordinates (9, 0, -10), $p_{uncorrected}$=1.9e-5, p_{FDR}=0.00833,
(b) Left hypothalamus, MNI peak-voxel coordinates (-9, 0, -15), $p_{uncorrected}$=0.0031, p_{FDR}=0.0444.
Voxelwise images are displayed at a threshold of p<0.005, uncorrected.

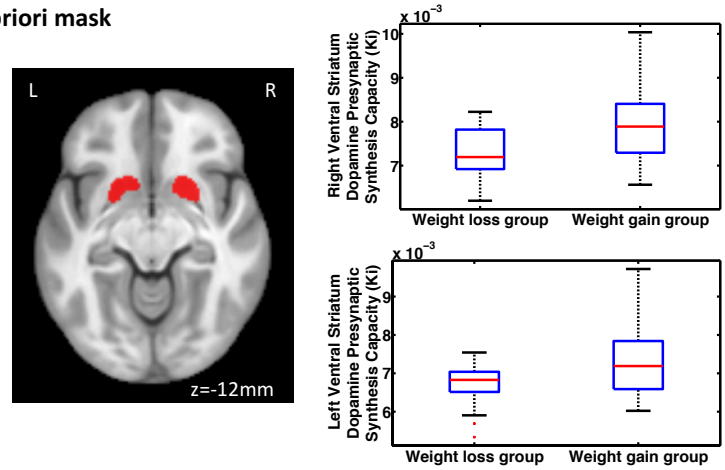
4.3.3 Dopaminergic PET Associations with Prior BMI Change

We found that individuals who gained weight had increased dopamine synthesis capacity in the ventral striatum compared to those who lost weight prior to the PET scan. This was significant in both the native-space ROI analysis (bilateral ventral striatum F=7.268, p=0.009) and MNI space voxelwise analysis using the basal ganglia a prior mask (right ventral striatum: $p_{uncorrected}$=5.5e-6, p_{FDR}=0.00347; left ventral striatum: $p_{uncorrected}$=9.2e-4, p_{FDR}=0.0125; see **Figure 10**). In addition, in the voxelwise analysis, we also found that individuals who gained weight had increased dopamine synthesis capacity in the midbrain ($p_{uncorrected}$ = 4.4e-5, p_{FDR} = 0.0043) compared to those who lost weight prior to the PET scan. In the linear regression analysis with BMI rate of change, we found similar results (ROI analysis: ventral striatum p=0.043; voxelwise analysis: right ventral striatum $p_{uncorrected}$=1.8e-4, p_{FDR}=0.0409, left ventral striatum $p_{uncorrected}$=1.2e-3, p_{FDR}=0.0409, midbrain $p_{uncorrected}$=2.3e-3, p_{FDR}=0.0409). We did not find any associations between dopamine receptor binding potential and prior BMI change.

a. Native-space ventral striatum ROI (one example ROI shown here)



b. Ventral striatum from MNI-space voxelwise analysis with basal ganglia a priori mask



c. Midbrain from MNI-space voxelwise analysis with basal ganglia a priori mask

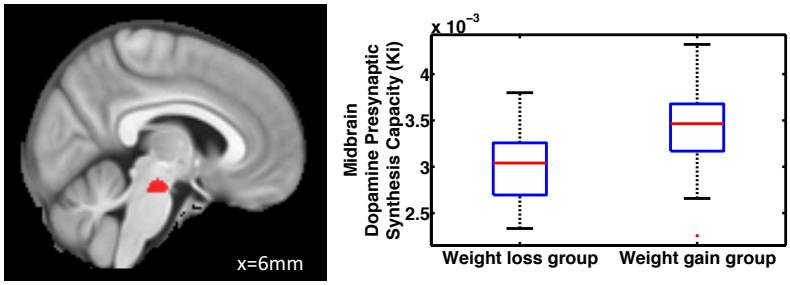


***Figure 10**: Increased dopamine synthesis capacity in individuals who gained weight compared to those who lost weight prior to the PET scan in the ventral striatum and midbrain.*
***(a)** Ventral striatum: Native-space ROI analysis (F=7.268, p=0.009),*
***(b)** Ventral striatum: MNI-space voxelwise analysis using the basal ganglia a prior mask (right (21,6,-14): $p_{uncorrected}$=5.5e-6, p_{FDR}=0.00347; left (-21,14,-12): $p_{uncorrected}$=9.2e-4, p_{FDR}=0.0125),*
***(c)** Midbrain (-2,-30,-24), $p_{uncorrected}$=4.4e-5, p_{FDR}=0.0043.*
Voxelwise images (in red) are displayed at a threshold of p<0.005, uncorrected.

4.4 Discussion

In line with our hypothesis, we found that increased BMI was related to enhanced dopamine tone along with diminished receptor availability. Specifically, we found a positive correlation between current BMI and dopamine synthesis capacity in the hypothalamus, an area that plays a key role in the homeostatic regulation of appetite. Hypothalamic dopamine acts as a satiety signal and the release of dopamine in the lateral hypothalamic area and ventromedial hypothalamus has been linked to meal size and time between meals in normal rats [137, 138] and is increased during meal ingestion in obese compared to normal size rats [139, 140]. Furthermore, electrical stimulation of the lateral hypothalamus results in enhanced “wanting” without “liking” of food rewards as well as increased meal size in rats [141]. A potential mechanism of this phenomenon is the subsequent increase in dopamine release in the nucleus accumbens that results from electrical stimulation of the lateral hypothalamus [142]. Dopamine modulates neuronal excitability depending on the type of dopamine receptor that is activated [143], so altered presynaptic dopamine in the hypothalamus could subsequently affect dopamine release in the ventral striatum. Unfortunately, we cannot differentiate between individual nuclei in the hypothalamus due to the limited spatial resolution of our PET images. Nonetheless, our finding of a positive correlation between BMI and hypothalamic dopamine synthesis capacity is consistent with rodent work supporting the idea that higher BMI may be linked to altered dopamine homeostatic satiety mechanisms in the hypothalamus.

In line with independent past work, we also found that current BMI correlated inversely with $D_{2/3}$ receptor binding potential in the brains of human volunteers across the BMI spectrum [98, 100], adding support to the link between mesolimbic dopamine systems and body mass regulation. Unlike prior reports, we observed this effect in the dopaminergic midbrain, where presynaptic autoreceptors abound. Though the current design cannot distinguish with certainty between pre- and post-synaptic receptor binding, nor between dopamine D_2 and D_3 receptors, our results are concordant with previous findings that D_2 autoreceptor deficient mice show increased food-seeking behavior [144]. Although not significant at the FDR-corrected level, we also found a trend-level negative correlation between BMI and ventral striatum $D_{2/3}$ receptor BP_{ND}, consistent with past studies in humans [98] and rodents [100]. Therefore, our findings of a negative correlation between BMI and midbrain D_2 receptor binding potential could support the reward deficiency theory of obesity, suggesting that individuals with lower reward system sensitivity may overeat to compensate for this deficiency. However, given the importance of midbrain D_2 autoreceptors in inhibiting striatal dopamine release [144], our results could also support a model in which increased body mass index results from altered mesolimbic dopamine regulation, where impaired inhibition via autoreceptors could lead to exaggerated striatal dopamine release. Taken together, our results of increased BMI being linked to decreased $D_{2/3}$ receptors and increased hypothalamic dopamine synthesis capacity lead us to conclude that higher BMI is related to altered regulation of the mesolimbic dopamine system.

In addition to dysfunction of dopamine regulatory mechanisms, we also hypothesized that increased BMI would be related to heightened synthesis in the mesolimbic dopamine system. While we did not find any significant correlations between striatal dopamine synthesis and current BMI, we did find that dopamine tone in the ventral striatum and midbrain was increased in individuals with recent prior weight gain compared to those with recent weight loss. Two potential conclusions could be surmised from this finding: (1) increased mesolimbic dopamine synthesis capacity makes people susceptible to weight gain, or (2) recent weight gain leads to increased mesolimbic dopamine tone. Unfortunately, we are unable to differentiate between these two conclusions with the retrospective, cross-sectional design of the present study. Nonetheless, our observation of increased mesolimbic dopamine synthesis in individuals with prior weight gain is consistent with the known important role that the dopamine system plays in reward-guided learning, craving, and motivation [2, 3, 145]. With respect to feeding behavior in particular, it has been shown that dopamine is released in response to eating palatable foods [145-148], which is correlated with both meal pleasantness [149] and food caloric density [150], and that dopamine modulates neural representations of food value-related signals [151]. Therefore, it is easy to understand how hyperactivity of the reward system may trigger food craving or prolong eating past satiety, thus leading to weight gain and development of obesity. In fact, a link has been demonstrated between hyper-responsivity of the reward system to milk-shake consumption and future weight gain [103, 104]. However, other studies have shown that this link depends on genetic risk [152-

154]. An alternative model of obesity (the "incentive sensitization model") suggests that repeated intake of palatable food may cause elevated reward responsivity to associated cues via classic conditioning, resulting in increased craving and food intake when the cues are encountered [155]. This model is supported by studies showing that future weight gain is predicted by hyper-responsivity of reward regions to palatable food images [101], food TV commercials [156], geometric cues that signal impending food image presentation [114], food odors that predict food receipt [104], and pictorial cues that predict food receipt [153]. While our results cannot differentiate between these two models, our findings of positive correlations between dopamine synthesis capacity in reward-, homeostasis-, and executive control-related regions support the general concept that obesity is related to hyperactivity of the dopamine system.

Taken together, these data suggest that a neural signature related to current BMI across the normal to obese range includes relatively increased presynaptic dopaminergic tone in the homeostatic hypothalamus and diminished mesolimbic regulatory D_2 receptors. Furthermore, recent change in BMI is related to increased dopamine tone in the ventral striatum and midbrain, key regions in the reward network. Given the cross-sectional nature of our study, we are limited in our ability to determine a causal link between these deficits and the development of obesity. However, by investigating three different aspects of the dopamine system in the same individuals, we are able to reconcile apparently conflicting models of dopamine's role in obesity. Specifically, our data suggest

that upregulation of body mass is related to both hyperactivity of the mesolimbic dopamine system as well as altered regulation (increased dopamine tone in the homeostatic hypothalamus and decreased $D_{2/3}$ receptors in the midbrain). Future work must include a longitudinal characterization of the dynamic relationship between dopaminergic dysfunction and increased BMI.

5

Dopamine Synthesis and Receptor Profile Association with Foraging Behavior in Humans

Contents

Abstract
5.1 Introduction
  5.1.1 Marginal Value Theorem
  5.1.2 Neural Circuit Implicated in Foraging Behavior
  5.1.3 Implication of Dopamine in Foraging Behavior
  5.1.4 Dissociation of Neural Mechanisms Encoding Reward Timing and Magnitude
5.2 Methods
  5.2.1 Study Participants
  5.2.2 Patch Foraging Behavioral Task
  5.2.3 Behavioral Measures of Interest
  5.2.4 PET Imaging Methods
  5.2.5 Principal Component Analysis of PET data
  5.2.6 Statistical Analyses
5.3 Results
  5.3.1 Behavioral Results
  5.3.2 PET Data PCA Results
  5.3.3 Correlations Between Foraging Behavior and Dopamine Function
  5.3.4 Total change in patch leaving threshold
  5.3.5 Change in threshold due to travel time and depletion rate
5.4 Discussion

Chapter 5 Abstract

Foraging is a type of food-reward guided behavior that involves searching for rewards within an environment where rewards occurs in groups such as a tree full of berries. Optimal foraging theory states that an animal should leave one group of rewards to search for another when the rate at which it is receiving rewards in the current group falls below the average for the environment. Computational work posits that striatal dopamine plays a key role in encoding the average reward rate of the environment, however, its role in foraging behavior has not yet been characterized. To address this gap in knowledge, we used PET imaging to directly measure dopamine synthesis capacity (with [^{18}F]-FDOPA) and dopamine receptor availability (D_1 and D_2 receptors with [^{11}C]-NNC112 and [^{18}F]-Fallypride, respectively) in 57 healthy adults who also completed a computer-based foraging task. We measured the threshold at which people decided to leave one group of rewards in search of another in four reward environments with different average reward rates and found that the amount that people changed their threshold was correlated with two specific patterns of dopamine synthesis and receptor availability. These results provide insight into the neural mechanisms underlying food-seeking behavior in humans.

5.1 Introduction

To build on the findings described in Chapter 4 on the role of dopamine in body mass regulation, we investigated dopamine's role in an important food-seeking behavior, foraging. Foraging is a type of reward-guided behavior that is

essential for survival and conserved across species. In contrast to comparative decision-making between two currently available options, the important choice in foraging behavior is whether to engage with the current environment or leave and search elsewhere. Prior work has been done to describe optimal foraging behavior (Section 5.1.1) and the neural circuit involved in foraging behavior (Section 5.1.2), but the role of dopamine synthesis and receptor availability is still not clear. The work described in this chapter aims to characterize the relationship between dopamine and foraging behavior in humans.

5.1.1 Marginal Value Theorem

Foraging behavior in an environment where rewards are concentrated in groups or patches can be quantified using the marginal value theorem (MVT), which weighs benefits and costs in order to quantify the optimal thresholds to leave one patch of rewards and search elsewhere [1]. Experimental evidence supports that this theorem accurately describes the behavior of wild animals [30, 157] and that of humans performing a computer-based foraging task [158]. According to the MVT, animals should leave a current patch of rewards (e.g. prey) in search of a new one when the reward rate in the current patch falls below the average reward rate for the environment [1]. In many ecological settings and in our experiment, the average reward rate for the environment depends on two factors: (1) the reward depletion rate within each patch of rewards and (2) the travel time between patches. Therefore, these two parameters should be accounted for when deciding when to leave a patch.

5.1.2 Neural Circuit Implicated in Foraging Behavior

Foraging behavior depends on the function of a widespread circuit in the brain (including the midbrain, striatum, medial prefrontal cortex, and anterior cingulate cortex), which is important for encoding value and integrating and comparing values of different options to appropriately adjust behavior [29, 30, 159]. More specifically, it has been shown in non-human primates that neurons in the dorsal anterior cingulate cortex (ACC) are especially important for foraging decisions [30]. These neurons encode the relative value of leaving one patch of rewards to search for a new one and fire each time that a decision is made to stay in a patch. The firing rate at the decision point increases the longer that the animal has been in a reward patch, until a threshold is reached and the animal decides to leave the reward patch (see **Figure 11**A). Interestingly, the firing rate

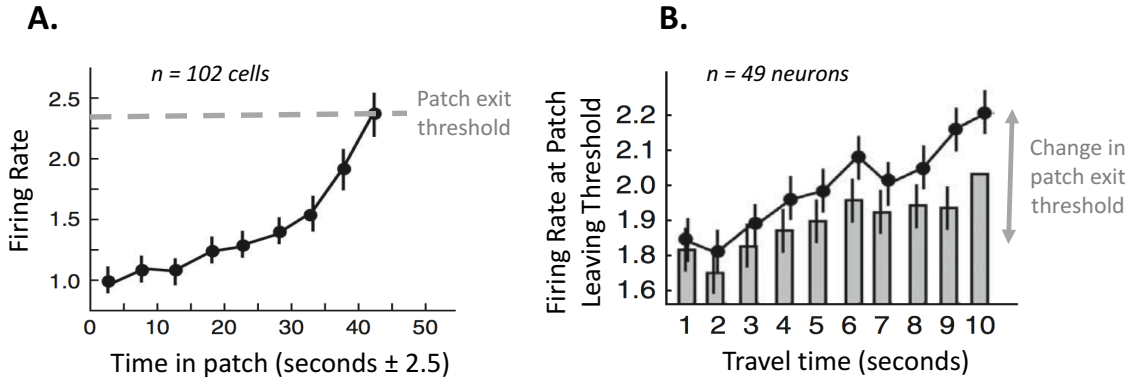


Figure 11*. ACC neural activity in non-human primates during foraging. (A) ACC neural firing rate increases with time spent in a reward patch until a threshold is reached and the animal leaves for a new patch. (B) The neural firing rate threshold for leaving a patch increases as travel time between reward patches increases. Figures adapated from Hayden, Nature Neuroscience, 2011 [30].*

threshold at which the animal decides to leave a reward patch is fixed for a given travel time delay between reward patches, where the threshold is highest for reward environments with longer travel time delays (see **Figure 11**B).

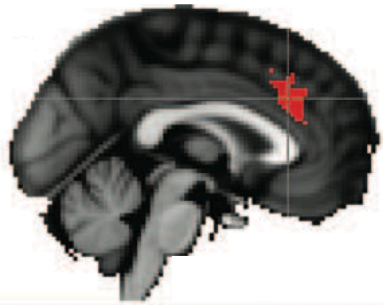


***Figure 12**. ACC BOLD fMRI activation associated with the search value of the foraging environment.*
Figure adapted from Kolling, Science, 2012 [29].

More insight into the neural mechanisms of foraging comes from a seminal human functional MRI (fMRI) decision-making study [29]. Nils Kolling and colleagues found that the ACC contains a signal related to the average value of searching the environment, or the foraging search value, a key decision variable when foraging since optimal behavior would be to leave when the value of current reward patch falls below the average (see **Figure 12**). Furthermore, the striatum plays a key role in foraging decision by both signaling prediction-error signals after a decision to search elsewhere us made and encoding search costs. In addition, coupling between neural activity in the ventral striatum and ACC is increased when a search decision is made under higher search costs. Many of these effects were found to vary with individual differences in sensitivity to the reward environment parameters. Specifically, the ACC signal related to the average value of the foraging environment was correlated with behavioral variation in how much search value promoted decisions to search. Taken together, both the Hayden and Kolling studies suggest that the ACC is crucial for foraging decision-making, but information about the reward environment that

affects decision thresholds likely comes from input to the ACC from another source such as the striatum and neuromodulators such as dopamine. Variability in this complete neural circuit including the ACC and input from the striatum likely contributes to individual variation in foraging behavior.

5.1.3 Implication of Dopamine in Foraging Behavior

The work of both Ben Hayden and Nils Kolling described in the previous section suggests that the ACC contains important information about the overall value of searching the environment and the time spent in a reward patch. However, the neural correlates of the actual thresholding process that relies on this information remain unlear. It is likely either activity in other brain regions or neuromodulatory mechanisms play a role in encoding the individual properties of the reward environment, such as travel time between reward patches, decay rate of rewards within a patch, and average reward rate within the environment.

Theoretical work by Yael Niv and Mark Humphries describe potential roles for tonic dopamine and dopamine receptors in foraging behavior. The model developed by Humphries and colleagues suggests that striatal tonic dopamine and dopamine receptor activation are key contributors to the tradeoff between exploitation and exploration [60]. This is directly related to foraging behavior where an animal must decide whether to exploit the current reward patch or explore and search for a new one. Yael Niv and colleagues proposed a computational model for how tonic dopamine in the striatum may encode information about the average reward rate of the environment [59]. This theory states that the average reward rate acts as an opportunity cost such that when it

is high each wasted second is costlier. It is suggested that tonic dopamine in the striatum is the neural mechanism that encodes the average reward rate. This computational model accurately explains rodent behavior in a number of cost-benefit tradeoff experiments in which animals respond more quickly and endure greater energetic costs when the average reward rate is high compared to when it is low. If this theory holds true in a foraging context, reward environments with a shallow decay rate of rewards within a patch and a short travel time between reward patches would have the highest average reward rate and should thus be associated with the highest levels of striatal tonic dopamine. In contrast, reward environments with steep decay rate and long travel time would have a lower average reward rate and resultantly associated with lower levels of tonic dopamine in the striatum.

If dopamine does indeed help set the threshold for leaving one reward patch in search of another, then individuals with diminished dopamine function would be expected to have an impaired ability to set an optimal threshold. Indeed, it was found that patients with Parkinson's disease, off medication, stayed in reward patches for longer than was optimal, and that this deficit was reduced by treatment with dopaminergic medication [160]. While these data suggest that individuals with pathologically low levels of dopamine synthesis have an impaired ability to set a patch-leaving threshold, the question remains, however, does normal variation in dopamine function in the ACC and striatum play a key role in adjusting the patch-leaving threshold based on the current reward environment?

5.1.4 Dissociation of Neural Mechanisms Encoding Reward Timing and Magnitude

It is already known that dopamine neurons in the midbrain are sensitive to both reward magnitude and timing. Specifically, it has been shown that they increase their firing rate in response to a reward, and that this response increases as the magnitude of the received reward increases [3]. Furthermore, when an animal learns that a cue predicts future reward delivery, the dopamine neurons start to respond to the cue and not the reward itself [2]. However, when an expected reward is not received, the dopamine neurons decrease their firing rate at the exact time that they expected the reward to occur, demonstrating that midbrain dopamine neurons encode information about reward timing as well. However, more recent work has suggested that while midbrain dopamine neurons encode both reward magnitude and timing, the striatum is important for encoding reward timing only [161, 162]. Since optimal foraging behavior, as described by the MVT, depends on both the depletion rate of reward magnitude within a patch of rewards as well as the time it takes to travel between patches of rewards, it is possible that behavioral sensitivity to these two parameters of the reward environment may also be dissociable. Furthermore, if dopamine is involved in setting the reward patch leaving threshold based on these two parameters of the reward environment, the relationship between dopaminergic function and behavioral sensitivity to reward magnitude depletion rate and travel time between patches may also vary.

5.2 Methods

5.2.1 Study Participants

Fifty-seven healthy volunteers aged 21.4 to 57.6 years (mean 35.4±9.9, 29 females) were recruited from the local Washington DC community. Subjects were screened by physician-administered physical and neurological examination, standardized clinical interview (SCID) [136], laboratory tests, and structural MRI read by radiologist to rule out psychiatric, neurological, and major medical illness. The group consisted of 51 individuals of Caucasian descent, five African Americans, and one participant of Asian descent. Of the 57 participants, 51 completed the [^{18}F]-FDOPA PET scan (mean age 35.3±9.9, 25 females), 45 completed the [^{11}C]-NNC112 scan (mean age 35.3±9.9, 20 females), and 42 completed the [^{18}F]-Fallypride scan (mean age 35.6±9.7, 17 females). One participant was excluded due to behavior that suggested they were not following the task instructions (absence of any leave decisions in one of the blocks of the task). All participants provided informed consent and were compensated for their participation. Study procedures were approved by the NIH Combined Neurosciences Institutional Review Board and Radiation Safety Committee.

5.2.2 Patch Foraging Behavioral Task

To assess foraging decision-making, participants played a computer-based game in which they foraged for apples (see schematic in **Figure 13**). This task was previously developed and published by Sara Constantino [158]. Subjects were shown an apple tree and asked to decide whether to stay at the

current tree and harvest it for apples, or leave and search for a new tree. If they decided to stay, they would receive a certain number of apples, shown below the tree. The apples earned were summed over the entire experiment and converted to monetary payment that was added to the study compensation. After staying at a tree and harvesting it, the number of apples remaining in the tree would decrease according to a depletion rate, similar to how a tree in the wild would gradually run out of apples the longer that an animal ate from it. Subjects would then make the stay or leave decision again. If the participants decided to leave, they had to endure a travel time delay until they reached a new tree, which started out with an average value of ten apples. There were an infinite number of new trees available to travel to. Participants completed this game in four different reward environments that varied in travel time delay ("short" 6 seconds or "long" 12 seconds) and reward depletion rate ("steep" 0.88 or "shallow" 0.94). Each reward environment, or block, lasted a fixed duration of six and a half minutes. Travel time and depletion rate remained constant throughout the block and the blocks were presented in a random order across participants. If participants did not make a decision within one second, they received a warning and had to wait two and a half seconds to make another decision. The starting amount of rewards in a tree was drawn from a normal distribution with a mean of 10 and standard deviation of 1 (maximum 15). The reward depletion rates within a patch were drawn from beta distributions such that the "steep" environments had a mean of 0.88 (alpha = 14.908728, beta = 2.033008) and the "shallow" environments had a mean of 0.94 (alpha = 31.55811, beta = 1.896899).

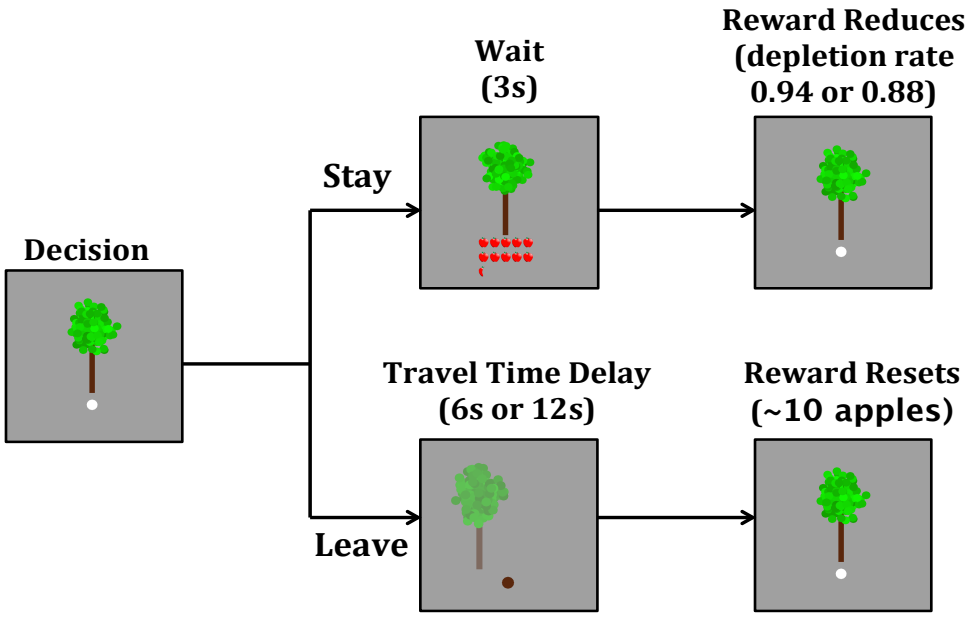


***Figure 13**: Schematic of patch foraging task.*
Figure adapted from Constantino, 2015 [158].

5.2.3 Behavioral Measures of Interest

To assess behavioral sensitivity to the variables in this task, I calculated the total change in threshold for leaving a patch between the reward environment with the highest average reward rate (short travel time and shallow depletion rate) and the one with the lowest average reward rate (long travel time and steep depletion rate). In addition, to assess whether there was a dissociation between changes related to reward timing and magnitude, I determined behavioral sensitivity to these two parameters. To calculate travel time sensitivity, I took the difference between the average threshold for leaving in the two reward environments with the short travel time and the average threshold for leaving in the two reward environments with the long travel time. Threshold changes due to depletion rate were calculated as the difference between the average threshold for leaving in the reward environments with a shallow depletion rate

and the average threshold for leaving in the reward environments with the steep depletion rate (i.e. shallow threshold – steep threshold).

5.2.4 PET Imaging Methods

The PET scans were collected as described in Section 3.4 and preprocessed as described in Section 3.5. These scans were all collected on separate days from the behavioral testing. Region of interest data were extracted from the basal ganglia (dorsal putamen, dorsal caudate nucleus, ventral striatum, and dopaminergic midbrain; see Section 3.5 and **Figure 7**). In addition, given the strong a priori knowledge about the role of the ACC in foraging decision-making, an ROI was created as a 5mm-radius sphere centered on the peak voxel encoding the average value of the foraging environment in the seminal human fMRI study from Nils Kolling (**Figure 14**).



***Figure 14**: Anterior cingulate cortex region of interest.*
This region was created as a 5mm sphere centered on the peak voxel encoding the average value of the foraging environment in a seminal human fMRI study [29].

5.2.5 Principal Component Analysis of PET Data

In order to take a comprehensive look at dopaminergic function and reduce the dimensionality of our analyses given the five different ROIs for three different PET tracers, we used a principal component analysis (PCA) to extract

patterns of covariance in the dopamine PET data. Only participants who completed all three PET scans were included in this analysis (n=39). PET values were corrected for age and gender and z-normalized before being input into the PCA analysis. Z-normalization involved subtracting the mean and dividing by the standard deviation for each data point, so the resulting mean of the data was approximately 0 and the standard deviation was approximately 1. This was done so that all PET data values were on similar scales prior to running the PCA, which is necessary because the typical values for the three PET tracers used vary by multiple orders of magnitude. Only components with eignenvalues greater than one were used in the regression analysis with foraging behavioral measures of interest.

5.2.6 Statistical Analyses

Regression analyses were conducted in IBM SPSS Statistics 22 to assess the relationship between foraging behavioral measures of interest and principal components of dopamine variation. To check which dopamine PCA components were significantly correlated with the total change in patch leaving threshold, the total change in threshold between the short-shallow reward environment and the long-steep reward environment was used as the dependent variable, and the PCA components were input as independent variables in a stepwise linear regression. Using a stepwise regression reduces overfitting and only keeps the variables in the model that significantly explain the behavioral variation. Stepwise linear regression is a method for systematically adding and removing independent variables from a linear model based on their significance [163]. The

initial model includes only a constant term. At each step, the remaining independent variable that maximizes the F-statistic is temporarily added to the linear model and the resulting p-value is compared to that of the model without that variable included. The independent variable remains in the model if the p-value of the F-statistic improves by at least 0.05. All independent variables included in the model are then re-evaluated and any terms in the model that have p-values greater than 0.1 are removed. This process of adding and removing variables is repeated for all independent variables. To test for a dissociation between behavioral sensitivity to changes in reward magnitude depletion rate and travel time, each of the four dopamine PCA component was used as the dependent variable in a stepwise regression with the two behavioral measures as the independent variables. A statistical threshold of $p<0.05$, uncorrected, was used to assess significance.

To follow-up on the PCA results and gain an understanding of the contributions of the individual PET tracers, we ran both native-space ROI (bilateral regions within the basal ganglia: dorsal putamen, dorsal caudate nucleus, ventral striatum, and dopaminergic midbrain; see Section 3.5) as well as whole-brain voxelwise regression analyses in SPSS and SPM, respectively, to test for correlations between the total change in reward patch leaving threshold and PET values for the individual tracers (using the complete sample). Results reported here meet a statistical threshold of $p<0.05$ (for ROI) and $p<0.005$ (for voxelwise), uncorrected, after controlling for age and gender. In addition, for the voxelwise analysis the AFNI tool 3dClustSim was used to determine the cluster

extent threshold for cluster corrected significance of $p<0.05$ (with an initial voxelwise threshold of $p<0.005$ or $z>2.58$) and the findings meeting this threshold are noted in the results.

5.3 Results

5.3.1 Behavioral Results

According to the MVT, the optimal exit thresholds for leaving a reward patch for the specific environment parameters used in this task were as follows: long steep = 5.88, long shallow = 6.56, short steep = 7.74, short shallow = 8.04. Since the task parameters were drawn from a beta distribution, the optimal values were calculated as the average result from 100,000 simulations of the task using the criteria defined by the MVT that it is optimal to leave the current patch when the predicted reward from the next harvest falls below the average reward rate for the environment. MVT simulations were run in MATLAB.

For the participants who completed this study, the average thresholds for leaving a reward patch generally followed the same pattern as the optimal thresholds (see **Figure 15**: long steep = 4.17, long shallow = 4.77, short steep = 5.30, short shallow = 5.58), however the averages were consistently lower than the optimal thresholds. The total change in patch leaving threshold between the short shallow environment and the long steep environment ranged from -2.16 to 5.22, with a mean of 1.41 and standard deviation of 1.83. The threshold change due to travel time differences (short – long) ranged from -2.33 to 4.44, with a mean of 0.97 and standard deviation of 1.30. Lastly, the threshold change due to

decay rate differences (shallow – steep) ranged from -1.92 to 2.83, with a mean of 0.44 and standard deviation of 1.12. Behavioral sensitivity to travel time and decay rate parameters (quantified by the amount of change in average patch leaving thresholds) were uncorrelated (Pearson r=0.137, p=0.314; **Figure 16**).

5.3.2 PET Data PCA Results

From the PCA analysis, four patterns of dopamine variation were identified with eigenvalues greater than one (see **Figure 17** for scree plot of component eigenvalues). These components account for 29.8%, 22.3%, 13.8%, and 8.1% of the variation in the data, respectively (**Figure 18**). Variables with component weighting values between -0.2 and 0.2 are whited out for visualization since their contribution is minimal. The first component describes a pattern of high

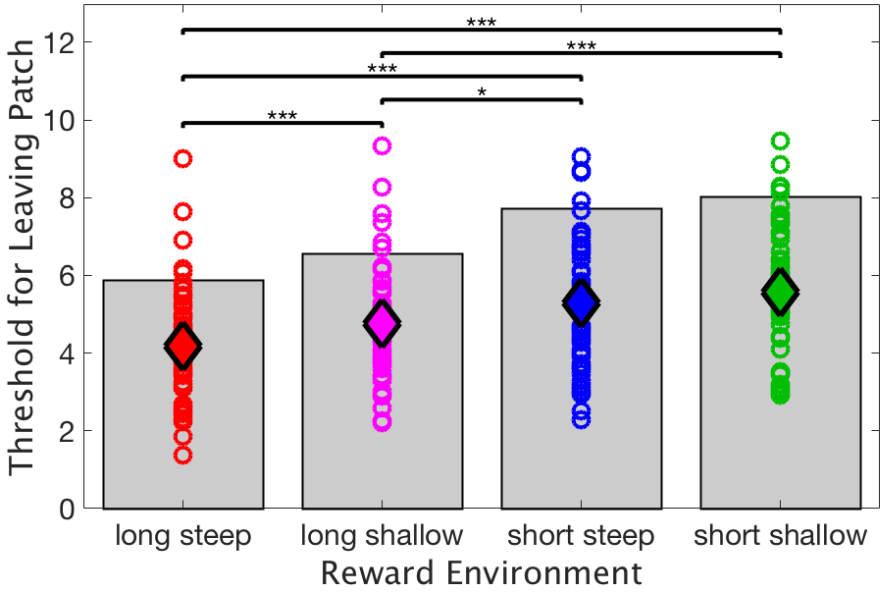


***Figure 15**: Foraging Behavioral Results.*
*The average threshold for leaving a reward patch is shown for each subject (open circle) for each reward environment block. The optimal thresholds as calculated from the marginal value theorem [1] are indicated with the gray bars. The group average thresholds are denoted with the colored diamonds. Significance is indicated as follows: * = p<0.05, *** = p<0.001.*

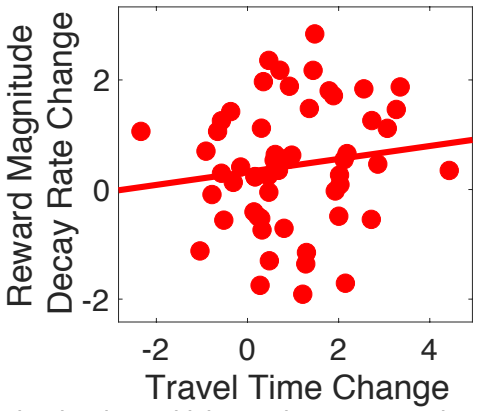


***Figure 16**: Correlation of behavioral sensitivity to change reward magnitude decay rate compared to change in travel time (r=0.137, p=0.314)*

dopamine receptor availability and low resting tonic dopamine. The second component has high tonic dopamine and high striatal D_2 receptor availability (but low in the midbrain). The third component is a pattern of high D_1 receptor availability, low D_2 receptor availability and moderately high tonic dopamine in the ventral striatum, putamen, and ACC. Finally, component 4 is mostly driven by high D_2 receptor availability in the midbrain along with moderately high resting tonic dopamine values in the ACC, ventral striatum, and midbrain, D_1 and D_2 receptor availability in the ventral striatum, and low D_2 receptor availability in the ACC.

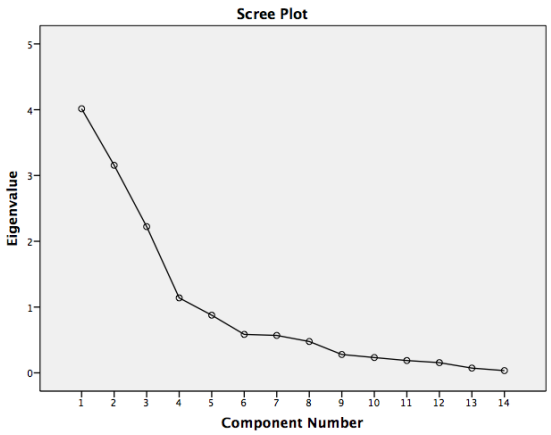


***Figure 17**: Scree plot of dopamine PET PCA component eigenvalues. Components 1-4 have eigenvalues greater than one and were thus retained for regression analyses with foraging behavior.*

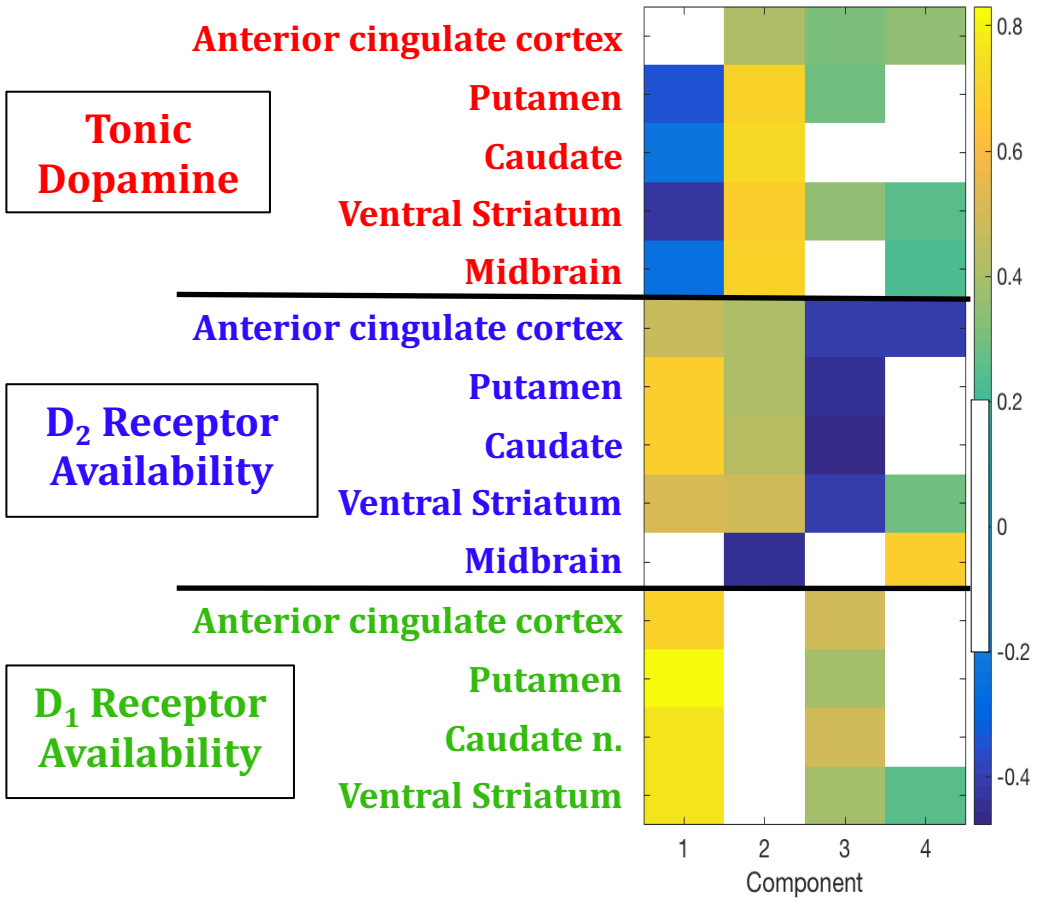


***Figure 18**: Results of dopamine PCA analysis.*
Four components had eigenvalues greater than one, suggesting that they contributed significantly to the variation in the data. In order from one to four, these components explained 29.8%, 22.3%, 13.8%, and 8.1% of the variation, respectively.

5.3.3 Correlations Between Foraging Behavior and Dopamine PET Data Principal Components

5.3.3.1 Total change in patch leaving threshold

Total change in patch leaving threshold was found to be correlated with both component 1 and component 4, using a stepwise regression (component 1: r=0.377, p=0.020; component 4: r=0.349, p=0.032; see **Figure 19**). Both were positive correlations where individuals with a greater component score changed their leaving thresholds more based on parameters of the reward environment.

Together, these two components described total change in patch leaving threshold very well (complete regression model F=6.257, r=0.513, p=0.005). There were no significant correlations with total change in patch leaving threshold and components 2 (r=-0.030, p=0.856) or 3 (r=0.088, p=0.599).

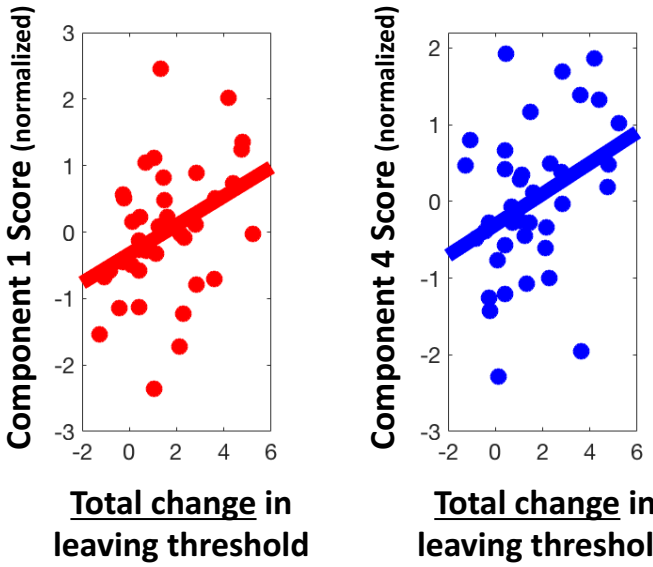


***Figure 19**: Component correlations with total change in patch leaving threshold (component 1: r=0.377, p=0.020; component 4: r=0.348, p=0.032)*

5.3.3.2 Change in leaving threshold due to travel time and decay rate

Component 1 showed a dissociation between behavioral sensitivity to travel time changes (short – long) and decay rate changes (shallow – steep) using a stepwise regression. Only patch exit threshold due to travel time, but not decay rate, was significantly correlated with component 1 score (F=4.568, r=0.336, p=0.039, see **Figure 20**). None of the other components were significantly correlated with threshold change due to either travel time or decay rate.

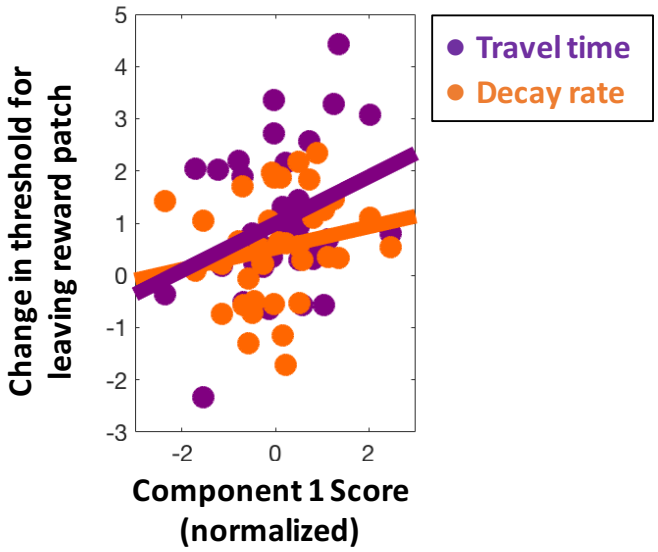


***Figure 20**: Correlation between component 1 and change in exit threshold due to travel time changes and decay rate changes.*
A stepwise regression showed that the component 1 score was positively correlated with change in exit threshold due to travel time (r=0.336, p=0.039) but not decay rate (r=0.200, p=0.228).

5.3.4 Correlations Between Total Change in Patch Leaving Threshold and Individual Dopamine PET Tracer Data

5.3.4.1 Tonic Dopamine ([^{18}F]-FDOPA)

There were no significant correlations or trends between the total change in patch leaving threshold and [^{18}F]-FDOPA K_i values in any of the basal ganglia ROIs. In the whole-brain voxelwise analysis we found positive correlations between the total change in reward patch leaving threshold and [^{18}F]-FDOPA K_i (related to tonic dopamine and dopamine presynaptic synthesis capacity) in key regions of the reward network. Specifically, there were large clusters in the left OFC (peak voxel (-33, 42, -24), $p_{uncorrected}$=2.6e-4) and ventral striatum (peak voxel (-27, 0, -14), $p_{uncorrected}$=0.0014) that met a cluster-corrected threshold of z>2.58, p<0.05 (see **Figure 21**). In addition, there was a smaller cluster (that did not meet cluster-level significance) in the right OFC (peak voxel (27, 44, -24),

$p_{uncorrected}$=0.0032). In addition, we also saw a positive correlation between total change in patch leaving threshold and [^{18}F]-FDOPA K_i in the ACC at a less stringent statistical threshold of $p_{uncorrected}$<0.01 (peak voxel (-2, 40, 16), $p_{uncorrected}$=0.0086) (see **Figure 22**). There were no significant negative correlations between [^{18}F]-FDOPA K_i and total change in patch leaving threshold.

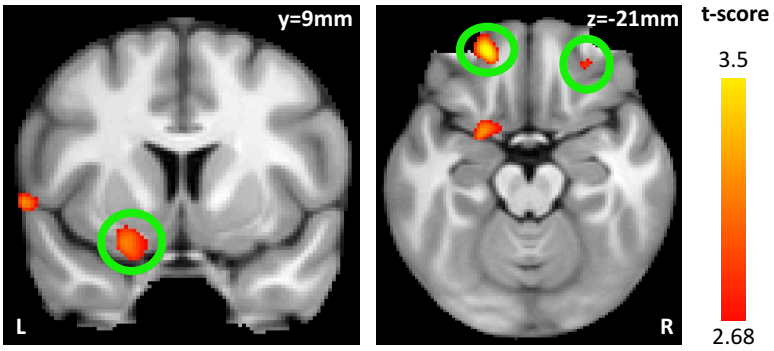


***Figure 21**. Positive correlations between [^{18}F]-FDOPA K_i and total change in exit threshold. Image is shown at $p_{uncorrected}$<0.005. Key regions in the reward network are circled in green including the left ventral striatum and bilateral OFC. The findings in the left OFC and left ventral striatum meet a cluster-corrected significance threshold of z>2.58, p<0.05.*

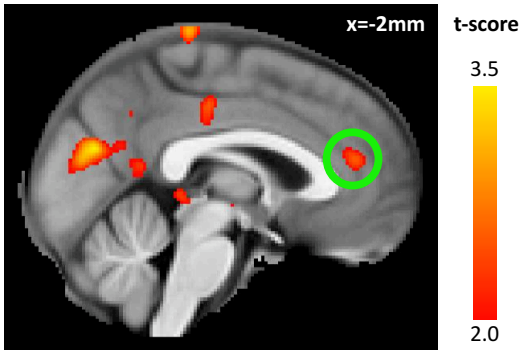


***Figure 22**. Trend towards positive correlation between [^{18}F]-FDOPA K_i in the ACC (-2,40,16) and total change in patch leaving threshold ($p_{uncorrected}$=0.0086). Shown at a threshold of t>2.0.*

5.3.4.2 Dopamine D_2 Receptor Availability ([^{18}F]-Fallypride)

The basal ganglia ROI analysis yielded no significant correlations between total change in patch leaving threshold and dopamine D_2 receptor availability,

however, there were trends in the putamen (r=0.261, p=0.095) and caudate nucleus (r=0.269, p=0.085). In the whole-brain voxelwise analysis, we found positive correlations between total change in patch leaving threshold and dopamine D_2 receptor availability in the left OFC (peak voxel (-33, 42, -24), $p_{uncorrected}$=5.4e-5), putamen (right: peak voxel (24, 0, -2), $p_{uncorrected}$=9.9e-4; left: peak voxel (-28, 6, -6), $p_{uncorrected}$=4.2e-4) and caudate nucleus (right: peak voxel (-9, 0, 16), $p_{uncorrected}$=6.7e-5; left: peak voxel (-15, 6, 8), $p_{uncorrected}$=0.0012) (see **Figure 23**). All of these regions meet cluster-corrected significance (z>2.58, p<0.05).

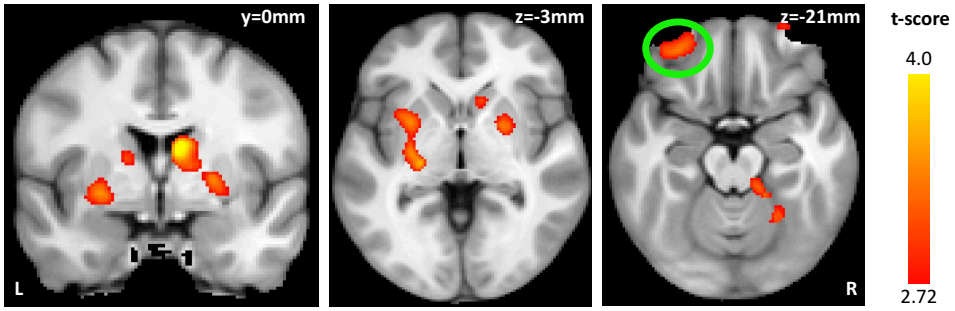


Figure 23*. Positive correlations between total change in patch leaving threshold and D_2 receptor availability in the putamen, caudate nucleus, and left OFC (circled).*
Image is shown at a threshold of p<0.005, although all listed regions are significant at cluster-corrected level of z>2.58, p<0.05.

5.3.4.3 Dopamine D_1 Receptor Availability ([^{11}C]-NNC112)

In the basal ganglia ROI analysis, we found a significant correlation between the total change in patch leaving threshold and D_1 receptor availability in the ventral striatum (r=0.324, p=0.034) as well as a trend in the putamen (r=0.263, p=0.088). In the whole-brain voxelwise analysis, we found positive correlations in many regions including the ventral striatum (left: peak voxel (-27, 8, -12), $p_{uncorrected}$=4.8e-4; right: peak voxel (32, 8, -8), $p_{uncorrected}$=0.0016) and

bilateral OFC (left: peak voxel (-26, 16, -16), $p_{uncorrected}$=1.1e-4; right: peak voxel (27, 21, -18), $p_{uncorrected}$=2.9e-5) (see **Figure 24**). All of these regions were significant at a cluster-corrected threshold of z>2.58, p<0.05.

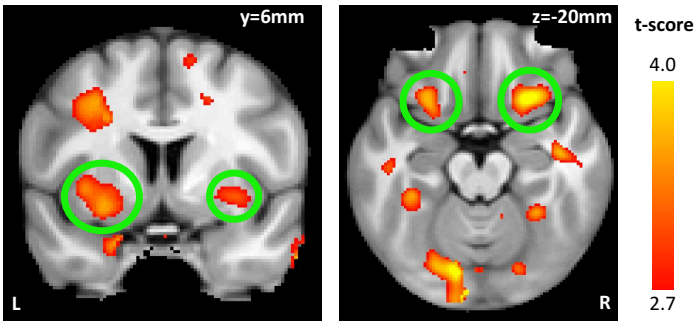


***Figure 24**. Positive correlations between total change in patch leaving threshold and D_1 receptor availability in regions including the bilateral ventral striatum and OFC (circled). Image is shown at a threshold of p<0.005, but all listed regions meet a cluster-corrected threshold of z>2.58, p<0.05.*

5.4 Discussion

In conclusion, we found that the amount individuals change their foraging behavior based on the parameters of the reward environment is correlated with their pattern of dopamine synthesis capacity (or tonic dopamine) and receptor availability throughout the basal ganglia and ACC. In other words, the levels of tonic dopamine and D_1 and D_2 receptor availability that a person has may define their sensitivity to changes in dopamine levels that occur in response to changes in the reward environment. This finding supports computational predictions made by Yael Niv and colleagues that tonic dopamine encodes the average reward rate of the environment [59]. Specifically, in the reward environment with the short travel time between reward patches and the shallow depletion rate within a patch, the average reward rate is the highest. On the other hand, the average reward rate is the lowest in the environment with the long travel time and

the steep depletion rate. According to Yael Niv's theory, levels of striatal dopamine should vary as the average reward rate of the environment changes. Our hypothesis was that dopamine levels set the threshold for when to leave one reward patch to search for another which means that the exit threshold between the environments with the highest and lowest average reward rate should change in proportion to an individual's sensitivity to changes in tonic dopamine levels. If Tony Grace's theory that baseline levels of tonic dopamine may modulate the response to dopamine release via homeostatic mechanisms is correct [58], then our results support this prediction.

First, we demonstrated that the total change in patch exit threshold between the reward environments with the highest and lowest average reward rate is positively correlated with two separate patterns of dopamine variability. The first pattern consists of low resting tonic dopamine levels coupled with high D_1 and D_2 receptor availability, which may represent a state of increased reactivity to phasic dopamine release [58]. Specifically, this conclusion is supported by findings from lesion-induced decreases in dopamine levels which leads to reduced autoreceptor stimulation and subsequent increases in dopamine synthesis and release [164-166], increased dopamine postsynaptic receptors [167], and increased activity of the enzyme responsible for synthesizing dopamine (tyrosine hydroxylase) [168]. Furthermore, the positive correlation between dopamine receptor availability and behavioral sensitivity to changes in the reward environment was further confirmed with our whole-brain voxelwise analysis and supports prior work showing that dopamine receptors

have been shown to be important for weighing costs and benefits in an effort-based task in rats [169].

The second pattern of dopamine variability that was correlated with the total change in patch exit threshold is mostly driven by high D_2 receptor availability in the midbrain, a region where D_2 receptors play a key role in the autoregulation of dopamine release throughout the brain [170]. Individuals with higher D_2 receptors in the midbrain would theoretically have increased regulatory control of their dopamine system, allowing for larger changes in dopamine levels and thus foraging behavior as the average reward rate of the environment changes. Although there is work showing that mice completely lacking D_2 autoreceptors display a supersensitivity to cocaine-induced dopamine release and enhanced motivation for food reward [144], it has also been shown that autoreceptors play a key role in regulating the intrinsic pacemaker activity of dopamine neurons that underlies tonic dopamine levels [40, 171, 172]. In our study, the behavioral measure of interest is how much individuals adjust their foraging behavior as the reward environment changes, therefore, greater regulatory control over dopamine pacemaker activity would be a beneficial trait that could allow greater changes in tonic dopamine as the average reward rate varies. In addition, component 4 also included a positive contribution of tonic dopamine in the ACC, ventral striatum, and midbrain, as well as dopamine D_1 and D_2 receptor availability in the ventral striatum. Taken together with our voxelwise results showing that the total change in patch leaving threshold was positively correlated with tonic dopamine in the ventral striatum and OFC (with a

trend in the ACC) as well as D_1 and D_2 receptor availability throughout the striatum and the OFC, these findings demonstrate that dopamine synthesis capacity and receptor availability throughout the reward network increases behavioral sensitivity to parameters in the foraging reward environment.

Another conclusion of this study is that the correlation between the pattern of dopamine synthesis and receptor availability in component 1 (low tonic dopamine and high receptor availability) and changes in foraging behavior is driven by changes in travel time between reward patches. However, there were no significant correlations between any of the dopamine PET components and changes in exit threshold due to changes in decay rate. This finding suggests a dissociation between the dopaminergic basis of behavioral sensitivity to reward timing and magnitude, supporting prior work showing a dissociation between the neural circuitry encoding reward timing and magnitude [161, 162].

While this is the first study to characterize the role of dopamine synthesis capacity and receptor availability in foraging behavior in humans, there are limitations to our study that should be kept in mind. Specifically, PET imaging is the only way to non-invasively directly measure the dopamine system in the living human brain, which has many drawbacks compared to methods used in animal research (e.g. direct neural stimulation, voltammetry, microdialysis with high-performance liquid chromatography, and optogenetic techniques). With the three PET tracers that we used in this study, none of them measure dopamine release. In addition, these tracers are not readily displaceable by exogenous dopamine and they were all collected at rest, so we are unable to quantify tonic dopamine

or receptor availability during the foraging task itself. In addition, the [^{18}F]-FDOPA tracer quantifies the activity of aromatic l-amino acid decarboxylase (AADC), the enzyme that converts L-dopa to L-dopamine. However, dopamine can subsequently be converted to norepinephrine in neurons containing the enzyme dopamine beta hydroxylase. Furthermore, AADC is also the enzyme that converts 5-OH-tryptophan to serotonin, therefore, [^{18}F]-FDOPA signal in the ACC where all three of these neurotransmitters are common is not specific to dopamine [173, 174]. However, norepinephrine has already been implicated in the trade-off between exploitation and exploration [175], so demonstrating its role in foraging behavior would be of great interest to the field.

Despite the limitations to interpretation pointed out above, this study is the first to show a direct correlation between foraging behavior and dopamine synthesis capacity and receptor availability in humans. Further work is needed to validate these findings and tease apart the specific roles of tonic dopamine changes and binding to specific receptors. However, our results provide a potential mechanistic explanation for how neural activity in the ACC measured in other studies could relate to a change in patch exit threshold based on the specific parameters of the reward environment.

6

Limitations and Development of PET Methods

Contents

Abstract
6.1 Limitations of Current PET Methods
6.1.1 Limitations of cortical PET data
6.1.2 Partial volume effects
6.2 Surface-based PET Imaging Methods
6.2.1 Introduction
6.2.2 Methods
6.2.2.1 Participants
6.2.2.2 Imaging data acquisition and preprocessing
6.2.2.3 Partial volume correction
6.2.2.4 Cortical surface sampling and smoothing
6.2.2.5 Kinetic modeling
6.2.2.6 Performance criteria and methods compared
6.2.3 Results
6.2.4 Discussion
6.3 Data-driven PET Parcellation: Application for Automated Optimal Reference Region Delineation
6.3.1 Introduction
6.3.1.1 Compartment Modeling
6.3.1.2 Current Methods for Reference Region Definition
6.3.2 Methods
6.3.2.1 Descriptive Model
6.3.2.2 Parameter Fitting and Error Weighting Function
6.3.2.3 Reference Region Voxel Selection
6.3.2.4 Test-Retest Reliability Measures
6.3.3 Results
6.3.3.1 Parameter Fitting
6.3.3.2 Reference Region Selection
6.3.3.3 Test-Retest Reliability of [^{18}F]-FDOPA Putamen K_i Values
6.3.4 Discussion
Chapter 6 Appendix

Chapter 6 Abstract

This chapter includes an introduction to the limitations of current PET methods as well as two methodological advancements that we have developed and implemented to address the limitations. Both techniques aim to improve the cortical signal of the PET data by (1) increasing the signal-to-noise ratio in the prefrontal cortex, where dopaminergic innervation is important, but much lower than that of the striatum and (2) optimizing the reference region that is used as a comparison region in non-invasive compartment models. The first method is a surface-based PET data analysis pipeline that involves registering a T1-weighted MRI scan to the PET data, sampling the PET data to the cortical surface, and then performing spatial smoothing and modeling on the cortical surface. The second method is a series of tools for data-driven parcellation of PET data which can then be used for automated optimization of reference region delineation.

6.1 Introduction

6.1.1 Limitations of Cortical PET Data

PET studies with tracers of the dopamine system often limit analyses to subcortical regions of interest due to the relatively low signal in cortical voxels compared to the basal ganglia. In addition, there are other potential methodological issues for the [^{18}F]-FDOPA PET tracer such that there is an apparently higher uptake rate in the adjacent white matter than in the cortical

gray matter. This is caused by a potential violation in the Gjedde-Patlak reference input model in white matter where a low tracer uptake results in an apparently flat decay curve in the later part of the scan, leading to a flawed calculation of high specific binding [174]. However, we know from post-mortem and rodent studies that cortical dopamine is important for cognition [176-178], is disrupted in patients with mental illnesses such as schizophrenia [179] and addiction [180, 181], and is affected by psychoactive drugs [182, 183], so an accurate in-vivo measurement of cortical dopamine in humans is essential for research paradigms probing the role of dopamine in cognition and alterations in mental health disorders.

6.1.2 Partial Volume Effects

PET data is susceptible to bias due to partial-volume effects caused by two distinct phenomena [184]. The first results in a blurring of the image because of the finite spatial resolution that is limited by the detector size, positron range before an annihilation event, photon noncollinearity, and acquisition mode, and is described as the point spread function (PSF) of the particular PET scanner [185]. The second phenomenon, called the tissue fraction effect, is caused by the fact that most voxels in a PET image include more than one type of tissue, which typically results in underestimation of gray matter signal and over estimation of white matter signal. The loss of signal from the gray matter into the surrounding tissues due to partial volume effects is called “spill-out”, while the contamination of signal from surrounding voxels is called “spill in”. The former phenomenon causing partial volume effects is limited by nuclear physics and

hardware engineering constraints, however, the latter can be corrected for with post-reconstruction methods using tissue segmentation information from a co-registered CT or MRI scan.

Partial volume correction (PVC) can be done at the ROI or voxelwise level. For PVC of ROI values, the Rousset method accounts for effects of spill-in and spill-out between each ROI pair [186]. In short, the Rousset method constructs a system of equations that describe the transfer of signal between each pair of ROIs using a PET simulation software and finds a solution to the system of equations that provides the "true" PET signal in each ROI. For voxelwise PVC, the Muller-Gartner (MG) algorithm corrects for both spill-out of signal from the gray matter into surrounding tissue as well as spill-in from adjacent white matter. The MG method utilizes MRI or CT tissue segmentations, smoothed by the scanner PSF, to subtract out the white matter signal and correct for the percent of gray matter signal in each voxel [187]. A commonly used modification of the MG algorithm (the "modified" MG method) uses the white matter signal that is calculated from the ROI-based Rousset method, rather than a hand-drawn drawn rectangular white matter ROI described in the original MG paper [188]. See Appendix A for a more detailed description of these PVC methods.

There have been mixed reports on the effects of PVC on PET data. One study that used volume-based three dimensional smoothing methods found that PVC improved gray matter signal in [^{11}C]-NNC112 data but actually made gray matter signal smaller and less reliable in [^{18}F]-FDOPA data [174]. However, it

has also been shown that PVC in conjunction with surface-based smoothing minimizes bias in cortical PET data [189]. It is important to note that different PVC methods can lead to different conclusions [190], so it is essential to choose the best PVC method for the question at hand and analysis methods used.

6.2 Surface-Based PET Imaging Methods

6.2.1 Introduction

Exploratory analyses are performed when no strong a priori hypothesis exists. Spatial smoothing is necessary for voxelwise exploratory analyses to reduce the noise present at a single voxel and to account for slight variations in anatomy across subjects. Most PET studies in the literature spatially smooth data volumetrically in three dimensions, which results in a blurring between the higher signal of the gray matter and the lower signal of the adjacent white matter and cerebrospinal fluid (CSF). One way to reduce this loss of signal is to sample the PET data to the cortical surface and then smooth in two dimensions along the surface of the gray matter, eliminating loss of signal through blurring into the white matter and CSF. Surface-based PET data analysis methods have been shown to increase signal-to-noise in cortical areas, thus improving power and decreasing the number of subjects needed to detect an effect of a given size [189]. Prior studies have used these methods with serotonin receptor, mGluR5, and TPSO tracers [191-194], however, they have not yet been tested with tracers of the dopamine system.

6.2.2 Methods

6.2.2.1 Participants

The surface-based PET analysis methods were tested on a cohort of 30 healthy humans from the local Washington DC community. Participants were screened by physician-administered physical and neurological examination, standardized clinical interview (SCID) [136], laboratory tests, and structural MRI read by a radiologist to rule out psychiatric, neurological, and major medical illness. Due to the fact that partial volume effects vary as the cortex thins during normal aging [190, 195], the testing group was selected to cover a wide range of ages varying from 21.6 to 72.5 with a mean of 41.5 and standard deviation of 14.5 years. Study procedures were approved by the NIH Combined Neurosciences Institutional Review Board and Radiation Safety Committee.

6.2.2.2 Imaging Data Acquisition and Preprocessing

Each participant completed all three PET scans of the dopamine system ([^{18}F]-FDOPA, [^{18}F]-Fallypride, and [^{11}C]-NNC112). Data were collected as described in Section 3.4. Each subject also completed multiple T1-weighted MRI scans that were averaged together processed with the Freesurfer software (Laboratory for Computational Neuroimaging, Martinos Center for Biomedical Imaging) to generate a deterministic segmentation of the cortex, white matter, and subcortical gray matter structures [196] used for region of interest based partial volume correction, as well as construction of models of the pial and white matter surfaces [197]. Subcortical segmentations were manually edited to clean up mistakes from the automatic Freesurfer process, which included the

commonly observed error of voxels in the nearby claustrum being classified as putamen. In addition, probabilistic segmentations of gray matter, white matter, and CSF were created with SPM8 (Wellcome Trust Centre for Neuroimaging, University College London), used for voxelwise partial volume correction.

6.2.2.3 Partial Volume Correction

The segmentations generated from the T1-weighted MRI images were coregistered to the PET data using SPM5. PVELab [188] was used for partial volume correction at both the ROI (using the Rousset method) and voxelwise levels (using the modified MG method). Voxelwise maps were thresholded to only include voxels with at least 20% gray matter intensity, as was previously shown to be an ideal threshold to reduce bias in cortical PET data [189]. More details about these two PVC methods can be found in Section 6.1.2 and Appendix A.

6.2.2.4 Cortical Surface Sampling and Smoothing

The cortical surfaces were converted from Freesurfer to SUMA (https://afni.nimh.nih.gov) format using @SUMA_Make_Spec_FS and then sampled onto a common standard grid with a linear depth of 141 [198]. Surfaces were warped to the PET image space using the SUMA tool ConvertSurface and PVC-corrected and uncorrected PET data were sampled to the surface by taking the mean of the middle 80% of the cortical ribbon (line between the equivalent nodes of the pial and gray matter surfaces), sampled at 10 steps, at each node on the surface using the SUMA tool 3dVol2Surf (see **Figure 25**). The middle 80% of the cortical ribbon was chosen as the sampled region to eliminate bias

due to slight misalignment of the PET and MRI data at the borders between gray matter and white matter and between gray matter and CSF. Finally, the data were smoothed along the cortical surface using SurfSmooth with Gaussian kernels of 15, 20, 25, 30, 35, and 40mm fwhm.

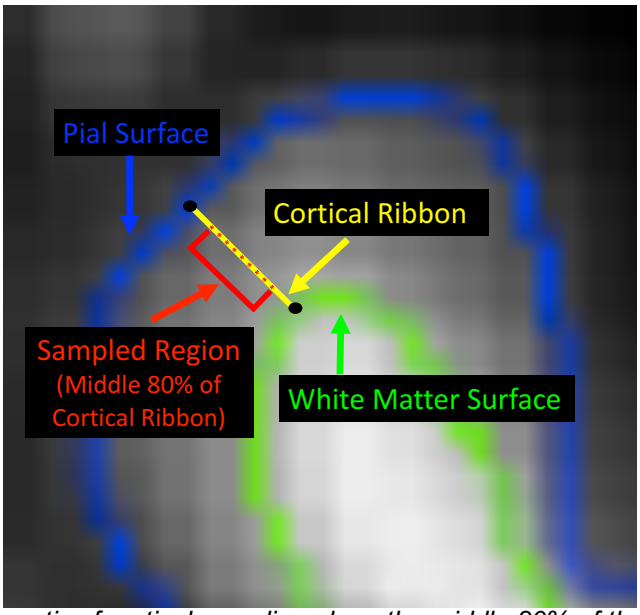


***Figure 25**: Schematic of cortical sampling along the middle 80% of the cortical ribbon.*

6.2.2.5 Kinetic Modeling

PET timecourses for each node on the surface were converted to nifti volumes with 3dUndump and 3dTcat and then input into PMOD for voxelwise kinetic modeling as described in Section 3.5. After kinetic modeling, the nifti volumes were converted back to surface-based 1D datasets using 3dmaskdump.

6.2.2.6 Performance Criteria and Methods Compared

The outcome measure of interest was how surface sampling and smoothing, as well as PVC, affect both the signal and noise in cortical PET data. Data from four different preprocessing pipelines were compared. Both of the following iterations were calculated from PET timecourse data with and without

PVC: (1) volume smoothing, kinetic modeling in PMOD, and performance measure extraction from volumetric regions of interest, (2) surface sampling, surface-based smoothing, kinetic modeling in PMOD, and performance measure extraction from surface-based regions of interest. See **Figure 26** for a schematic of the methods compared.

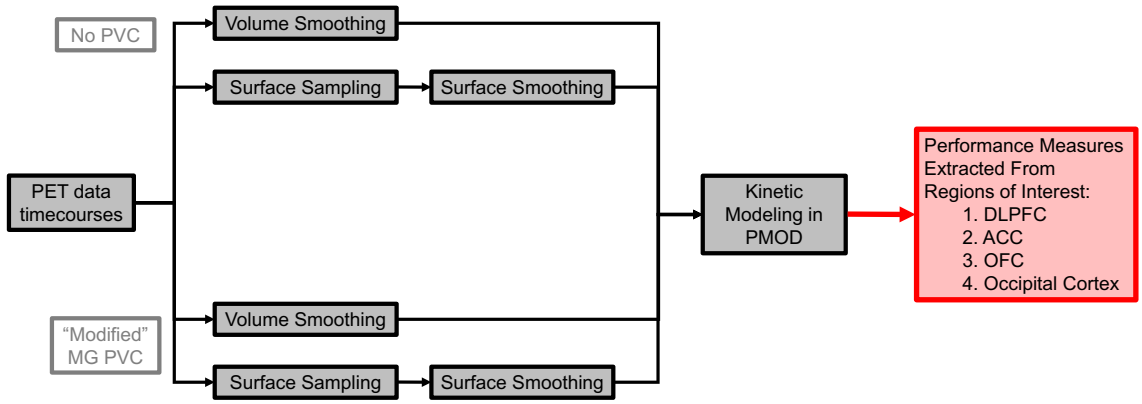


***Figure 26**: Schematic of the compared PET methods.*

Four cortical regions of interest were assessed, three of which are implicated in reward-guided behavior and decision-making (dorsolateral prefrontal cortex (DLPFC), anterior cingulate cortex (ACC), and the orbitofrontal cortex (OFC), as well as a control region (occipital cortex) with little to no expected specific binding of the dopaminergic PET tracers used in this study. The DLPFC mask was created based on landmarks from work by Patricia Goldman-Rakic using formal cytoarchitectonic methods in human post-mortem brains [199]. The DLPFC mask was created based on the volumetric T1-weighted MRI image and then sampled to the standard cortical surface mesh using the AFNI tool 3dVol2Surf. The other ROIs were created from a group average surface sampled to the standard surface mesh using the Freesurfer automatic cortical parcellation tools utilizing the Destrieux Atlas [200]. Specifically, the ROIs were comprised of the

following regions: ACC (anterior and mid-anterior cingulate gyrus and sulcus), OFC (orbital gyrus), and occipital cortex (occipital pole, as well as the superior, middle, and inferior occipital gyri and sulci). The sizes of the ROIs in terms of number of nodes in the standard surface mesh were as follows: DLPFC (left: 5538 nodes, right: 6456 nodes), ACC (left: 5763 nodes, right: 6774 nodes), OFC (left: 1171 nodes, right: 1335 nodes), occipital cortex (left: 10133 nodes, right: 11966 nodes). The cortical ROIs are shown in standard surface space in **Figure 27** and volumetric space in **Figure 28**. For the volumetric data, the cortical masks were warped to the subject's PET data native space using the FSL tool flirt prior to data extraction.

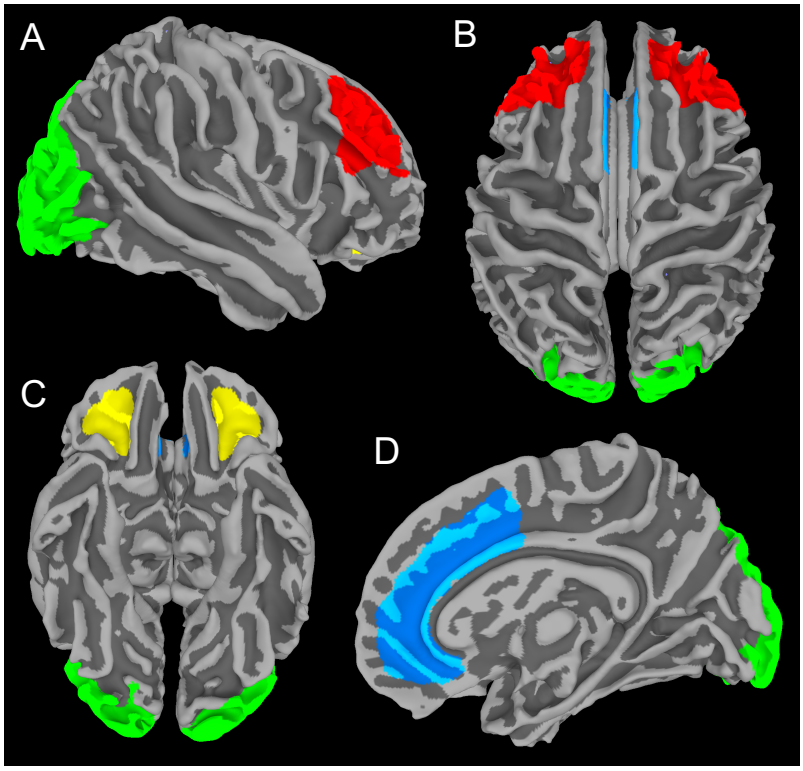


***Figure 27**: Cortical regions of interest in standard surface space. (DLPFC in red, ACC in blue, OFC in yellow, and occipital cortex in green). (A) view from the right, (B) superior view from above the brain looking down, (C) inferior view from below the brain looking up, and (D) medial view of the right hemisphere.*

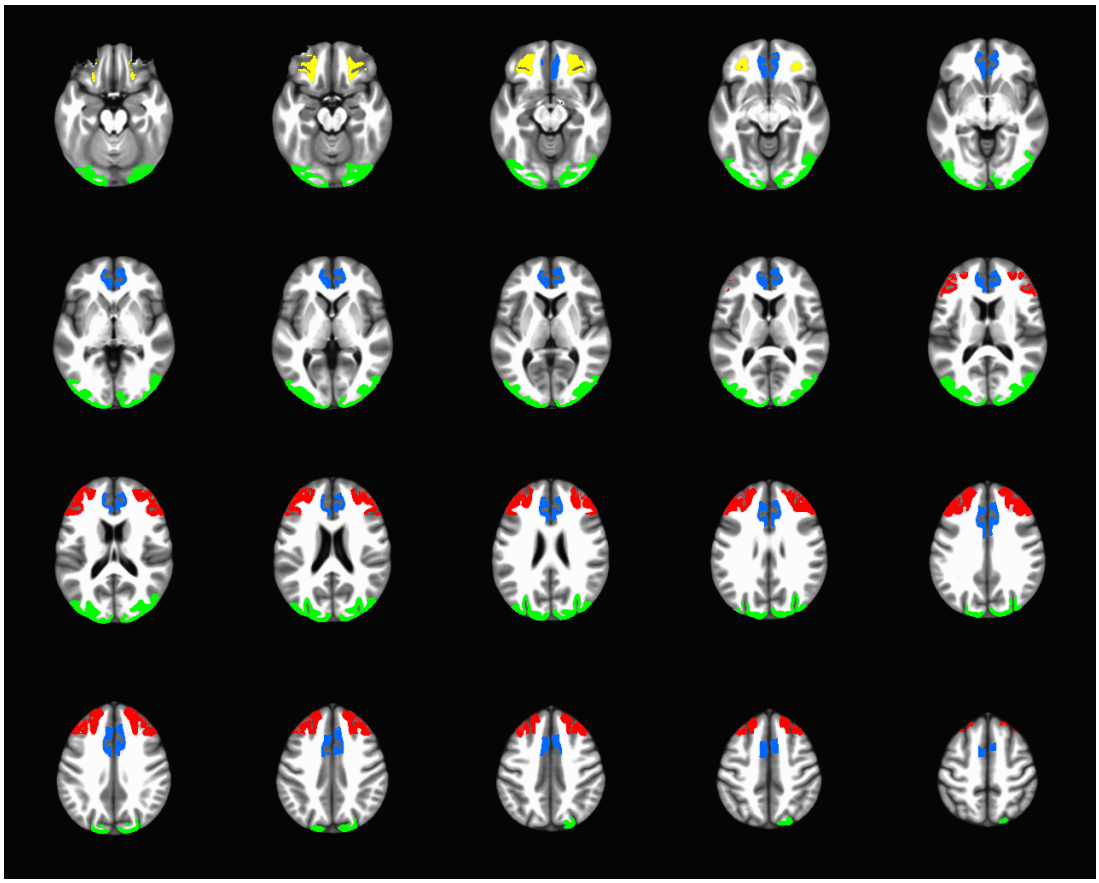


***Figure 28**:* Cortical regions in 3D volumetric space.
(DLPFC in red, ACC in blue, OFC in yellow, and occipital cortex in green).

To assess the performance of the four different PET methods, we quantified variations in signal and noise within the cortical ROIs of interest. To measure changes in the signal intensity we extracted mean PET values after kinetic modeling. Gray matter should have higher signal than CSF and white matter, especially in later time points, so an increase in signal should signify that less signal is lost into the surrounding tissue due to the blurring of signal from partial volume effects or three-dimensional smoothing. To measure changes in the noise of the signal, we calculated the coefficient of variation (CoV) across subjects (which is related to the effect size and can be used in power analyses). The CoV was calculated for each voxel or node as the standard deviation across

subjects divided by the mean across subjects. This value was then averaged across all voxels or nodes within an ROI to get our final value for comparisons.

6.2.3 Results

Partial volume correction led to a general increase in measured counts, especially around the edges of the cortex voxels contain a combination of gray matter and CSF (see **Figure 29**).

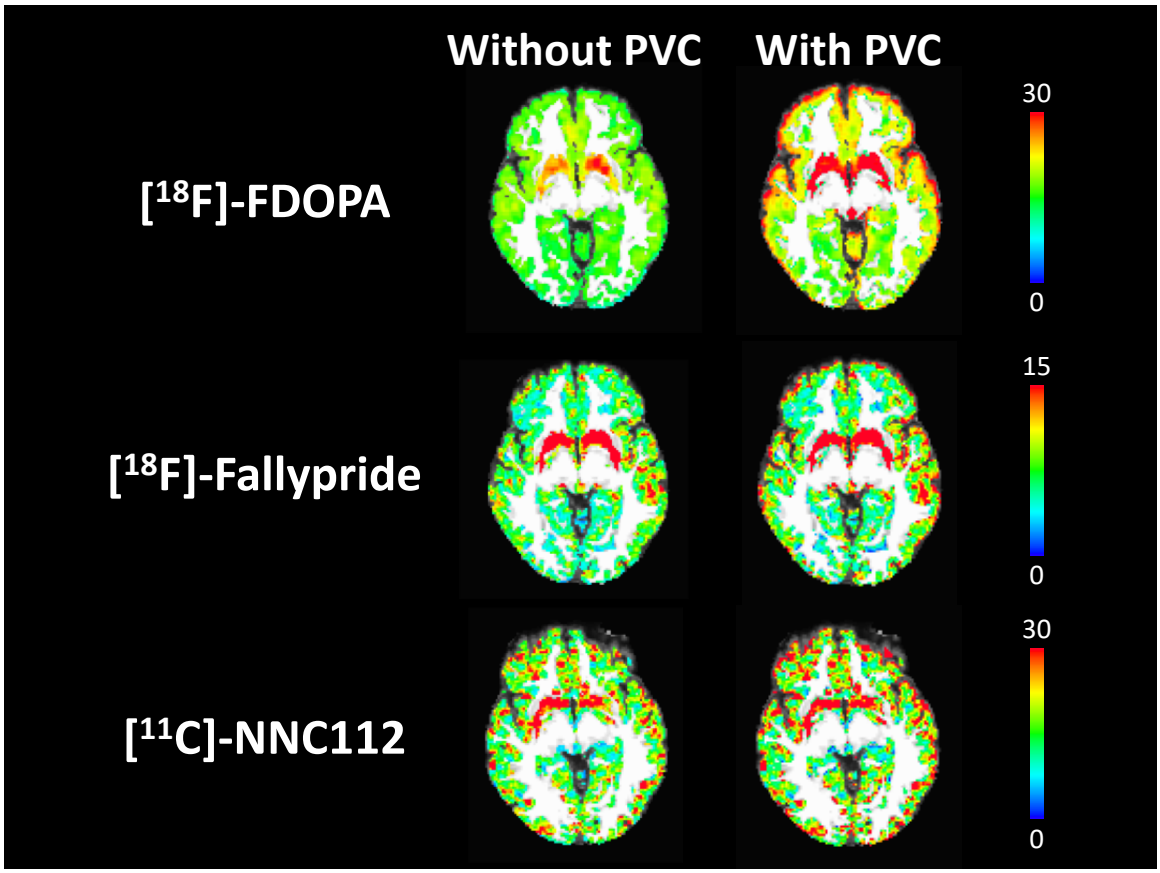


***Figure 29**. Effects of partial volume correction (PVC).*
Images shown are volume 20 of the PET data (before modeling with PMOD) from a representative subject. Both PVC and non-PVC data are shown after masking out voxels that contain less than 20% gray matter, although this step is not taken before sampling the non-PVC data to the cortical surface.

The effects of surface smoothing and partial volume correction on the modeled PET parameters showed two different patterns, depending on the PET scanner used. Data for an example region (DLPFC) are shown in **Figure 30** (the data for

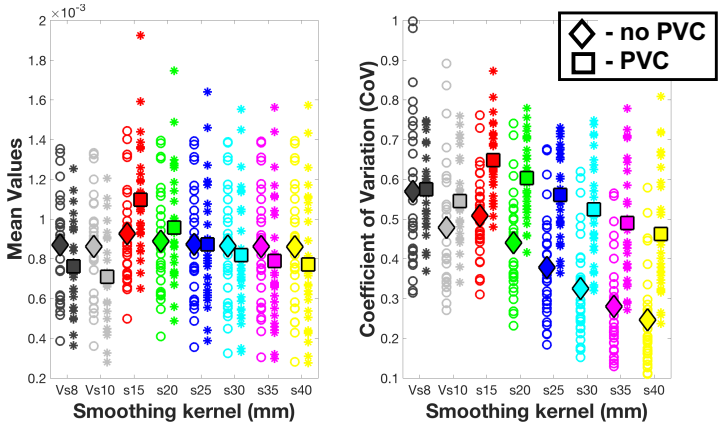
all other cortical regions of interest can be found in the Appendix at the end of this chapter). For the [^{18}F]-FDOPA data, which was collected on a GE Advance 3D scanner with a PSF of 7mm, we found that surface smoothing did not change the mean K_i values very much, however there was a slight increase in some regions at lower smoothing kernels (DLPFC and occipital cortex, but not ACC or OFC). Furthermore, surface smoothing decreased the CoV, although the CoV was greater with surface smoothing at the lower smoothing kernels (15mm and 20mm) in all regions except the occipital cortex. Lastly, PVC generally increased the mean values and CoV in the surface smoothing pipeline, but decreased mean K_i values in the volume-smoothing pipeline.

For the [^{18}F]-Fallypride and [^{11}C]-NNC112 data, which were collected on a Siemens high-resolution research tomograph (HRRT) scanner with a PSF of 3mm, we found that surface smoothing increased the mean values and decreased the CoV. In addition, PVC also increased the mean values in the surface-smoothing pipelines, but the CoV increased at lower kernels (in the DLPFC and OFC) or didn't change (ACC and occipital cortex) with PVC. PVC did not change the volume-smoothed data mean values or CoV much.

DLPFC Results

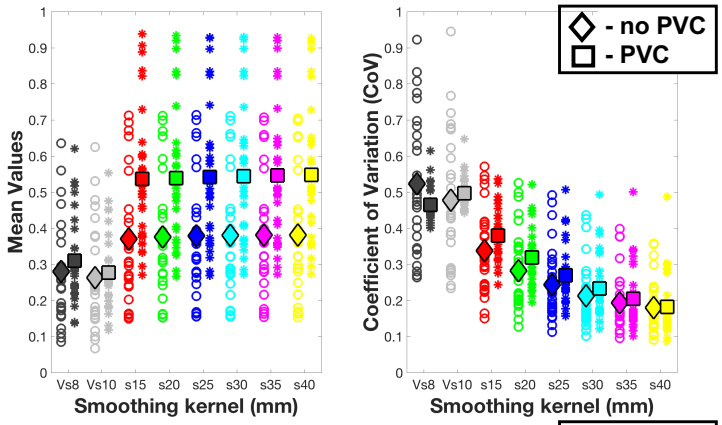
GE Advance Scanner (PSF 7mm)

[^{18}F]-FDOPA



Siemens HRRT Scanner (PSF 3mm)

[^{18}F]-Fallypride



[^{11}C]-NNC112

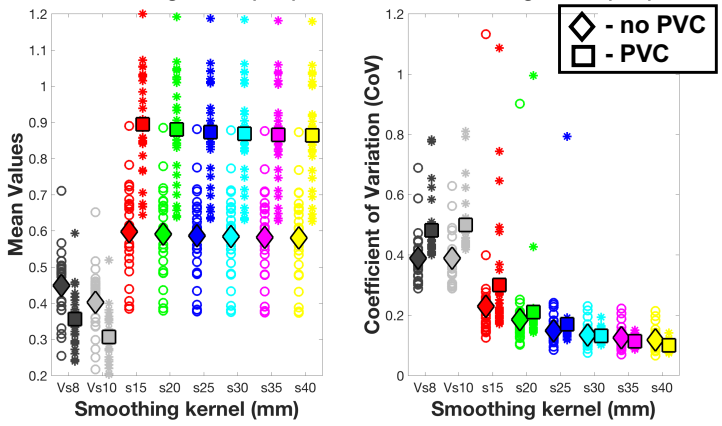


***Figure 30**. Effects of surface smoothing and PVC on parameter values and CoV in the DLPFC. Volume-based smoothing data are shown in gray scale (Vs8 - 8mm fwhm in dark gray; Vs10 - 10mm fwhm in light gray) and the surface-smoothing data are shown in color ranging from 15mm (red) to 40mm (yellow) (s15-s40).*

6.2.4 Discussion

In conclusion, we found that surface-based smoothing increases cortical signal and decreases noise for the two PET tracers that were collected on the Siemens HRRT PET scanner ([^{18}F]-Fallypride and [^{11}C]-NNC112). Compared to the GE Advance 3D scanner ([^{18}F]-FDOPA) that has a point spread function (related to spatial resolution) of 7mm, the HRRT scanner has a PSF of 3mm, which is an important difference since the thickness of the cerebral cortex in humans ranges from 1 to 4.5mm, with an average thickness of approximately 2.5mm [201].

In addition, as we predicted, partial volume correction, which uses tissue segmentation information from an MRI scan to correct for the contribution of more than one tissue type in a single voxel, increased the mean PET parameter value for all of the surface-based methods. However, PVC also increased the CoV in almost all of the tracers and cortical regions, demonstrating a trade-off between signal and noise. This effect may be in part caused by the particular PVC algorithm we used (the “modified” MG algorithm), which is a commonly used method for voxelwise PVC, but is sensitive to the amount of gray matter thresholding that is applied (20% in our case). This threshold was based on a prior publication demonstrating that it resulted in the lowest bias of the data [189], however, that study used PET data from an HRRT scanner. In our case, the increase in CoV with PVC was greatest with the [^{18}F]-FDOPA tracer, collected on the lower resolution GD Advance 3D scanner, so it is possible that a different gray matter threshold could reduce this effect.

One unexpected finding was that the BP_{ND} values for in the occipital cortex for [^{18}F]-Fallypride and [^{11}C]-NNC112 were comparable to those in the other cortical regions. We predicted that they would be lower since studies in non-human primates have shown that cortical D_1 receptor levels were highest in the prefrontal cortex and decreased further back along the rostral-caudal gradient with the lowest levels being in the occipital cortex [202]. However, D_2 receptor levels in non-human primates were shown to have the highest cortical levels in the frontal, parietal, and occipital cortices [202]. In addition, there is great variation in the pattern of dopaminergic innervation of the cortex across species [203], so it is difficult to make predictions from the animal literature. Furthermore, the [^{11}C]-NNC112 tracer has affinity for the serotonin 5-HT_{2A} receptor in addition to dopamine D_1 receptors, which is especially problematic with cortical signal that may have a 20-30% serotonergic contribution [204]. Serotonin-2 receptors are concentrated in several cortical areas including the occipital lobe [205], which may explain part of the reason why the [^{11}C]-NNC112 signal there is comparable to that in the other cortical ROIs. Furthermore, human post-mortem studies have shown that dopamine D_2 receptor densities are very low throughout most of the cortex [206], which likely explains why we are unable to pick up variance between cortical regions. With the [^{18}F]-FDOPA tracer, however, we did see the expected pattern of K_i values being highest in the prefrontal regions (DLPFC ≈ 0.9e-3, ACC ≈ 1.2e-3, OFC ≈ 1.1e-3, occipital cortex ≈ 0.6e-3).

Taken together, surface-sampling and smoothing generally improved the signal and decreased noise in the cortex for the PET data that we tested, with the

largest effects seen with the data collected on the high-resolution (HRRT) scanner. Furthermore, partial volume correction increased the mean signal even more for all three tracers. More work is needed to optimize the PVC method for data collected on the GE Advance 3D scanner (e.g. testing out different gray matter thresholds), however, the surface-based pipeline generally achieved our desired outcome of increased signal and reduced noise.

6.3 Data-Driven PET Parcellation: Application for Automated Optimal Reference Region Delineation

6.3.1 Introduction

6.3.1.1 Compartment Modeling

PET data is commonly analyzed using full compartment models that require arterial blood sampling to quantify the kinetics of tracer distribution [207]. However, for certain tracers, non-invasive models can be used that require only the time activity curve of a reference (control) region, eliminating the need for invasive arterial blood sampling [81, 82, 208]. With the reference region method, the time activity curve in a region of interest (or voxels across the brain) is compared to that of a reference region, for which the following two assumptions must be valid: (1) the reference region must have little to no specific binding of the tracer and (2) the distribution volume is the same in the tissue of interest and the reference tissue, at equilibrium. The distribution volume is the ratio of the radioligand concentration in the tissue of interest (the nonspecifically bound

tracer) to the plasma at equilibrium and gives a measure of how much the radioligand is being concentrated in the tissue. Another way to think about the distribution volume is as the volume of blood that contains the same activity as 1 ml of tissue [209]. Given these constraints, we predict that the curve of activity over time in the ideal reference region would go up as the tracer enters the tissue but would then go down quickly over time since the tracer is not specifically bound to a target.

6.3.1.2 Current Methods for Reference Region Definition

Manual definition of regions of interest including the reference region has been considered the gold standard method for reference region model PET data analyses. This involves hand-tracing the regions on either the PET data itself or an MRI scan and can be very time consuming and prone to error and bias. In addition, if the hand-tracing is done on an MRI scan, there is potential for alignment error when it is registered to the PET data. Furthermore, if the hand-tracing is done on the PET data, the limited spatial resolution of PET data may make it difficult to completely distinguish a desired gray matter reference region from the surrounding vasculature, cerebrospinal fluid, and white matter. A schematic of the arteries and veins of the brain is shown in **Error! Reference source not found.**. Careful selection of reference region voxels is important because if voxels including vasculature or white matter are included, the assumptions required for reference region validity may not be met and the modeled parameter of interest (i.e. specific binding of tracer) may be flawed.

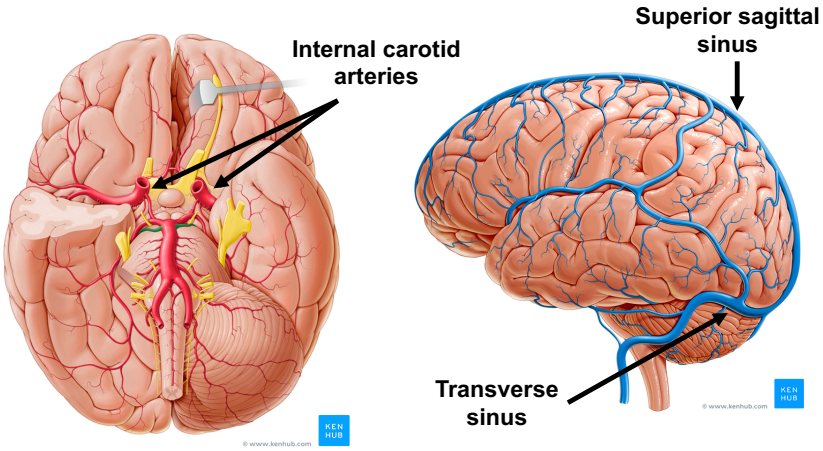


***Figure 31**: Major vasculature of the brain with select vessels labels. (internal carotid arteries, superior sagittal sinus, and transverse sinus) (adapted from [213, 214], © Kenhub (www.kenhub.com))*

Some automated methods for ROI definition have been developed using software such as FreeSurfer or other templates, however it has been found that manual definition of the cerebellar reference region was required for good agreement [210]. In addition, these methods require an MRI scan, which can introduce variance due to variation in sequence and quality, is costly, and can be difficult to obtain in patients with movement disorders such as Parkinson's disease. Other automated methods for reference region delineation that do not require an MRI scan have been published using a unsupervised PCA approach [211] and supervised clustering approach [212], however, they have not been widely adopted yet and it is unclear whether they are generalizable to different PET tracers. The method that our lab has adapted is described in Section 3.5. In short, we use FreeSurfer to automatically segment the cerebellum gray matter from a T1-weighted MRI scan followed by a hand-editing process to clean up any mistakes in the automatic process and then in house scripts to exclude the vermis and lateral and superior parasinus regions (see **Figure 32** for example

and Section 3.5 for more details). In addition to requiring a separately acquired MRI scan and accurate alignment with the PET data, this process also uses valuable time for the hand-editing process. Therefore, there is a need for a generalizable and completely automated reference region method that is based solely on the PET data.

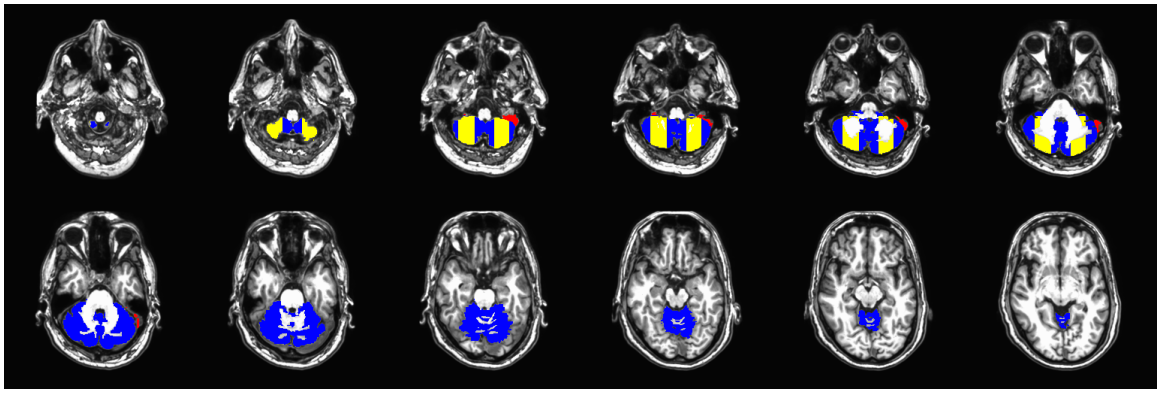


***Figure 32**: Example cerebellum reference regions for an example subject. Masks included are the FreeSurfer automated segmentation of the cerebellum gray matter (conjunction of all shown masks), non-brain voxels removed during hand-editing (shown in red), and final reference region after exclusion of medial and lateral slices (yellow).*

6.3.2 Methods

6.3.2.1 Descriptive Model

We modeled activity over time of PET data following a bolus tracer infusion with a descriptive model: $\boldsymbol{Activity = \gamma * (1 - e^{-\alpha * t}) * e^{-\beta * t}}$. This model is composed of an upper limit, γ, an exponential decay component in the increasing form $(1-e^{-\alpha * t})$ to model rate of tracer uptake, and an exponential decay component in the decreasing form $(e^{-\beta * t})$ to model rate of tracer decay. This approach allows us to extract key features from the data and reduce the dimensionality from 27 or more time points at each voxel (in the PET studies used here) to three parameters: α, β, and γ. For the [^{18}F]-Fallypride tracer that

has an almost three times longer scan time than the other two tracers, we only used the first 90 minutes of scan data to keep the validity of the descriptive model for the tracer kinetics.

6.3.2.2 Parameter Fitting and Error Weighting Function

Parameter fitting was completed in Matlab with the nonlinear solver fminsearch, which uses the Nedler-Mead optimization method [215]. This optimization method was chosen because it can be used even in cases when the function that is being optimized is not differentiable, making it versatile for multiple applications. PET images were smoothing volumetrically with a kernel of 10mm fwhm to reduce some of the noise in the data. To exclude voxels that fell outside the brain, the model-fitting was restricted to voxels with average count values larger than the mean for the entire image. Careful consideration was given to the error-weighting function for the parameter fitting since an equal weighting of the error from all frames (timepoints) would overfit the timepoints that contain less data (e.g. the early timepoints that are shorter in duration and the late timepoints where the PET tracer has decayed significantly). Total prompts (coincidences) were extracted from the dicom header for each timepoint image using the ImageJ software [216]. The detected total prompt counts in the raw data follows the Poisson distribution, so the standard deviation of the count rate is approximately equal to the square root of the total prompts [217]. For each voxel and each time point, the sum of squared error, or square of the difference between the tested model values and the actual data, was multiplied by the standard deviation term. As a result, the optimization process weighs

error that occurs during the middle time frames more heavily, when the total counts are the highest, than the beginning or end frames. An example of the error weighting vector (square root of total prompts) for one subject is shown in **Figure 33**.

The model-fitting procedure was done independently for each voxel in the brain (more than one million), which took over a week to run on a single linux machine. To accelerate this process, the Matlab code was parallelized to 500 nodes, compiled so that it would not require a Matlab license, and run on the NIH biowulf supercomputing cluster, reducing the run-time to approximately 15 minutes per scan.

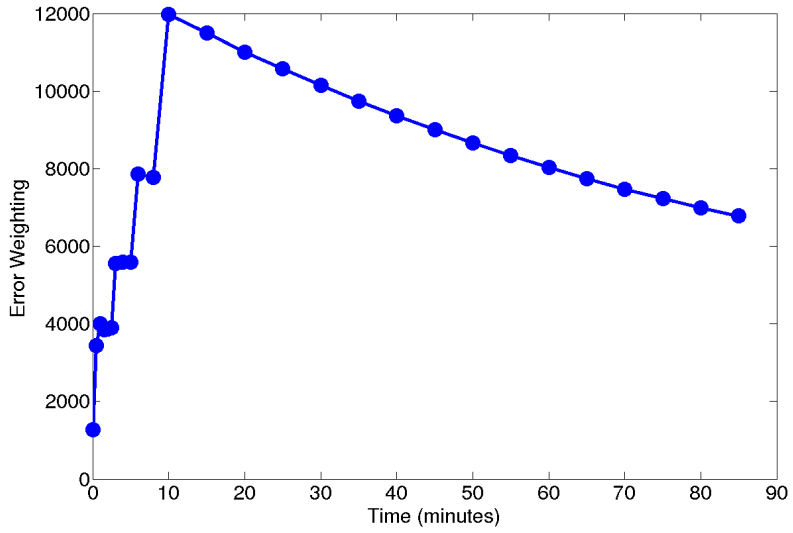


***Figure 33**: Example error weighting vector for one subject for an [^{18}F]-FDOPA scan. This is calculated as the square root of the total prompts for each time point*

.

6.3.2.3 Reference Region Voxel Selection

A priori knowledge of the kinetics of a desirable reference region was used for defining the automated voxel selection process. Specifically, an ideal point in the three-dimensional parameter space (α, β, and γ) was defined and, for each

voxel, a distance from the ideal point was calculated. In order to exclude white matter, where uptake of the tracer is limited, the ideal γ value was defined as the maximum value. To select voxels without specific uptake of the tracer, the ideal β value was defined as the maximum value, where the decay rate of the tracer over time would be the greatest. Finally, to exclude voxels containing mostly vasculature, the ideal α value was defined as the minimum.

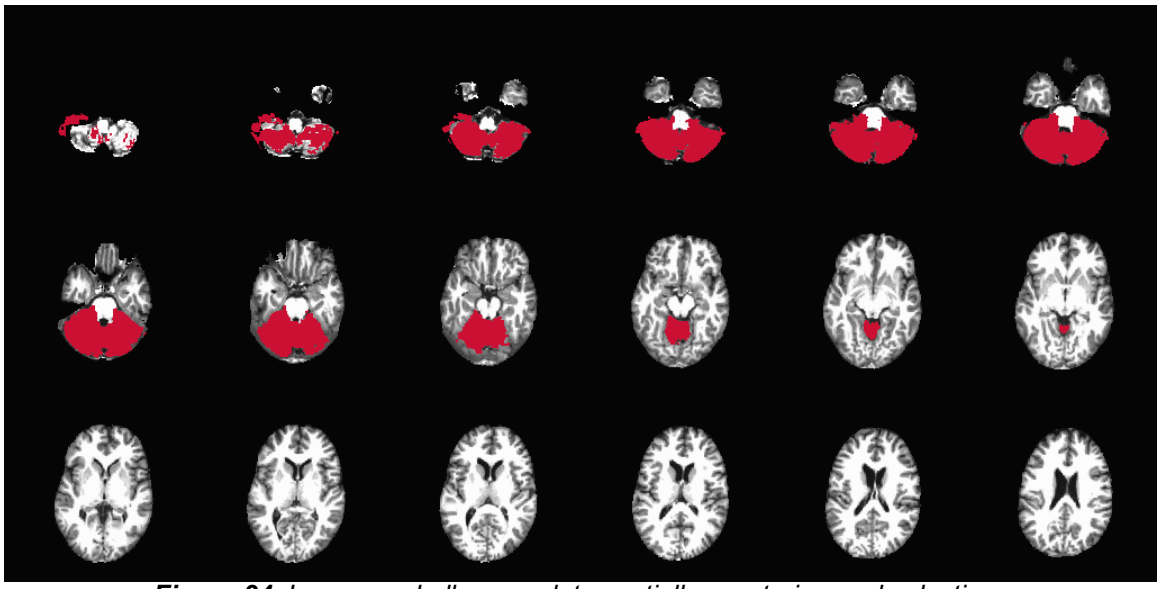


***Figure 34**: Large cerebellum mask to spatially constrain voxel selection.*

For the actual voxel selection procedure, a large cerebellum mask was first applied to spatially restrict the selected voxels because the cerebellum is the commonly accepted reference region for the three tracers tested here (see **Figure 34**). In this testing cohort, we used the native-space cerebellum segmentations from each individual's native-space MRI scan, although we could have also used a common-space cerebellum mask warped to each individuals' PET space using a PET-based MNI to native space warping procedure. Given the large size of the cerebellum mask used, we would not expect this to change the results much. The bottom three slices of the PET data were also excluded

from reference region selection due to the visible increased noise of images collected at the periphery of the scanner's field of view. Next, the parameter maps for α, β, and γ were z-normalized to transform the data to a common scale and reduce outlier effects. The ideal point was generated from the z-normalized cerebellum parameter data according to the criteria in the previous paragraph. Next a distance value was calculated for each voxel within the cerebellum as the absolute value of the difference between the parameter values for that voxel and the ideal values. The difference values were the sum of the distances from each parameter, which was equal to the absolute value of the difference between the ideal and fit parameter value for β and γ (except for when Z_β was less than -1, the error term was automatically set to 999999 to avoid inclusion of any voxels with high specific binding of the tracer). A stepwise weighting system was used for α because the ideal reference region does not necessarily have the lowest alpha (or rate of tracer uptake) values, rather, it should exclude the voxels with the highest alpha values that are characteristic of vasculature. The stepwise weighting system for α was based on the parameter value z-normalized to the whole brain (z_α) and followed these criteria: **0** if $z_\alpha < 1$, **1** if $1 > z_\alpha < 2$, **2** if $2 > z_\alpha < 3$, and **3** if $z_\alpha > 3$. A schematic of the distance metric algorithm is shown in **Figure 35**.

For the [^{18}F]-FDOPA tracer, for which 16 healthy volunteers were scanned twice, we examined the effect of reference region size by constraining the maximum number of selected voxels to the following values: 3000, 5000, 7500, 10000, 12500, and 15000. The mean number of voxels in the native-space MRI

defined cerebellar reference region is 6,610.5 (range 4,174-11,009) and the mean number of voxels in the entire cerebellum is 36,864.2 (range 27,358-46,431).

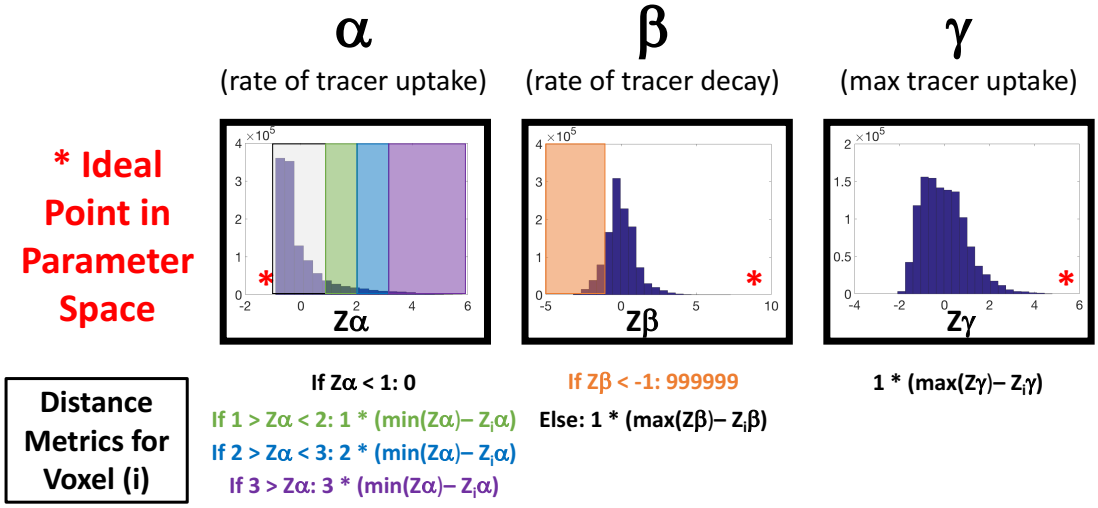


***Figure 35**: Schematic of the distance metric assignment for each of the three fitted parameters. The ideal point (red *) is defined as the minimum z-score for the α parameter, maximum z-score for the β parameter, and maximum z-score for the γ parameter. The distance from the ideal point is defined as a linear difference in z-scores from the ideal point for the β and γ parameters, except when Z_β is less than -1 it is set to 999999 to ensure exclusion of voxels with specific binding. For α, the distance is defined as zero if Z_α is less than 1, 1 times the difference between Z_α and the minimum Z_α score if Z_α is between 1 and 2, 2 times the difference between Z_α and the minimum Z_α score if Z_α is between 2 and 3, and 3 between Z_α and the minimum Z_α score if Z_α is greater than 3. The total distance metric for each voxel is the sum of the distance metric for each of the three parameters.*

6.3.2.4 Test-Retest Reliability

One way to validate our automated reference region selection method is to measure the test-retest reliability of the PET parameters of interest. We collected longitudinal [^{18}F]-FDOPA data from two cohorts of subjects who were scanned twice. Cohort 1 consisted of 17 healthy participants (mean age 55.6, range 42.9-71.6, five females) who were scanned an average of 5.6 years apart (range 2.1-10.6) and who had good quality MRI scans that consisted of averages of multiple T1 images (**Figure 36a**). Cohort 2 consisted of data collected from a

collaborator on a group of individuals who have Gaucher disease or are carriers of a mutation conferring genetic risk for Gaucher disease, which is a lysosomal storage disease that increases risk for Parkinson's disease. None of these patients had signs of Parkinson's disease and were thus expected to have stable [^{18}F]-FDOPA data over time. Cohort 2 included 26 participants (mean age 57.3, range 27.5-78.5, 9 females) who were scanned an average of 3.4 years apart (range 1.1-8.1). Importantly, this cohort had poor quality MRI scans that were single T1 images (**Figure 36b**).

For both cohorts, we calculated three different test-retest reliability measures for the specific uptake rate (K_i) in the putamen: absolute percent difference (APD), intraclass correlation coefficient (ICC), and standard error of measurement (SEM). The APD was calculated as the absolute value of the difference between the bilateral putamen K_i from the first and second scans, divided by the mean of both: $\mathbf{A}PD = \frac{|Putamen_Ki_visit1 - Putamen_Ki_visit2|}{mean(Putamen_Ki_visit1, Putamen_Ki_visit2)}$.

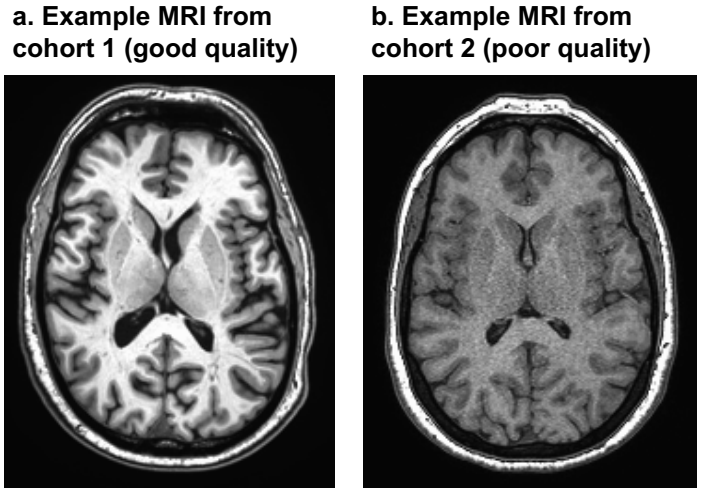


Figure 36*: Example T1 MRI images for (a) cohort 1 (good quality) and (b) cohort 2 (poor quality)*

The ICC is an index of reliability that takes a value between 0 (no agreement between measurements) and 1 (absolute agreement) and represents the within-subject variance in the data compared to the between-subject variability [218-220]. Intraclass correlation values, r, greater than 0.6 are good and those greater than 0.75 are considered excellent [221]. To calculate the ICC, a one-way model with row effects random was used according to the equation: $\boldsymbol{r} = \frac{\boldsymbol{MS_R - MS_W}}{\boldsymbol{MS_R}}$, where MS_R is the mean square error (or variance) for rows (i.e. between subject variance in putamen K_i values) and MS_W is the mean square error for residual sources of variance (i.e. sum of within subjects variance in putamen K_i values) [220]. Finally, while the ICC provides a unitless value of reliability of a measurement, the SEM provides an estimate of the precision of a measurement. The SEM is the product of the standard deviation of a measurement (within subject standard deviation), s, and the square root of one minus the intraclass correlation coefficient, r: $\boldsymbol{SEM = s * \sqrt{1 - r}}$.

6.3.3 Results

Ten healthy individuals who completed all three PET scans ([^{18}F]-FDOPA, [^{11}C]-NNC112, and [^{18}F]-Fallypride) were selected as a test cohort for the proof of concept of this method. In addition, this method was also applied to the data of 17 healthy controls and 26 Gaucher disease patients and family members who completed the [^{18}F]-FDOPA PET scan twice and measures of test-retest reproducibility were calculated. The results of the parameter fitting for all three tracers for a representative example subject are shown in Section 6.3.3.1. In

addition, parameter values for specific voxels are shown to demonstrate the differences in kinetics between vasculature, white matter, gray matter with specific uptake of the tracer, and gray matter with non-specific uptake. Lastly, the final selected voxels for the reference region are presented for the cases when there is no spatial constraint (can select voxels from the whole brain) and when the voxel selection is limited to the cerebellum.

6.3.3.1 Parameter Fitting

Whole brain parameter maps for all three of the PET tracers demonstrate spatial correspondence of the tissues that we sought to segregate. Specifically, the map of α values ([^{18}F]-FDOPA: **Figure 37**, [^{11}C]-NNC112: **Figure 38**, [^{18}F]-Fallypride: **Figure 39**) shows the highest values in regions consistent with major arteries and veins in the brain such as the internal carotid arteries and the superior sagittal and transverse sinuses (depicted in **Error! Reference source not found.**).

The maps of β values show the lowest values, or slowest decay, in regions known to have high specific uptake (putamen and caudate nucleus) and the highest values in regions with quick decay indicating low specific uptake (cerebellum, occipital lobe, and vasculature) ([^{18}F]-FDOPA: **Figure 40**, [^{11}C]-NNC112: **Figure 41**, [^{18}F]-Fallypride: **Figure 42**). Lastly, the whole brain maps of γ values show high values in the gray matter and low values in the white matter, indicating that more of the tracer gets into gray matter compared to the white matter ([^{18}F]-FDOPA: **Figure 43**, [^{11}C]-NNC112: **Figure 44**, [^{18}F]-Fallypride: **Figure 45**).

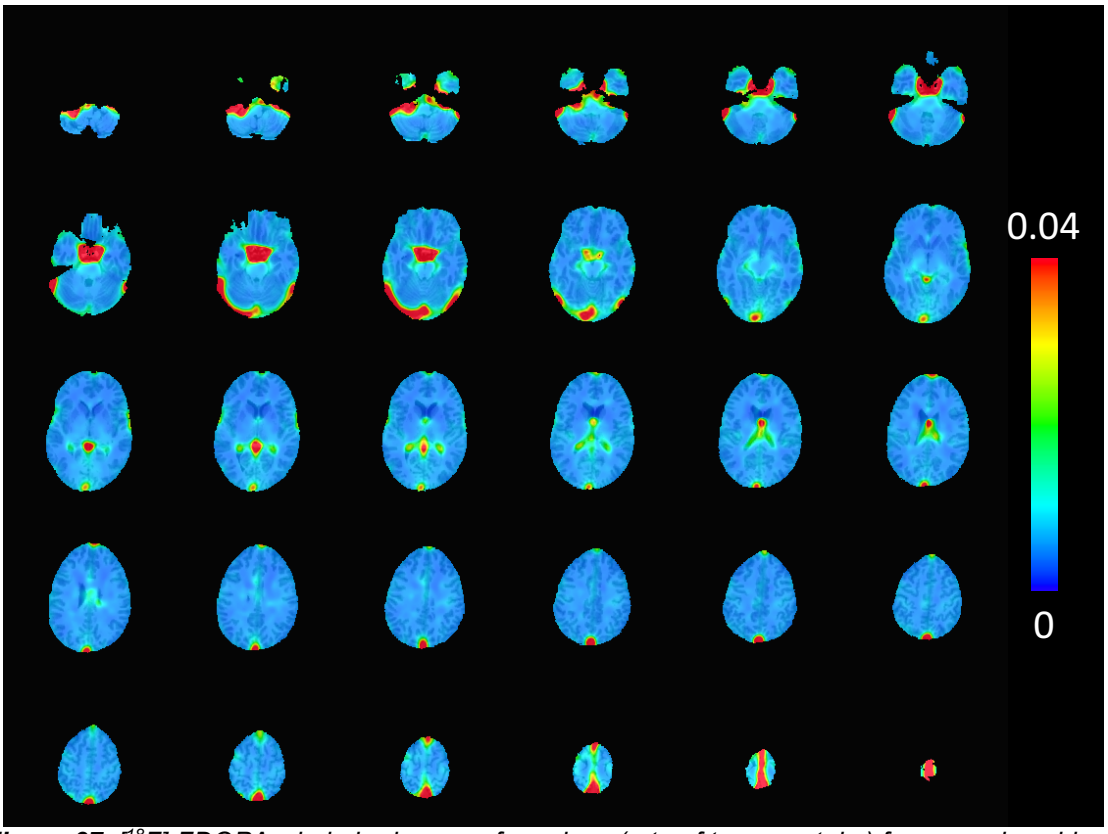


***Figure 37**: [^{18}F]-FDOPA whole brain map of α values (rate of tracer uptake) for example subject.*

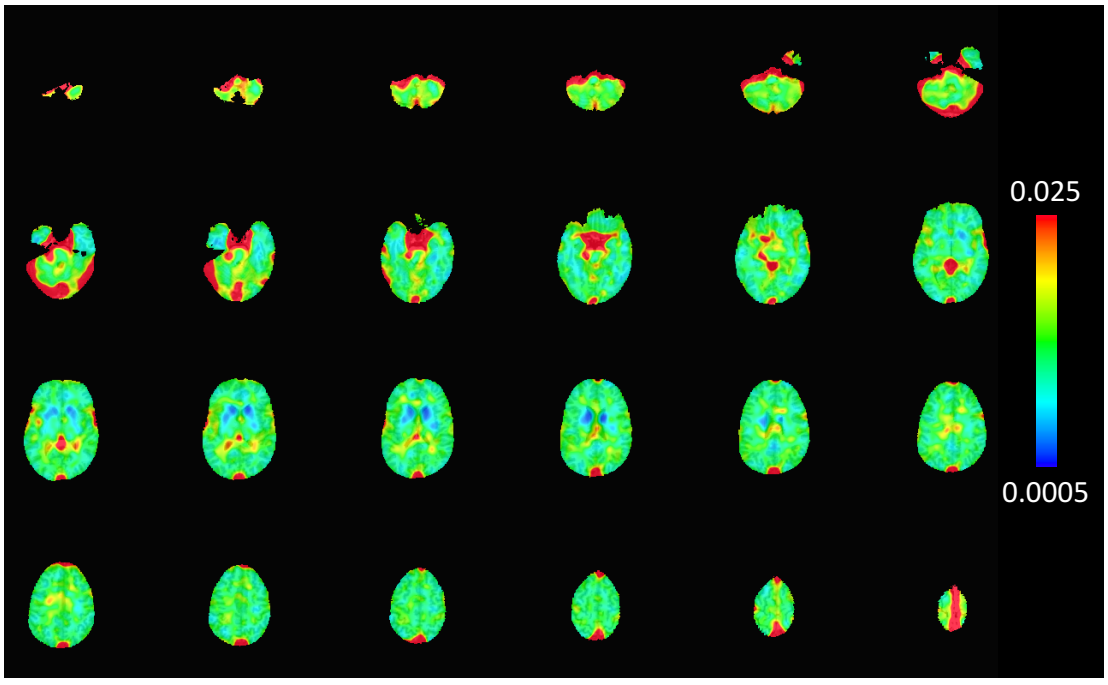


***Figure 38**: [^{11}C]-NNC112 whole brain map of α values (rate of tracer uptake) for example subject.*

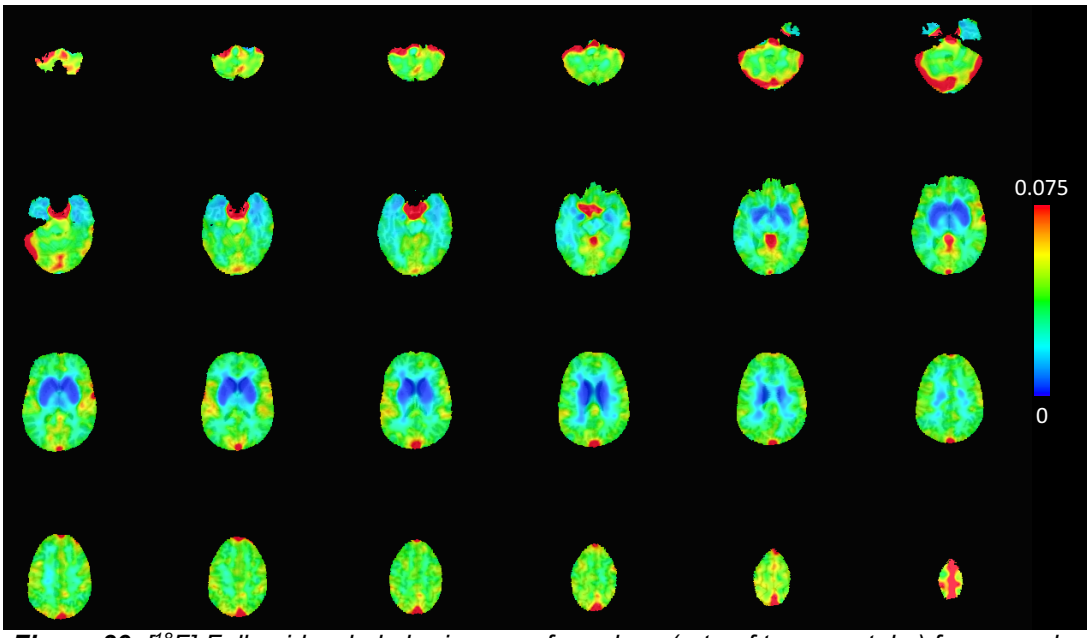


***Figure 39**: [^{18}F]-Fallypride whole brain map of α values (rate of tracer uptake) for example subject.*

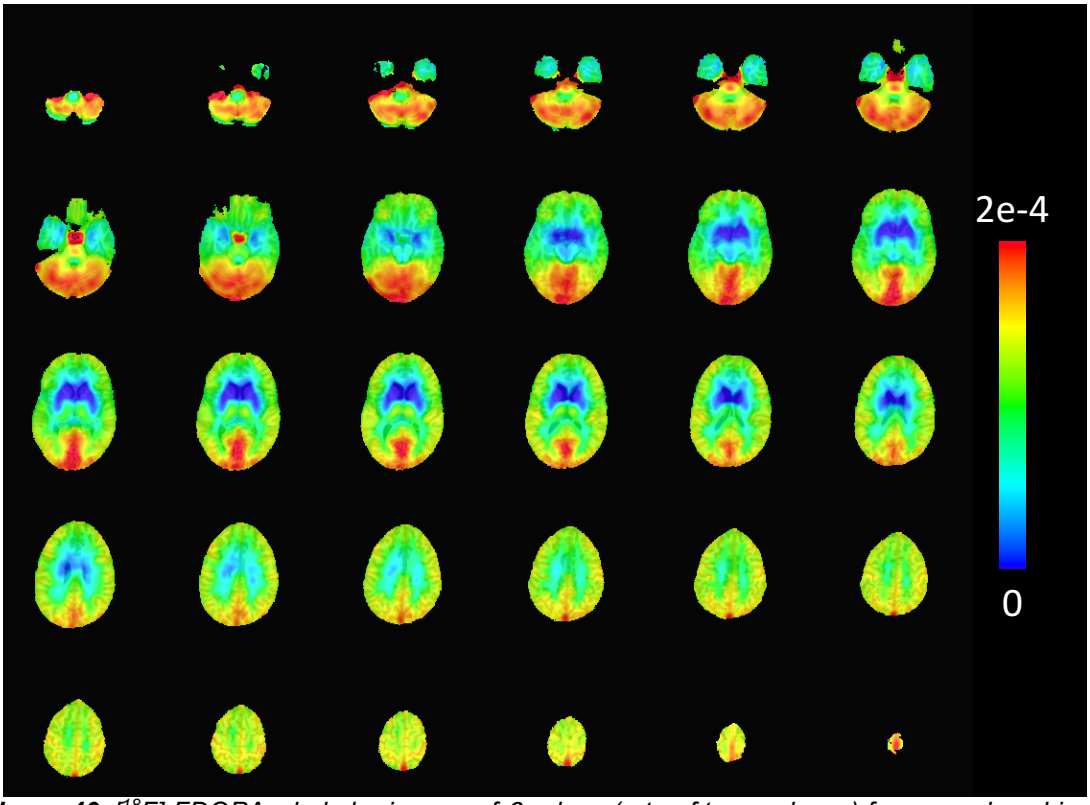


***Figure 40**: [^{18}F]-FDOPA whole brain map of β values (rate of tracer decay) for example subject.*

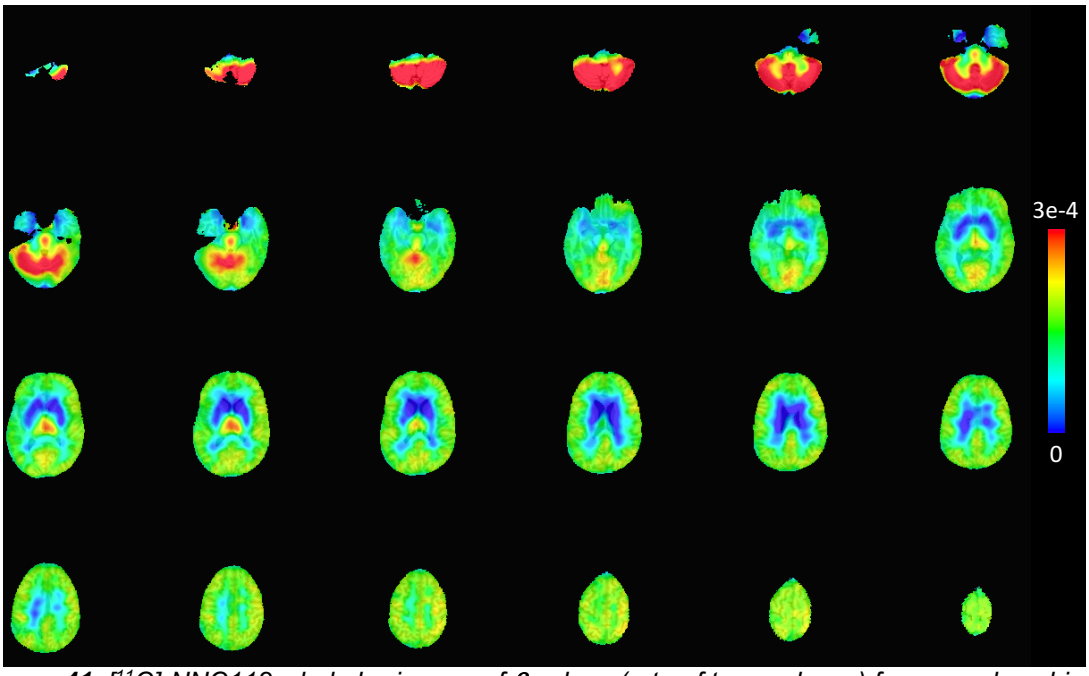


***Figure 41**: [^{11}C]-NNC112 whole brain map of β values (rate of tracer decay) for example subject.*

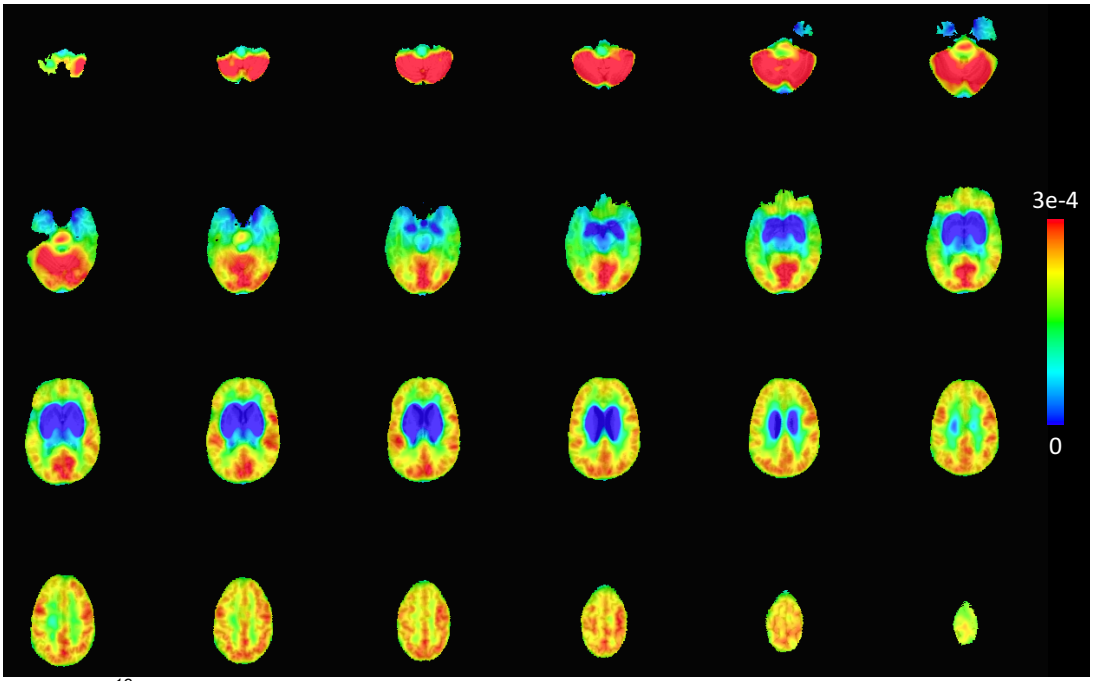


***Figure 42**: [^{18}F]-Fallypride whole brain map of β values (rate of tracer decay) for example subject.*

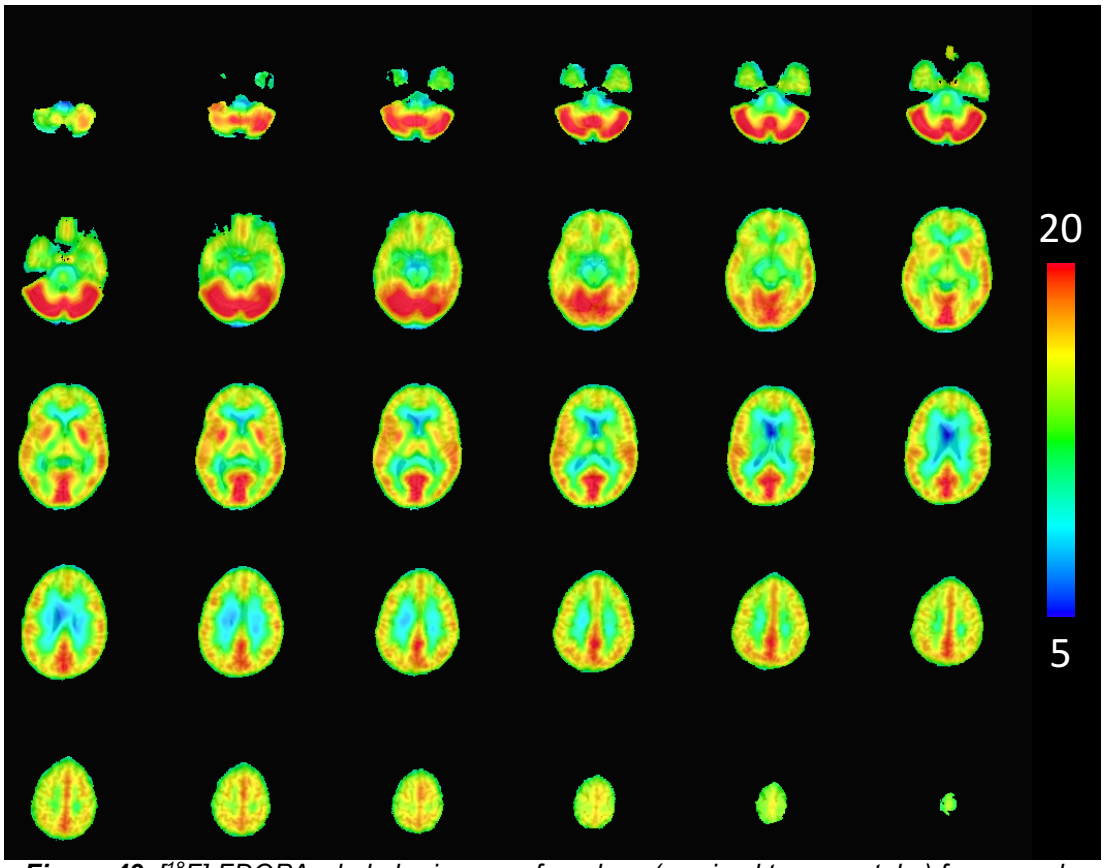


***Figure 43**: [^{18}F]-FDOPA whole brain map of γ values (maximal tracer uptake) for example subject.*

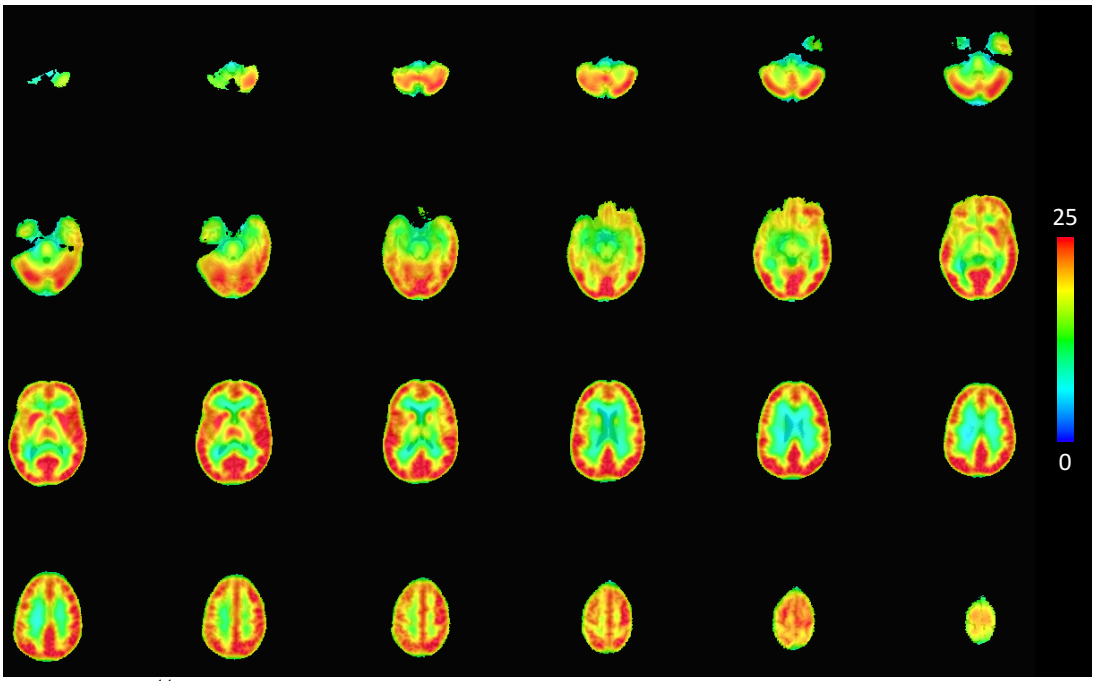


***Figure 44**: [^{11}C]-NNC112 whole brain map of γ values (maximal tracer uptake) for example subject.*

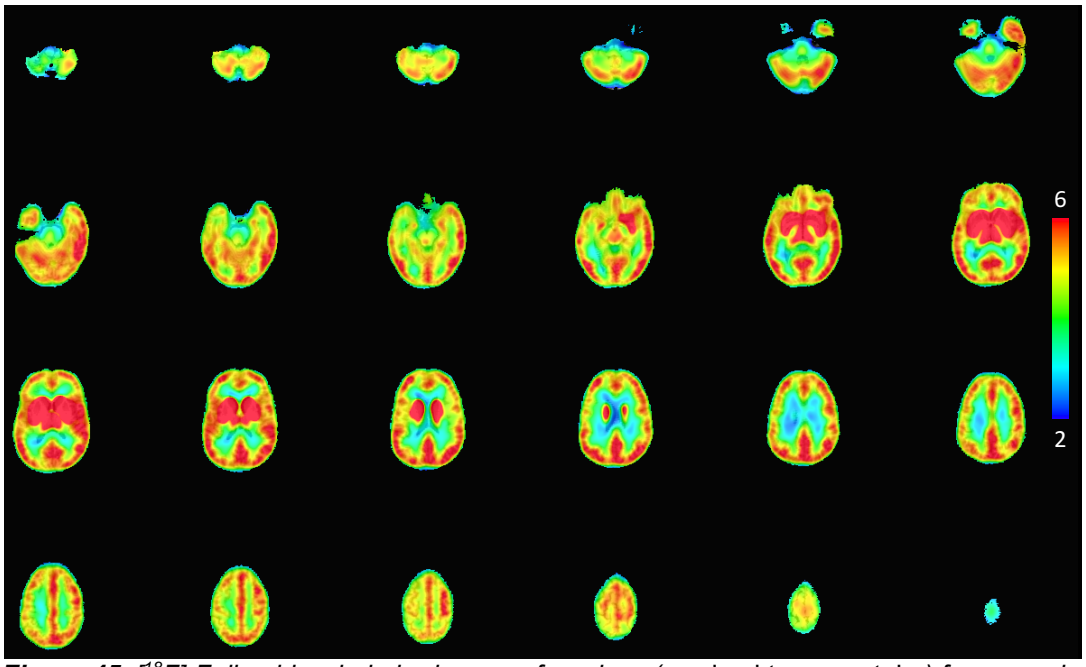
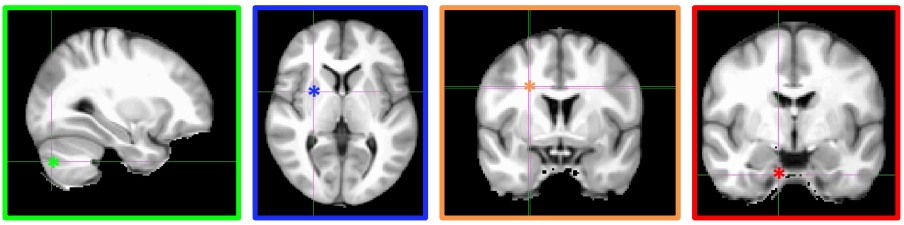


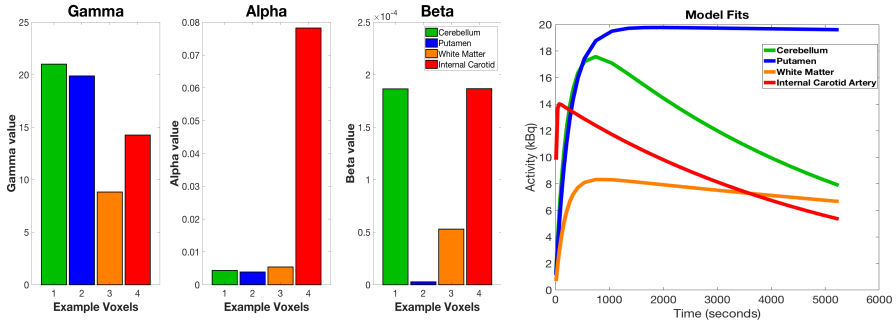
***Figure 45**: [^{18}F]-Fallypride whole brain map of γ values (*maximal tracer uptake*) for example subject.*

Finally, to demonstrate the ability of this method to characterize vasculature, white matter, gray matter with specific uptake, and gray matter with non-specific uptake, parameter values and plots of model-fits from example voxels of these tissue types are shown in **Figure 46**. The vasculature (internal carotid artery) is characterized as having a high alpha value, or quick rate of tracer uptake. The white matter has relatively low gamma (total tracer uptake), alpha (rate of tracer uptake), and beta (rate of tracer decay). The gray matter with specific uptake (putamen) has high gamma with low alpha and low beta, indicating a slow decay due to specific binding of the tracer to the target. Lastly, the gray matter with non-specific uptake (cerebellum) has a high gamma with low alpha and high beta, due to a quick washout of the tracer because of minimal specific binding of the tracer.

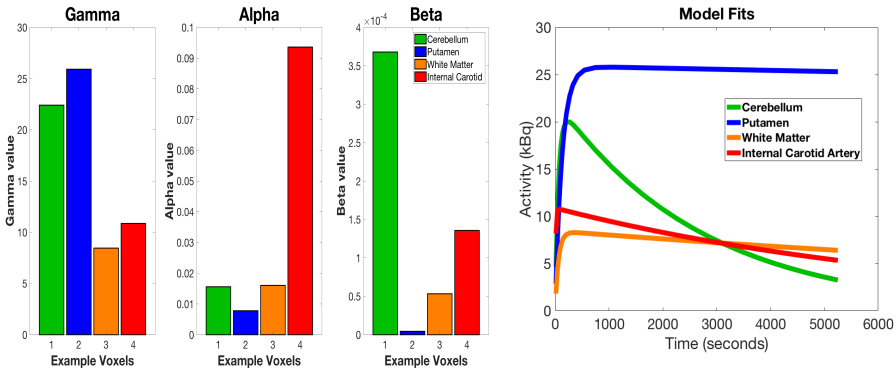
a. Location of example voxels



b. [^{18}F]-FDOPA parameter values for example voxels



c. [^{11}C]-NNC112 parameter values for example voxels



d. [^{18}F]-Fallypride parameter values for example voxels

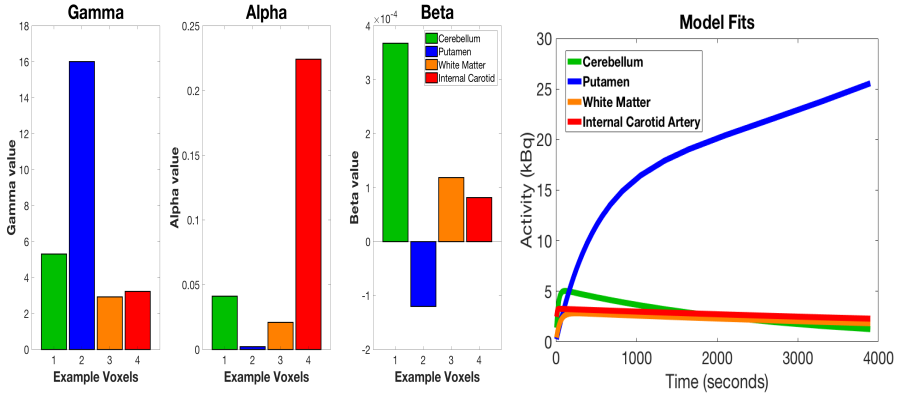


***Figure 46**: Model-fitting results from example voxels for one subject (all three PET tracers: a. location of example voxels, b. [^{18}F]-FDOPA, c. [^{11}C]-NNC112, d. [^{18}F]-Fallypride). Additional images with actual data and model fits are in Chapter 6 Appendix B.*

6.3.3.2 Reference Region Selection

Using the automated algorithm for selecting voxels for the reference region described in Section 6.3.2.3, reference regions of various sizes ranging from 3,000 to 15,000 voxels were created. Histograms of the parameter values for all voxels in the brain as well as those selected for the largest size reference region (15,000 voxels, no spatial mask used) are shown in **Figure 47** ([^{18}F]-FDOPA), **Figure 48** ([^{11}C]-NNC112), and **Figure 49** ([^{18}F]-Fallypride). The results of reference region voxel selection for the whole brain are shown in **Figure 50** ([^{18}F]-FDOPA), **Figure 52** ([^{11}C]-NNC112), and **Figure 54** ([^{18}F]-Fallypride), and the results constrained to the cerebellum are shown in **Figure 51** ([^{18}F]-FDOPA), **Figure 53** ([^{11}C]-NNC112), and **Figure 55** ([^{18}F]-Fallypride).

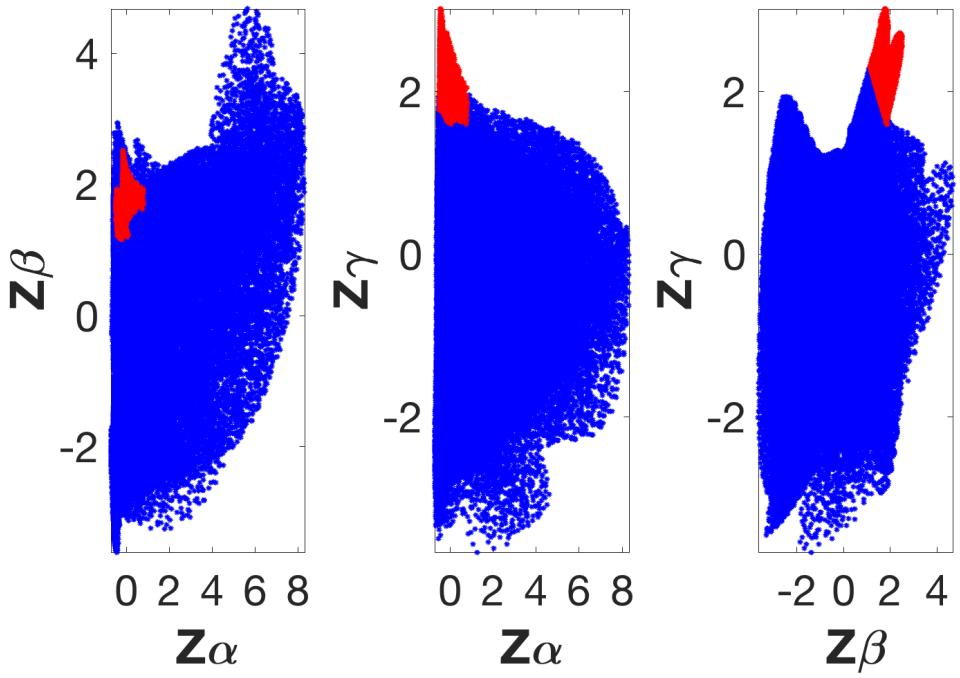


***Figure 47**: [^{18}F]-FDOPA histogram of parameter values for an example subject. All voxels in the brain are included in the histogram. Voxels selected using the automated algorithm for the largest region (15,000 voxels) are shown in red. No spatial mask was used.*

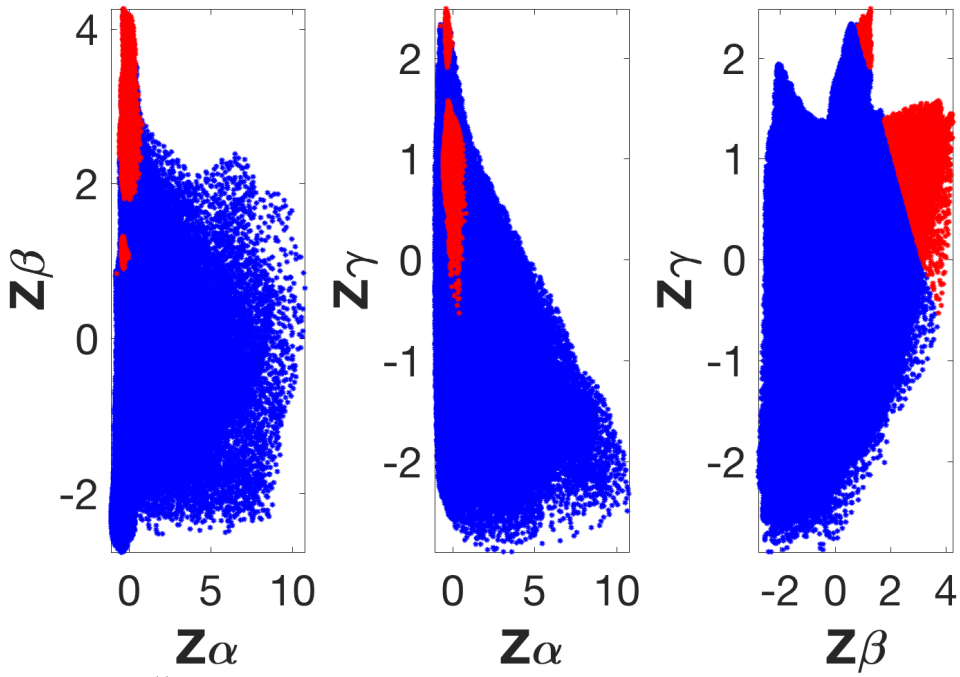


***Figure 48**: [^{11}C]-NNC112 histogram of parameter values for an example subject. All voxels in the brain are included in the histogram. Voxels selected using the automated algorithm for the largest region (15,000 voxels) are shown in red. No spatial mask was used.*

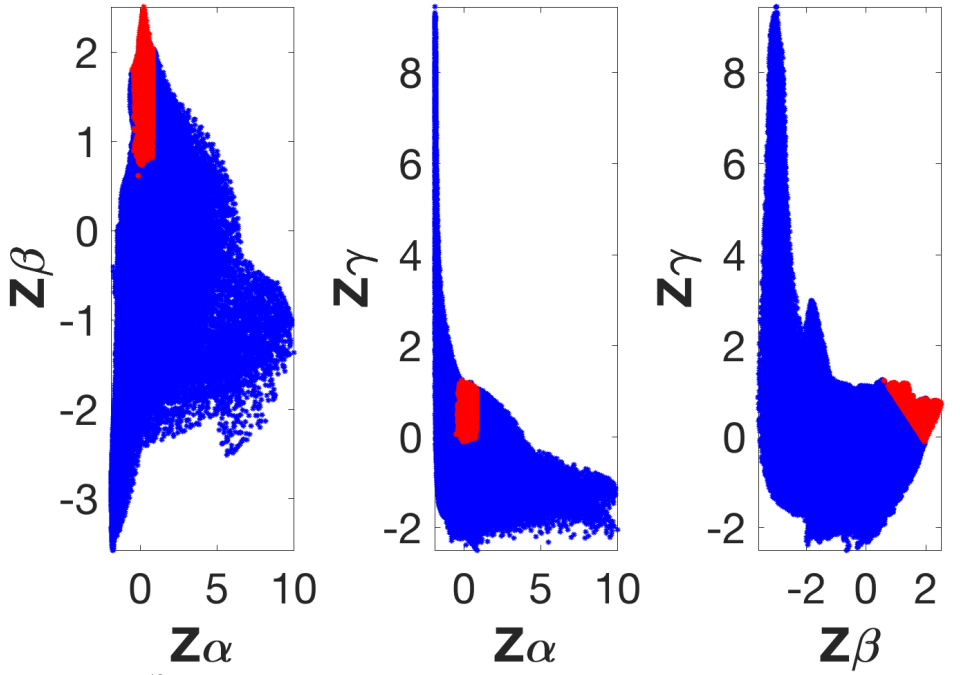


***Figure 49**: [^{18}F]-Fallypride histogram of parameter values for an example subject. All voxels in the brain are included in the histogram. Voxels selected using the automated algorithm for the largest region (15,000 voxels) are shown in red. No spatial mask was used.*

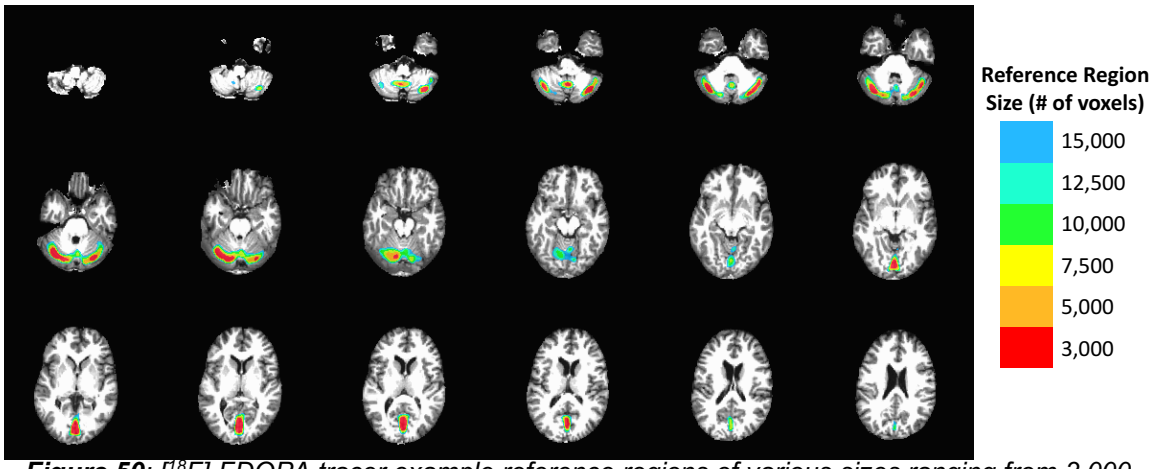


***Figure 50**: [^{18}F]-FDOPA tracer example reference regions of various sizes ranging from 3,000 (red) to 15,000 (blue) for example subject, unconstrained (whole-brain).*

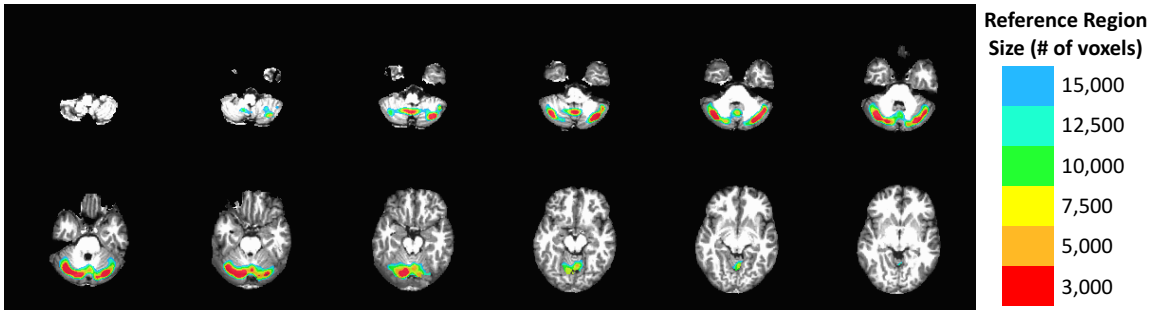


***Figure 51**: [^{18}F]-FDOPA tracer example reference regions of various sizes ranging from 3,000 (red) to 15,000 (blue) for example subject, constrained to the cerebellum with a spatial mask.*

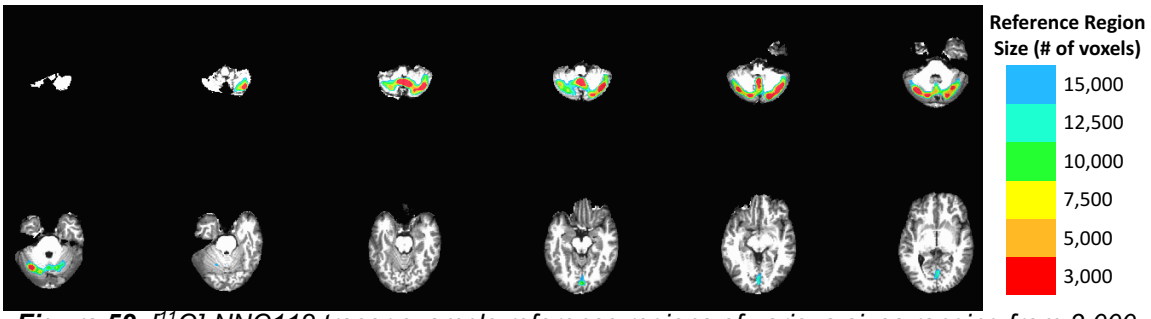


***Figure 52**: [^{11}C]-NNC112 tracer example reference regions of various sizes ranging from 3,000 (red) to 15,000 (blue) for example subject, unconstrained (whole-brain).*

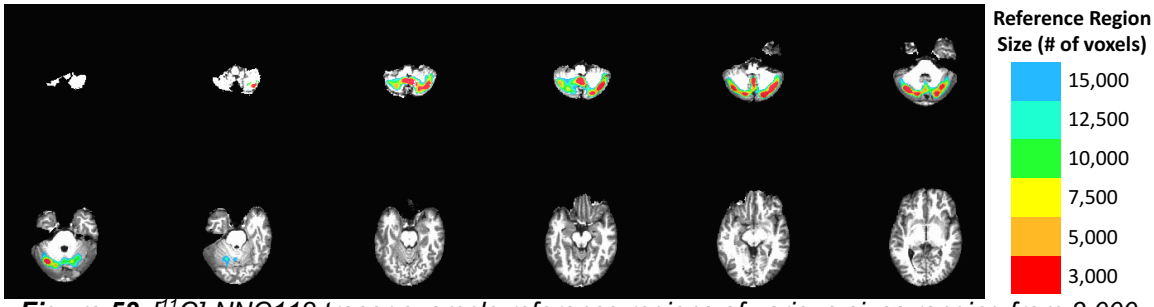


***Figure 53**: [^{11}C]-NNC112 tracer example reference regions of various sizes ranging from 3,000 (red) to 15,000 (blue) for example subject, constrained to the cerebellum with a spatial mask.*

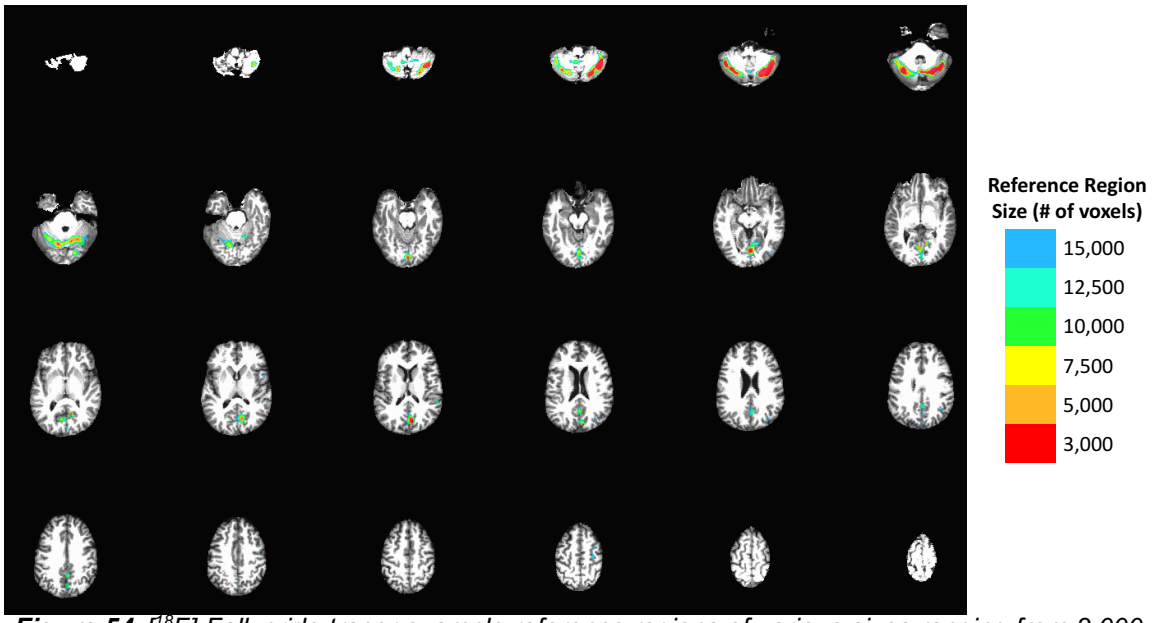


***Figure 54**: [^{18}F]-Fallypride tracer example reference regions of various sizes ranging from 3,000 (red) to 15,000 (blue) for example subject, unconstrained (whole-brain).*

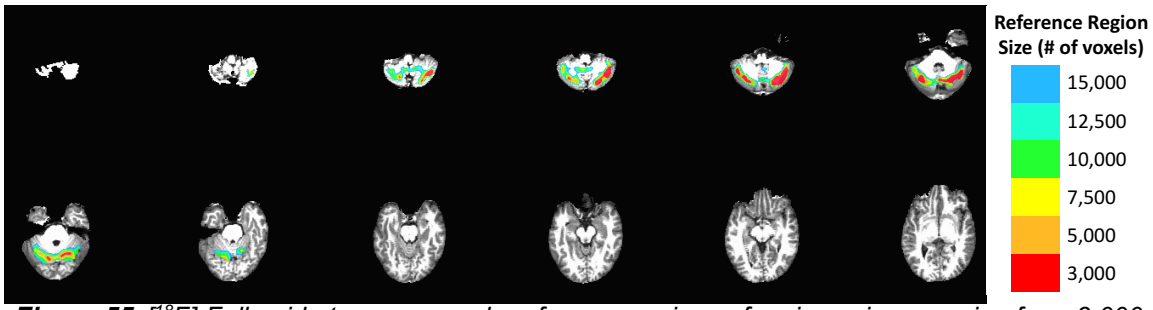


***Figure 55**: [^{18}F]-Fallypride tracer example reference regions of various sizes ranging from 3,000 (red) to 15,000 (blue) for example subject, constrained to the cerebellum with a spatial mask.*

6.3.3.3 Test-Retest Reliability of [^{18}F]-FDOPA Putamen K_i Values

All of the test-retest reliability results reported here are using reference region that is constrained to the cerebellum using a native-space mask extracted from the FreeSurfer segmentation of each subject's MRI scan, with the bottom three slices of the image removed due to noise concerns at the periphery of the PET scanner's field of view (see Section 6.3.2.3 for more details).

6.3.3.3.1 Cohort 1 – Good Quality MRI Scans

For cohort 1, with good quality MRI scans, the ICC value for the native space T1 MRI FreeSurfer segmented, hand-edited cerebellum reference region

was 0.800. All sizes of automated reference regions yielded higher values with the 5,000-voxel region having the highest value (3000: 0.808, 5000: 0.832, 7500: 0.828, 10000: 0.822, 12500: 0.821, and 15000: 0.819; see **Figure 56**). The absolute percent difference (APD) value for the native MRI hand-edited reference region was 6.453. With the exception of the smallest automated reference region

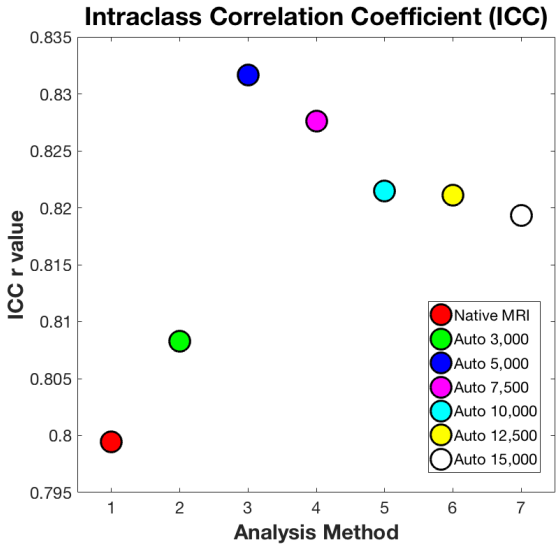


***Figure 56**: Individuals with good quality MRI scans: intraclass correlation coefficient (ICC) values for [^{18}F]-FDOPA putamen K_i values for all methods tested.*
Native MRI = FreeSurfer segmentation with hand-editing, Auto = automated data-driven method introduced here.

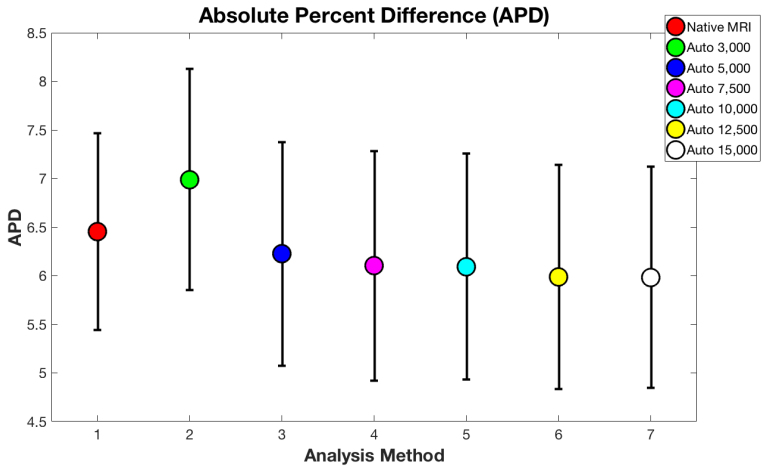


***Figure 57**: Individuals with good quality MRI scans: Absolute percent difference (APD) mean values and standard error for [^{18}F]-FDOPA putamen K_i values for all methods tested.*
Native MRI = FreeSurfer segmentation with hand-editing, Auto = automated data-driven method introduced here. None of the the automated regions were significantly different from the native MRI method (all p>0.44).

(3,000 voxels, APD 7.000), all automated methods yielded lower APD values, with the 15,000 voxel one as the minimum (5000: 6.225, 7500: 6.102, 10000: 6.093, 12500: 5.9868, and 15000: 5.983; see **Figure 57**), however none of the automated regions were significantly different from the native MRI method as assessed with a paired t-test (all p>0.44). Note that the APD is the only of these test-retest measures that yields a value for each subject and is therefore the only one where the significance of the differences can be measured with a t-test.

Lastly, the native-space MRI hand-edited method yielded a standard error of measurement (SEM) value of 2.227e-4, which was worse than all but the smallest (3,000 voxels) of the automated reference regions. Of the automated reference region sizes, the 5,000 voxel one had the lowest SEM, but all of them that were at least 5,000 voxels gave better SEM values than the native MRI method (3000: 2.309e-4, 5000: 2.008e04, 7500: 2.031e-4, 10000: 2.065e-4, 12500: 2.047e-4, 15000: 2.053e-4; see **Figure 58**).

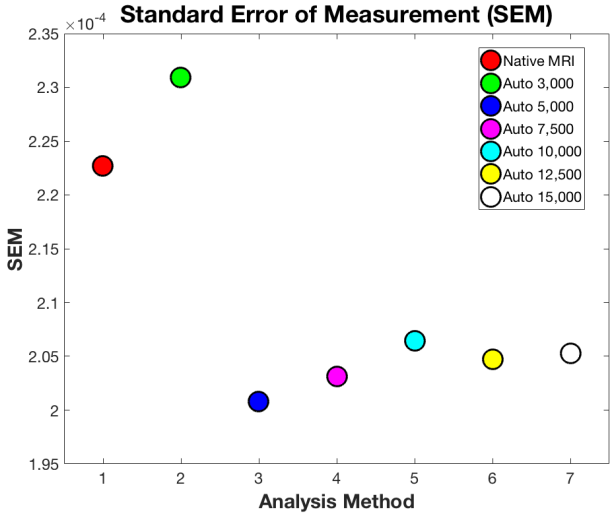


***Figure 58**: Individuals with good quality MRI scans: Standard error of measurement (SEM) for [^{18}F]-FDOPA putamen K_i values for all methods tested.*
Native MRI = FreeSurfer segmentation with hand-editing, Auto = automated data-driven method introduced here.

6.3.3.3.1 Cohort 2 – Poor Quality MRI Scans

For cohort 2 with poor quality MRI scans, we only tested the 15,000-voxel automated reference region against the standard native-space MRI hand-edited method. The ICC correlation coefficient (r) for the native-space MRI hand-edited method was only 0.351, while the automated method yielded a higher value of 0.573. The SEM for the native-space MRI hand-edited method was 7.150e-4 compared to lower error value of 4.300e-4 for the automated method. Lastly, the APD for the native-space MRI hand-edited method was 11.554, which was significantly higher than that for the automated method, which was 7.529 (paired t-test: p=0.020, t=2.474).

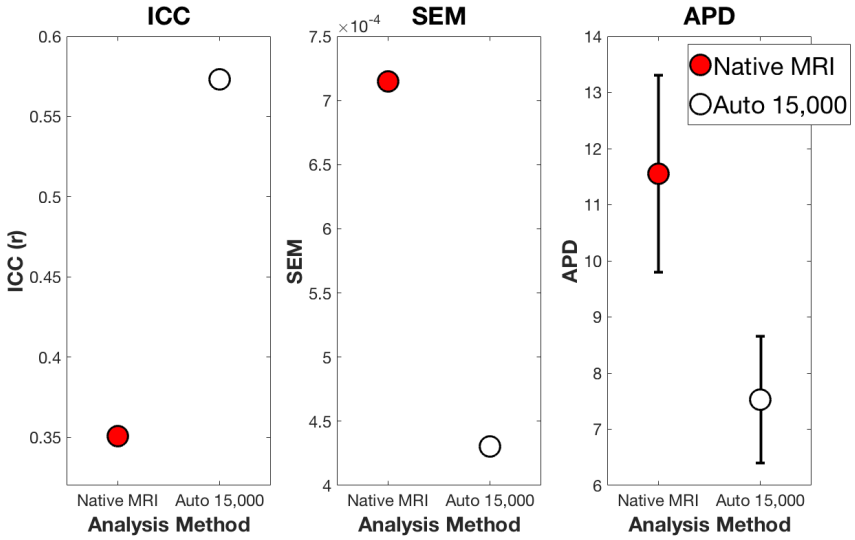


***Figure 59**: Test-retest metrics for individuals with poor quality MRI scans. Included are the intraclass correlation coefficient (ICC), standard error of measurement (SEM), and absolute percent difference (APD) for [^{18}F]-FDOPA putamen K_i values for the standard native MRI method (FreeSurfer segmentation with hand-editing) and the automated data-driven method with 15,000 voxels.*

6.3.4 Discussion

In this section, we've presented a method for data-driven parcellation and automated reference region selection for PET data from three different tracers.

Parcellation and voxel selection is based on the kinetics of the PET data alone, therefore eliminating the need for an MRI scan. This method has the ability to segregate different tissue types (vasculature, white matter, gray matter with specific binding, and gray matter with non-specific binding) and select voxels for a reference region with a reasonable spatial pattern based on apriori knowledge of dopaminergic innervation of the brain. Even when no spatial constraints are defined, a majority of the voxels selected for the reference region fall within the cerebellum, which is the region commonly used as a reference region for dopaminergic PET studies due to the low amounts of dopaminergic terminals and receptors there [174, 179, 222, 223]. Importantly, the selected voxels that fell outside of the cerebellum were mainly concentrated in the occipital lobe, another region that is commonly used as a reference region because of its low dopaminergic tone [174, 224-226].

Another striking feature of the selected reference region is that it clearly avoids voxels near the vasculature surrounding the cerebellum (e.g. transverse sinuses) as well as the white matter of the cerebellum. This is important because for a reference region model to be valid, it must have a similar flow of blood in and out of the tissue as the regions of interest, which would be the gray matter of the striatum and prefrontal cortex in this case.

In addition to the excellent spatial specificity, this method also yields test-retest reliability values that are equally good or better than the current gold-standard reference region methods. Even in healthy controls scanned over 5 years apart, we attained ICC correlation coefficients of bilateral putamen K_i

ranging from 0.808-0.832, which is in the same range as was previously found in a smaller cohort tested two years apart [227]. Furthermore, when the MRI scan is of poor quality, the gold-standard method of MRI segmentation with Freesurfer followed by hand-editing performs very poorly (ICC r = 0.351). Our automated method improves that value to r = 0.573, which is much closer to the "good" range of 0.6-0.75 [221]. While the automated method outperforms the MRI-based segmentation, the ICC value for cohort 2 with poor quality MRI scans is still much lower than the value for healthy volunteers. It is important to remember that cohort 2 included patients (and their family members) with Gaucher disease, a lysosomal storage disease that we know confers increased risk for Parkinson's disease [228]. Although the underlying mechanisms of how lysosomes contribute to neurodegenerative disorders such as Parkinson's disease are still not well understood, the link is clear and it seems unlikely that these patients have not endured any neuronal changes due to their disorder or genetic risk factors that could lead to decreased test-retest reliability. Specifically, these patients could be experiencing pre-clinical changes in their dopamine system that have not yet resulted in clinical symptoms or group differences that can be picked up with the typical neuroimaging statistical testing that we have done. This would not be surprising as we know that the motor signs of Parkinson's disease do not manifest until between 50% and 70% of dopamine neurons in the substantia nigra are lost [229].

Here, we've presented one use for the results of data-driven parcellation of PET data using a descriptive model of exponential uptake and decay.

However, there are other potential applications that should be considered as well. First of all, this method could be used to filter out voxels containing mostly vasculature which could be used for an image-derived arterial input function. Image-derived arterial input functions are an alternative to reference-region modeling in which the time activity curve from an artery is used in place of arterial sampling. This provides a non-invasive modeling approach for tracers for which a valid reference region has not been identified. Delineation of an image-derived arterial input function has many challenges including poor MRI-based segmentation of the internal carotid arteries and errors in coregistration algorithms to align the PET and MRI data [230]. Our method does not require an MRI scan or any coregistration, therefore, it provides a promising alternative to the currently available methods.

In addition to segmentation of an image-derived arterial input function, this method could also be used to define regions of specific uptake and white matter that could be used to create masks for data extraction. Finally, a third potential application for this method is to fit other types of models to voxelwise imaging data. For example, the same pipeline could be used to fit linear, quadratic, or cubic functions to longitudinal MRI data to define trajectories through development. Since the model-fitting is done independently for each voxel in the brain, this method could help identify different longitudinal trajectories for each region in the brain.

In conclusion, we've developed a tool for automated data-driven parcellation of PET data and optimization of reference region selection. This

method has the potential to substantially reduce costs and human labor associated with collecting a separate MRI scan and hand-editing the segmentations. Eliminating the MRI in PET data analysis pipeline also reduces potential bias associated with different quality MRI scans, coregistration error aligning MRI-based segmentations to the PET data, and scanning time for the patient, which is especially important for those with movement disorders such as Parkinson's disease where laying still is very difficult.

Chapter 6 Appendix

A. Surface Smoothing and Partial Volume Correction Additional Results

The results from surface smoothing and PVC for the DLPFC are shown in the main text of this chapter (**Figure 30**). This appendix contains the results from the remaining cortical regions of interest including the anterior cingulate cortex (ACC, **Figure 60**), orbitofrontal cortex (OFC, **Figure 61**), and occipital cortex (**Figure 62**). These results show that these regions all generally follow the same pattern with the main difference being the PET scanner used to collect the data (GE Advance Scanner vs. Siemens HRRT Scanner).

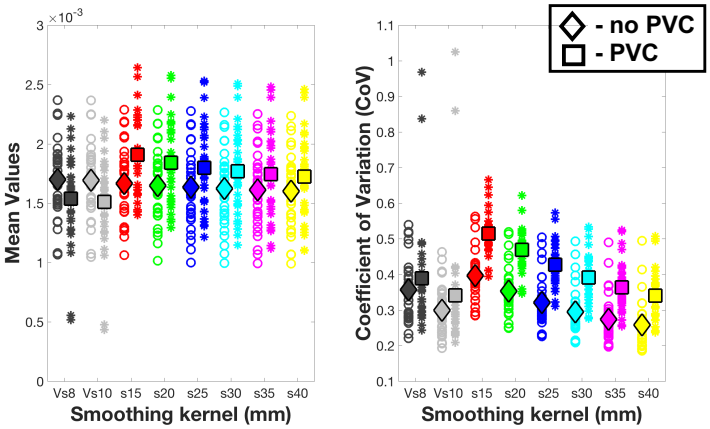
B. Example Voxel Model-Fitting Additional Results

To demonstrate how well the descriptive model in Section 6.3.2.1 fit the actual PET data, **Figure 63** shows the actual data (after 10mm smoothing) for four example voxels (cerebellum, putamen, white matter, and internal carotid artery) for a single subject. The actual parameter values from the model-fitting can be seen in **Figure 46**.

ACC Results

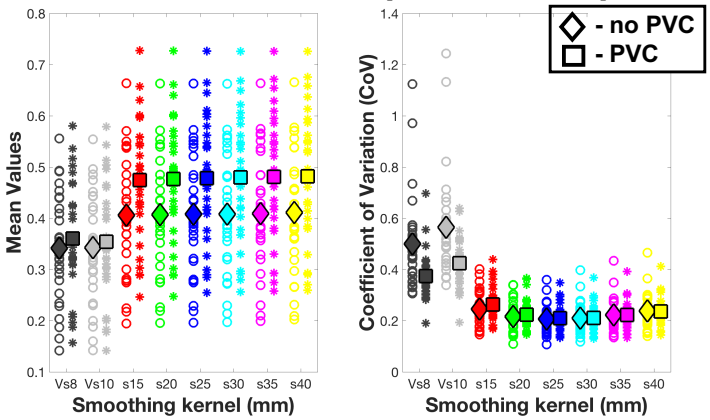
GE Advance Scanner (PSF 7mm)

[^{18}F]-FDOPA



Siemens HRRT Scanner (PSF 3mm)

[^{18}F]-Fallypride



[^{11}C]-NNC112

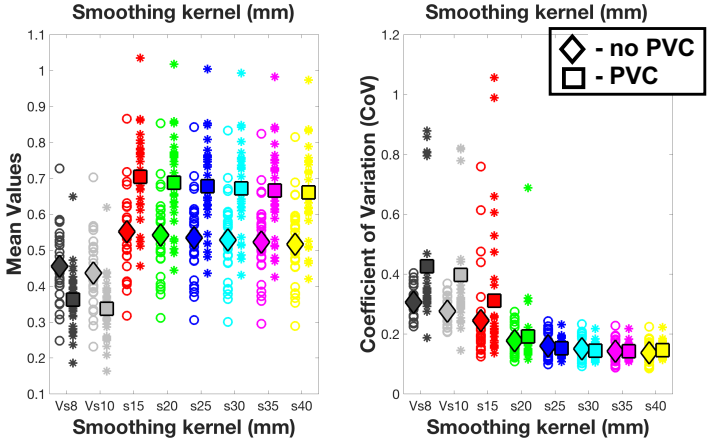
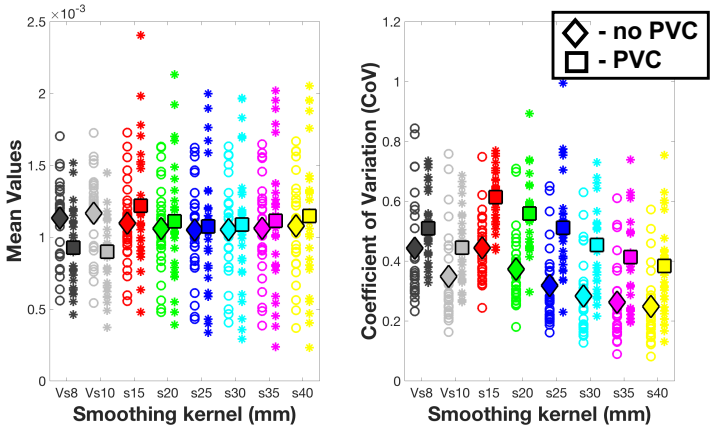


Figure 60. *Effects of surface smoothing and PVC on parameter values and CoV in the ACC. Volume-based smoothing data are shown in gray scale (Vs8 - 8mm fwhm in dark gray; Vs10 - 10mm fwhm in light gray) and the surface-smoothing data are shown in color ranging from 15mm (red) to 40mm (yellow) (s15-s40).*

OFC Results

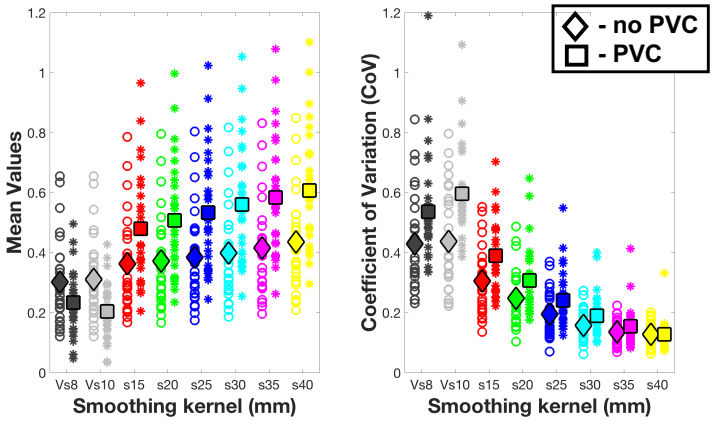
GE Advance Scanner (PSF 7mm)

[^{18}F]-FDOPA



Siemens HRRT Scanner (PSF 3mm)

[^{18}F]-Fallypride



[^{11}C]-NNC112

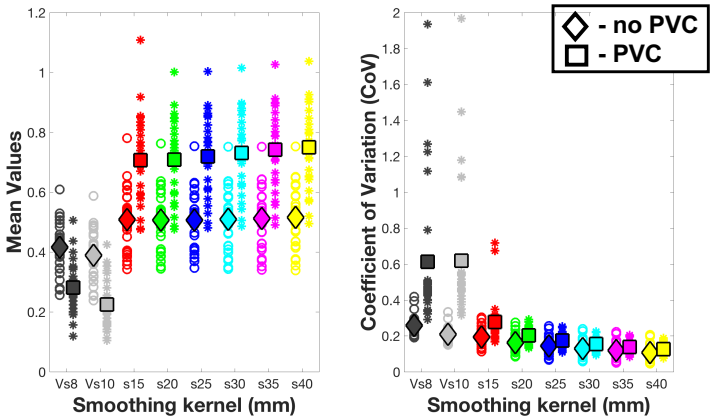


Figure 61. *Effects of surface smoothing and PVC on parameter values and CoV in the OFC. Volume-based smoothing data are shown in gray scale (Vs8 - 8mm fwhm in dark gray; Vs10 - 10mm fwhm in light gray) and the surface-smoothing data are shown in color ranging from 15mm (red) to 40mm (yellow) (s15-s40).*

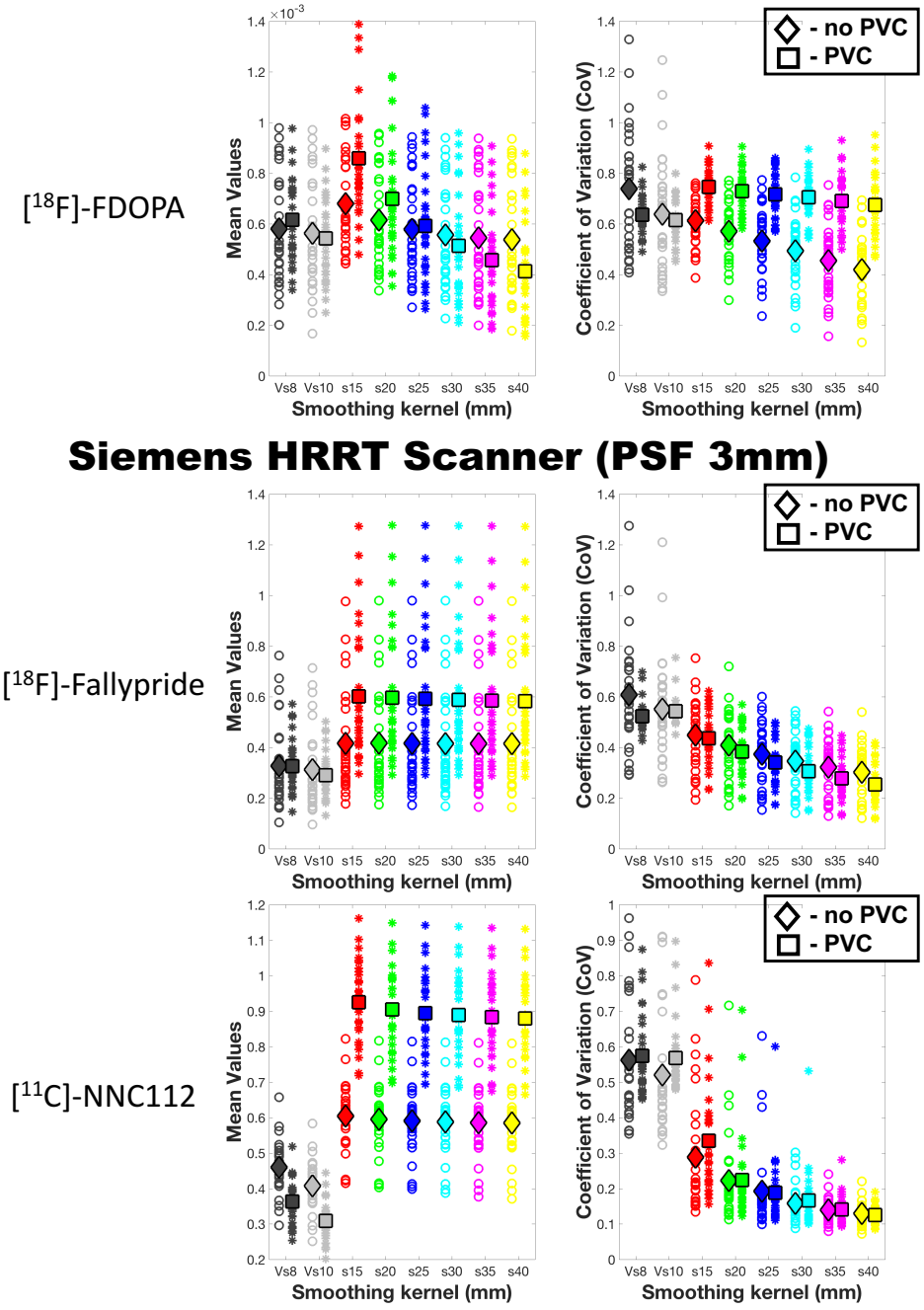


***Figure 62**. Effects of surface smoothing and PVC on mean values and CoV in occipital cortex. Volume-based smoothing data are shown in gray scale (Vs8 - 8mm fwhm in dark gray; Vs10 - 10mm fwhm in light gray) and the surface-smoothing data are shown in color ranging from 15mm (red) to 40mm (yellow) (s15-s40).*

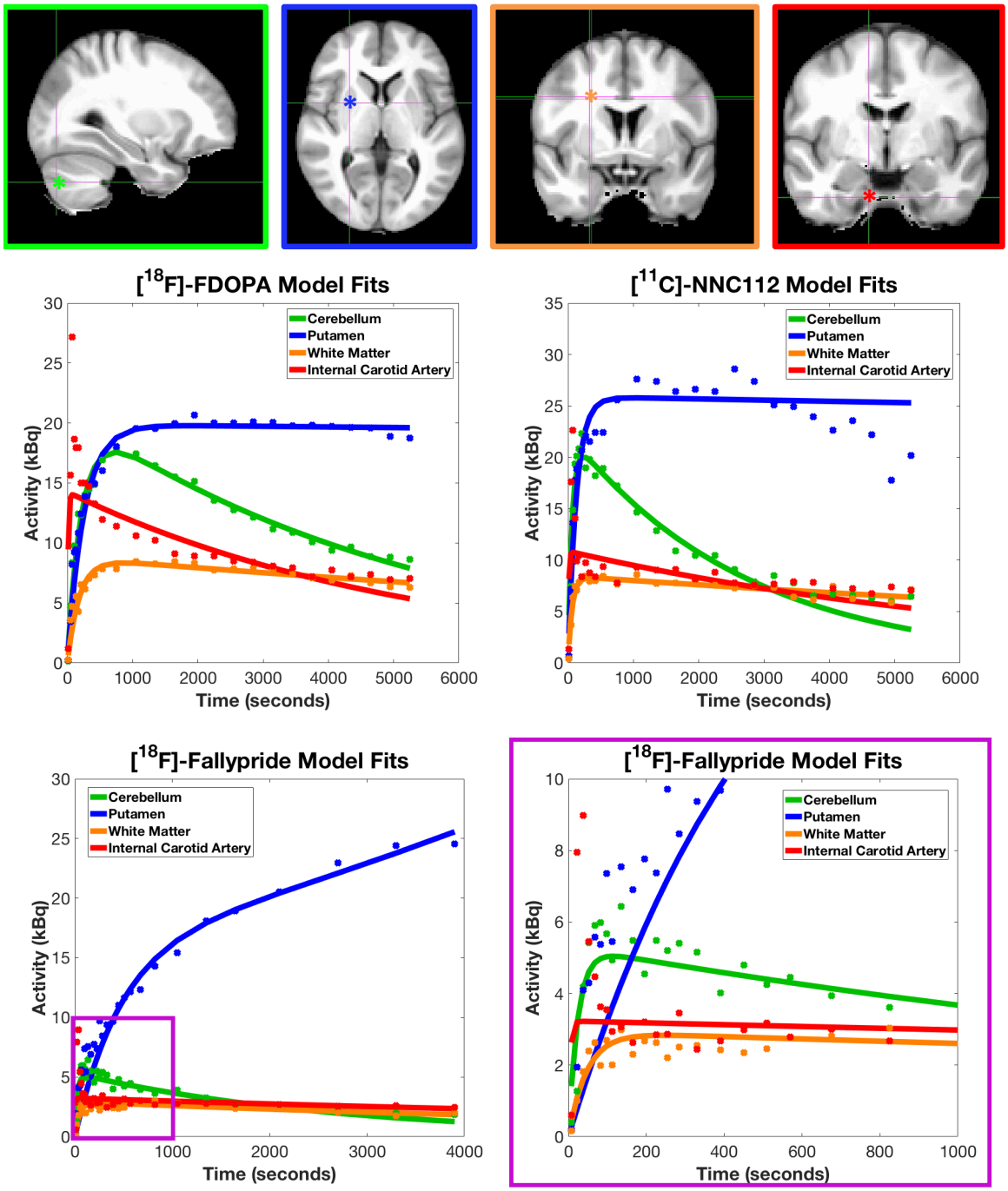


Figure 63. *Data and model-fitting results for an example subject. The data points (*) are from the single voxels indicated in the MRI image at the top of this figure. For the [^{18}F]-Fallypride tracer, the data are shown for the first 4000 seconds of the scan (note that the entire scan lasts about 13,500 seconds, but only the first 4000 seconds are used for the model-fitting) as well as a zoomed in section of the first 1000 second of the scan (indicated with a magenta box) to better show the data points and model-fitting in the cerebellum, white matter, and internal carotid artery example voxels.*

7

Future Work

Contents

7.1 Overview of Future Work
7.2 Optimization and Implementation of PET Methodological Advancements
7.3 Validation of Dopamine PET PCA Results
7.4 Role of Dopamine in Other Types of Reward-Guided Behavior

7.1 Overview of Future Work

Further work is necessary to complete our understanding of dopamine's role in reward-guided behavior. In reference to the work included in this document, it is first necessary to implement the described methodological advancements in PET data analysis in order to have improved and reliable cortical signal. This includes implementation of both the surface-based PET processing pipeline and the optimized reference region selection method. Second, the work described here is limited to looking at only two phenotypes related to reward-guided behavior: foraging and increased body mass index. The role of dopamine in other types of learning and decision-making should also be examined including those behaviors described in Section 2.2. Lastly, cortical values should be included in the PCA of dopamine synthesis capacity and D_1 and D_2 receptor availability that is described in Chapter 5. Furthermore, the PCA

results should be validated with an independent cohort of subjects to ensure reliability and reproducibility.

7.2 Optimization and Implementation of PET Methodological Advancements

There are a number of limitations to current PET methods (see Section 6.1), which make it difficult to measure reliable PET signal in the prefrontal cortex. The two methods that are presented in Chapter 6 address these limitations. Thus far, both of these methods have completed the testing phase. The purpose of the testing phase was two-fold. First, it was necessary to test out different parameters to see how they compared to each other. For the surface-based analysis pipeline, this included comparing various smoothing kernels as well as the effect of partial volume correction. For the reference region optimization method, most of the methods development has focused on acceleration of the model-fitting procedure and development of an algorithm for the automated selection of voxels for the reference region. The results of the testing phase have been promising and have helped guide the optimization of parameters to be used in the entire cohort.

This project has two distinct future directions. First, both the surface-based analysis pipeline and the reference region optimization method need to be implemented in the analysis of the data of all participants who have completed PET scans. Cortical PET values will then be extracted and used in either region of interest, voxelwise, or PCA analyses such as those described in Chapters 4 and 5. In addition, both methods require more work before they are optimized.

For the surface-based analysis pipeline, this includes streamlining the scripts to utilize the NIH supercomputing resources in order to decrease processing time. In addition, the results of the in-house pipeline described in Section 6.2 will be compared to the PETsurfer tools for partial volume correction, surface-based analysis- and kinetic modeling included in the newest version of Freesurfer (version 6, released in January of 2017).

For the reference region optimization method, three main changes are necessary. First, to speed up the model-fitting process, I plan to implement a feature allowing the user to select the optimization method used to fit the time activity curve at each voxel to the descriptive model of exponential uptake and decay. The current form of the code uses the Nelder-Mead numerical method, which is a versatile but slow method commonly applied to nonlinear optimization problems when the derivative is unknown [215]. However, a more appropriate optimization method for this specific application is the Levenburg-Marquardt algorithm [231] since it is possible to differentiate the function that we are optimizing (the sum of the squares of the error between the data points and the parameterized descriptive function). This method will speed up the model-fitting procedure tremendously.

The second change that is needed for the reference region optimization method is to further test and improve the automatic voxel selection algorithm. The current method was developed based on theoretical properties of the tissue types that I wanted to include in the reference region along with tweaks to the algorithm based on empirical data from the testing data that has been run so far.

However, one potential change that could improve the current algorithm would be to calculate the total distance metric as the product of the individual distances for each parameter instead of the sum. This change makes it more important for all three parameters to be close to the ideal since a large deviation of one would cause a much larger difference in the total distance value with multiplication rather than addition.

Finally, re-writing the reference region optimization code in another programming language such as python or C would also have some benefits. This would allow the incorporation of more sophisticated optimization and parallelization tools that are available in those programming languages and would make it easier to distribute the open-source code for others to use since users would not need a Matlab license and compiler toolbox to make changes to the code.

7.3 Validation of Dopamine PCA Results

To ensure that component weights from a principal component analysis are reliable and representative of a population, it is necessary to validate PCA results in an independent sample. This principle is termed “cross-validation” and was first proposed in 1951 as a means to assess the effectiveness of model weights [232], however, cross-validation can also be used to determine the suitable number of components that describe the data.

For validating the effectiveness or generalization of the PCA model, there are a few commonly used approaches for cross-validation. If the sample size is large enough, the ideal approach would be to run a PCA on a training sample of

data to calculate component weights for each of the variables of interest (PET measures in our case). The results from the training set are then used to estimate data for the test sample and compared to the actual data for the test sample by calculating the predicted residual error sum of squares (PRESS) [233]. If the sample of data is small, such as in our case, a similar approach can be taken in which only the data from a single subject or small group of subjects is left out of the training set and used in the PRESS calculation. This "leave-one-out" method is repeated multiple times and the PRESS is summed across all iterations. The smaller the PRESS in the test sample, the better the quality of the PCA results.

For calculating how many components are required to adequately describe the data, there are several different techniques [234]. Each of the various techniques has their own strengths and weaknesses. A simple approach to determine the number of components is to plot the eigenvalues of each component according to their size ("scree" plot) and subjectively determining if there is an "elbow" or turn in the scree plot where there is a dramatic change in slope [233]. Another commonly used rule is to keep the components that have eigenvalues larger than the average, which would be 1 in our case [233]. However, this method can result in missing important information that may be held in the components with lower eigenvalues. A review of the commonly used methods found that eigenvector cross-validation (or "Random model") was superior in cases involving few variables and samples when computational effort was considered [234]. This method involves repeatedly leaving out one sample

of data, performing PCA on the remaining data, and then calculating a PRESS for the left-out sample based on the results of the PCA. The number of components is chosen as the case that minimizes the PRESS value. Thus far, the scree plot method and eigenvalue cut-off methods have been used in the PCA of the PET region of interest data, however, the eigenvector cross-validation would be a more quantitative method for selecting an appropriate number of components in this case where there are few variables and samples [234].

7.4 Role of Dopamine in Other Types of Reward-Guided Behavior

This thesis includes an investigation of the role of dopamine synthesis and receptor profile in two phenotypes related to food reward-guided behavior in humans (increased body mass index and foraging behavior). However, we know that dopamine plays a role in many other aspects of reward-guided learning and decision-making. Two specific behaviors for which I have collected but not yet analyzed the data include comparative decision making and the effects of reward environment volatility (see [28]) as well as credit assignment of rewards to actions and stimuli (see [14]). In particular, I predict that there are overlapping dopamine-related neural mechanisms that are generalizable across many different aspects of reward guided behavior. To ask that question, I plan to use canonical correlation analysis (CCA), which is a method for identifying patterns of covariance across two different sets of variables (reward-guided behavioral measures and dopamine PET values in this case).

8

Conclusions

We are at the forefront of a revolutionary era for neuroscience. With huge funding endeavors such as the BRAIN Initiative and large-scale collections of open-access data such as the Human Connectome Project, new technologies for studying the brain are being developed at an impressive pace. Breakthroughs in optogenetic techniques have allowed scientists to be able to stimulate and measure specific neurons and circuits and methods such as CLARITY and expansion microscopy have allowed detailed structural mapping of neural circuitry. These developments have led to exciting studies dissecting the neural circuitry of the dopamine reward system in freely moving rats [20] and mammals [235]. Likewise, designer receptors called DREADDs have allowed specific targeting of the direct and indirect pathways of the striatal dopamine system to isolate their individual contributions to behavioral sensitization with repeated drug exposure [236] and have increased the understanding of the role of D_2 receptor signaling in compulsive drug use and food consumption [237].

Despite these breakthroughs in measuring and manipulating the dopamine system in animals, the tools available for human research studies lag behind. Human research is necessary if we want to study higher mental

functions, such as reward-guided learning and decision making. We also cannot be sure that mechanisms uncovered in animals apply to humans unless we replicate them in human studies. Lastly, if we want to discover the pathophysiology underlying mental illnesses for which animal models are lacking, we must study individuals who have those illnesses.

Focusing on the food-reward related phenotypes addressed in this thesis, the challenges of western lifestyles such as the overwhelming abundance of fatty high calorie food coupled with increasingly sedentary lifestyles are unique to human beings. The decisions that we make about how and where to seek food such as which restaurant to go to for dinner, or what snack to buy from the vending machine, cannot be replicated in animal models. Thinking about foraging behavior in a broader context not just related to food, decisions that we make about how to spend our time also have uniquely human attributes.

Animal models have provided a great deal of insight into the neural mechanisms underlying reward-guided behaviors and dopamine signaling in response to reward receipt or omission. For example, we have learned that neurons in the ACC play a key role in foraging decisions [30], the lateral OFC is required for specific reward credit assignment [15], and that phasic dopamine signals of reward prediction errors in either the positive or negative direction are essential for synaptic plasticity and learning in many situations [238]. We have also learned a great deal from computational modeling of reward-guided behaviors, which has been especially helpful for generating useful mechanistic predictions and testable hypotheses such as the link between phasic dopamine

responses and temporal difference models [239], tonic dopamine and the average reward rate [59], and dopamine receptors and the explore-exploit tradeoff [60].

The results presented in this thesis provide insight into the dopaminergic basis of two phenotypes related to reward-guided behavior in the context of food rewards. These findings are significant because they increase our understanding of the neural circuitry underlying body mass regulation as well as the contribution of dopamine to individual sensitivity to variables in the reward environment that affect foraging behavior. It is essential to first understand the neurocircuitry underlying normal reward-guided behavior in order to have a framework upon which to develop interventions or biomarkers for treatment response.

In Chapter 4, we demonstrated a link between dopamine synthesis and receptor availability and increased body mass index. While prior studies had asked similar questions with PET imaging in humans, this was the largest and first to date to use three different dopamine PET tracers in the same individuals. The study presented in Chapter 5 was the first to directly measure the link between dopamine and foraging behavior in humans. Our findings support existing computational models of dopamine's role in encoding the average reward rate of the environment [59] and explore-exploit tradeoffs [60]. The PET data analysis methods presented in Chapter 6 provide tools for researchers to increase cortical PET signal and optimize reference region selection when a high-quality MRI is not available. Hopefully these advancements will lead to

more studies investigating the role of cortical dopamine on reward-guided behaviors in humans.

In the short-term, the two studies presented here on the dopaminergic basis of food-reward related phenotypes both provide evidence to support theoretical and computational predictions. These findings build on the scientific knowledge base upon which future studies will be based. The PET data analysis methods we developed can be implemented immediately to improve cortical measurements and hopefully lead to a better understanding of the role of cortical dopamine in reward-guided behaviors. In addition, the PET parcellation method can be used to improve reference region selection in PET datasets without an MRI scan or with poor MRI quality that is insufficient for MRI-based segmentation.

In the intermediate future, our work can provide a framework upon which future studies can build. For example, longitudinal studies that scan participants at multiple timepoints can be used to measure dynamic changes in dopamine function and see how those relate to changes in body mass index. This would allow for clarification about the causality of the correlations found between increased BMI and dopamine synthesis capacity in the hypothalamus as well as decreased midbrain D_2 receptors. In addition, collection of larger datasets with more information on diet and exercise could allow for the investigation of subgroups of participants with different leading contributors to their obesity. With regards to the dopaminergic basis of foraging behavior, future studies could use PET tracers such as [^{11}C]-Raclopride to measure dopamine release during task

performance in order to build upon the correlations that were identified here. In addition, pharmacological manipulations could be used to alter dopamine levels and assess any resulting effects on foraging behavior.

In the long-term, these findings may lead to the development of targeted treatments and biomarkers for tracking treatment response or predicting risk. If longitudinal studies are used to map the dynamic relationship between dopamine synthesis capacity and receptor availability and body mass, predictive algorithms could be developed to identify individuals at higher risk for weight gain or obesity related complications. This could hopefully be extended to study the link between dopamine and weight gain seen with dopaminergic medications such as antipsychotics. This common side effect of second-generation antipsychotics can lead to metabolic syndrome and is a major factor in reducing medication compliance. Being able to stratify patients who are at a higher risk of antipsychotic-induced weight gain could allow for more intense preventative measures such as diet and exercise interventions as well as help guide treatment decisions towards medications with fewer metabolic side effects. The methods presented here also have important potential long-term implications. Specifically, if the PET parcellation method presented here is widely adopted, it could reduce PET research costs by eliminating the need to collect structural MRI scans for region segmentation.

The work presented in this thesis provides both experimental evidence supporting computational models describing dopamine's role in reward-guided behavior in humans as well as methodological advancements to improve in-vivo

quantification of dopamine function in humans. These are the first and largest studies to directly measure three different aspects of dopamine function in humans and link them to different aspects of reward-guided behavior. More work is needed to assess the role of dopamine in other aspects of reward-guided behavior and to translate findings from animal studies to human behavior.

Appendices

A

Partial Volume Correction Methods for PET Data Analysis

Contents

A.1 Geometric Transfer Matrix Method for Partial Volume Correction of Region of Interest Data
A.2 "Modified" Muller-Gartner Algorithm for Partial Volume Correction of Voxelwise Data

A.1 Geometric Transfer Matrix Method for Partial Volume Correction of Region of Interest Data

Partial volume correction was implemented using the PVELab software [188]. For region of interest (ROI) data, we used the geometric transfer matrix method described by Rousset and colleagues [240]. In this method, the measured value in each ROI (t_j) (82 ROIs in our case, including cortical and subcortical gray matter regions, white matter, and cerebrospinal fluid) is considered to be the sum of the true activity in each ROI (T_i) scaled by a weighting factor (w_{ij}), which represents the contribution of each of the other i ROIs to the signal in ROI j (see Equation 1).

$$t_j = \sum_{i=1}^{N} w_{ij} T_i \qquad \text{Eq. 1}$$

where t_j is the mean value observed within ROI_j and is assumed to be uniform throughout the ROI. A system of linear equations for each ROI is built, known as the geometric transfer matrix (GTM), which can then be solved for the true values (T_i) (see Equation 2).

$$\begin{bmatrix} t_1 \\ t_2 \\ \vdots \\ t_N \end{bmatrix} = \begin{bmatrix} w_{11} & w_{21} & \cdots & w_{N1} \\ w_{12} & w_{22} & & \vdots \\ \vdots & & \ddots & \vdots \\ w_{1N} & w_{2N} & \cdots & w_{NN} \end{bmatrix} \mathrm{X} \begin{bmatrix} T_1 \\ T_2 \\ \vdots \\ T_N \end{bmatrix} \qquad \text{Eq. 2}$$

The off-diagonal weighting factors represent the fraction of spill-in activity from the other ROIs into the current ROI_j.

The measured activity values for each ROI (t_j) are extracted as the mean value of all voxels in the ROI using a deterministic ROI file generated from each individual subject's T1-weighted MRI scan segmentation (using Freesurfer 6.0 with manual adjustments, as described in Section 3.5). The weighting factors (w_{ij}) are calculated using a three-dimensional PET simulator developed by Ma, Y. et al. [241, 242] that incorporates physical characteristics of the PET scanner such as the spatial resolution (input by the user as the point spread function of the specific scanner used), attenuation (loss of signal due to absorption by the body or scattering out of the field of view of the detectors), and random coincidences (detection of two photons 180 degrees apart that occur by chance and not by being emitted from a single true source). Remember from Section 6.1.2 that the point spread function (PSF) is the blurring of a point source of radiation that describes the spatial resolution of the scanner, which is limited by the detector size, positron range before an annihilation event, photon noncollinearity, and acquisition mode. The physical characteristics used in the

PET simulator software were determined from PET studies using a phantom with known true source values. The PET simulator starts with a single unit of activity in each of the ROIs, convolves that with the point spread function of the PET scanner and then applies the image reconstruction algorithm, including attenuation correction and correction for random coincidences to generate an image of what that known unit function in a single ROI would look like in a measured PET image. These images are called the regional spread functions (RSF_i). Each weighting factor w_{ij} is then calculated as the proportion of the total RSF_i that falls within the boundary of that particular ROI_j. Lastly, the true ROI values (***T***) are calculated by left multiplying the vector containing the measured ROI values (***t***) by the inverse of the matrix containing the weighting factors (***w***) (see Equation 3).

$$\boldsymbol{w}^{-1}\boldsymbol{t} = \boldsymbol{T} \qquad \text{Eq. 3}$$

A.2 "Modified" Muller-Gartner Algorithm for Partial Volume Correction of Voxelwise Data

For voxelwise partial volume correction, we used the "modified" Muller-Gartner (MG) algorithm [187, 188]. This algorithm has two main parts. First, the observed PET image (I_{obs}) is defined as the convolution of the actual distribution of radioactivity (I_{actual}) and the three-dimensional point spread function of the PET scanner (h) (see Equation 4).

$$I_{obs} = I_{actual} \otimes h \qquad \text{Eq. 4}$$

Second, I_{actual} is made up of the linear sum of the images comprising signal from the gray matter (I_{gray}), white matter (I_{white}) and cerebrospinal fluid (I_{CSF}) (see Equation 5).

$$I_{actual} = I_{gray} + I_{white} + I_{CSF} \quad \text{Eq. 5}$$

Combining Equations 4 and 5, we can re-write the equation for the observed signal (Equation 6).

$$I_{obs} = I_{gray} \otimes h + I_{white} \otimes h + I_{CSF} \otimes h \quad \text{Eq. 6}$$

The activity within the cerebrospinal fluid (CSF) and white matter are assumed to be constant and known. The spatial pattern of gray matter, CSF, and white matter are determined from the T1-weighted MRI scan using a probabilistic segmentation algorithm implemented with SPM8 (Wellcome Trust Centre for Neuroimaging, University College London). This gives us images of probabilities of each tissue type for each voxel in the brain that take values between 0 and 1 (X_{gray}, X_{white}, and X_{CSF}). The white matter activity is determined from the geometric transfer matrix method (described in A.1) using the corrected value for the white matter ROI (T_{white}), which is the modification to the original Muller-Gartner algorithm yielding the name “modified” MG. The true CSF signal (I_{CSF}) is assumed to be zero since CSF does not have metabolic (or dopaminergic in our case) activity, so we do not expect spill-in of signal from the CSF to the gray matter. A three-dimensional image of white matter signal I_{white} is generated by multiplying the white matter ROI value T_{white} by the probability map of white

matter in each voxel and then convoluting that by the point spread function of the scanner (see Equation 7).

$$I_{white} = T_{white} * X_{white} \quad \text{Eq. 7}$$

The same equation holds true for the gray matter, however, the true value (T_{gray}) is the unknown that we are solving for (Equation 8).

$$I_{gray} = T_{gray} * X_{gray} \quad \text{Eq. 8}$$

We can now re-write Equation 6 as:

$$I_{obs} = (T_{gray} * X_{gray}) \otimes h + (T_{white} * X_{white}) \otimes h \quad \text{Eq. 9}$$

and solve for T_{gray} by subtracting the white matter contribution from the observed PET signal and then dividing by the convolution of the spatial distribution of the gray matter probabilistic spatial distribution map (X_{gray}) and the point spread function (h):

$$T_{gray} = \frac{I_{obs} - (T_{white} * X_{white}) \otimes h}{X_{gray} \otimes h} \quad \text{Eq. 10}$$

B

Validity of Simplified Reference Tissue Model (SRTM) for Calculating [^{11}C]-NNC112 and [^{18}F]-Fallypride BP_{ND}

Contents

B.1 Assumptions of the SRTM Model
B.2 Validity of the SRTM Model for [11C]-NNC112
B.3 Validity of the SRTM Model for [18F]-Fallypride

B.1 Assumptions of the SRTM Model

The simplified reference tissue model (SRTM) is used for the analysis of reversibly binding PET receptor studies and was developed by Lammertsma and Hume [82] as an alternative to the full reference tissue method (or 4 parameter reference tissue method) [243]. Compared to the full reference tissue method, the SRTM has been shown to be less dependent on parameter starting values and gives more stable and consistent parameter estimates [82]. The SRTM assumes the following compartment model (**Figure 64**):

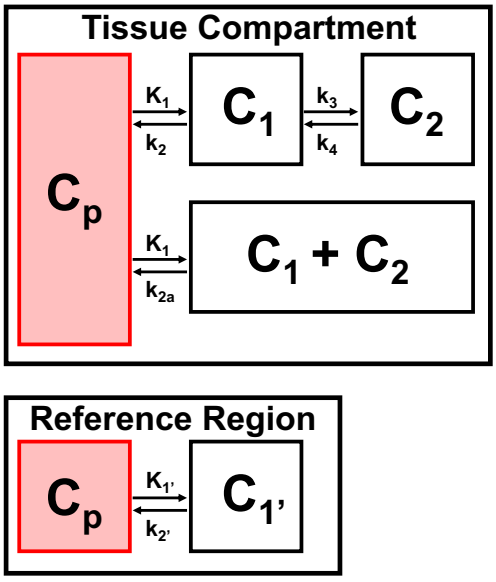


***Figure 64**. Compartment model for SRTM method*

The assumptions of the SRTM model are as follows (http://doc.pmod.com/PDF/PKIN.pdf):

1) The distribution volume in the tissue of interest and the reference region is assumed to be equal ($K_1/k_2=K_1'/k_2'$). This assumption is required for all reference region-based methods (compared to analysis methods using arterial sampling).
2) Specific to the SRTM, the second assumption is that the kinetics in the tissue of interest is such that it is hard to distinguish the free and bound compartments, allowing the tissue of interest compartment to be modeled with a one-tissue compartment model. If this assumption is not valid, the BP_{ND} estimates will be biased. For this assumption to be met, there must be a rapid equilibrium between the free, non-specifically bound, and specifically bound compartments. Importantly,

it has been suggested that the SRTM might also be valid for tracers that do not perfectly fulfill this constraint [244].

One approach to determine whether assumption #2 is valid for a particular PET tracer is to see if the time-activity curve of the region of interest can be fitted satisfactorily with a single tissue compartment, such that there is not much improvement when a two-tissue compartment model is used instead [82]. The results of this approach for both [^{11}C]-NNC112 and [^{18}F]-Fallypride will be detailed in Sections B.2. and B.3.

Another reference tissue model that has been used in prior [^{11}C]-NNC112 studies [245, 246] and has been suggested to be good for tracers with two tissue kinetics such as [^{18}F]-Fallypride (http://doc.pmod.com/PDF/PKIN.pdf) is Ichise's Multilinear Reference Tissue Model (MRTM) [247]. The MRTM is similar to the Logan plot method for analysis of receptor data [248] in such that it does not assume a specific number of compartments in the tissue voxels (compared to the SRTM that assumes that the data can be modeled with a 1-tissue compartment model). In other words, the MRTM model does not assume a quick equilibrium between the free and non-specific compartment and the specific binding compartment. Instead, a t* parameter is defined as the time at which equilibrium is reached (we use 42.5 minutes for [^{18}F]-Fallypride and 41.25 minutes for [^{11}C]-NNC112), and only data after that time is used for the linear fitting. As a way to assess whether the assumptions made in the SRTM model are valid, we applied both the SRTM and MRTM reference tissue models in a sample of [^{18}F]-

Fallypride (49 subjects) and [^{11}C]-NNC112 (59 subjects) data and present the results in Sections B.2 and B.3.

B.2 Validity of the SRTM Model for [^{11}C]-NNC112

Initial validation work for the [^{11}C]-NNC112 tracer showed that a two-tissue compartment model using an arterial input function was valid for binding potential calculations [249-250]. The two tissue compartments are a combined free and non-specifically bound compartment and a specifically bound compartment. The two-tissue compartment (2TC) model yielded binding potential values in agreement with the known distribution of D_1 receptors from post-mortem studies. In addition, the binding potentials with the 2TC model had excellent identifiability (as measured by a low error in the parameter estimation) and were highly reliable over time (test-retest intraclass correlation coeffficients around 0.9). Subsequent work compared the 2TC with an arterial input function to reference region models such as the SRTM [251]. Specifically, the study by Catafau et al. found that there was no effect of modeling method (2TC vs. SRTM) on binding potential values ($F=0.004$, $p=0.950$) and that similar results were found with both methods. Furthermore, the SRTM method has also been used in other published studies with [^{11}C]-NNC112 [252, 253].

Lastly, we compared binding potential values in the bilateral putamen between the SRTM and the MRTM reference region methods in a sample of 59 subjects. Since the MRTM method does not assume that the tissue can be modeled with one compartment, correlation between the values obtained from these two methods can help clarify whether or not this assumption is valid (or

whether any violation of this assumption biases parameter estimation). We found a very strong correlation between the bilateral putamen BP_{ND} values calculated with the MRTM and SRTM methods (Pearson r=0.918, p=1.44e-24; see Figure **65**).

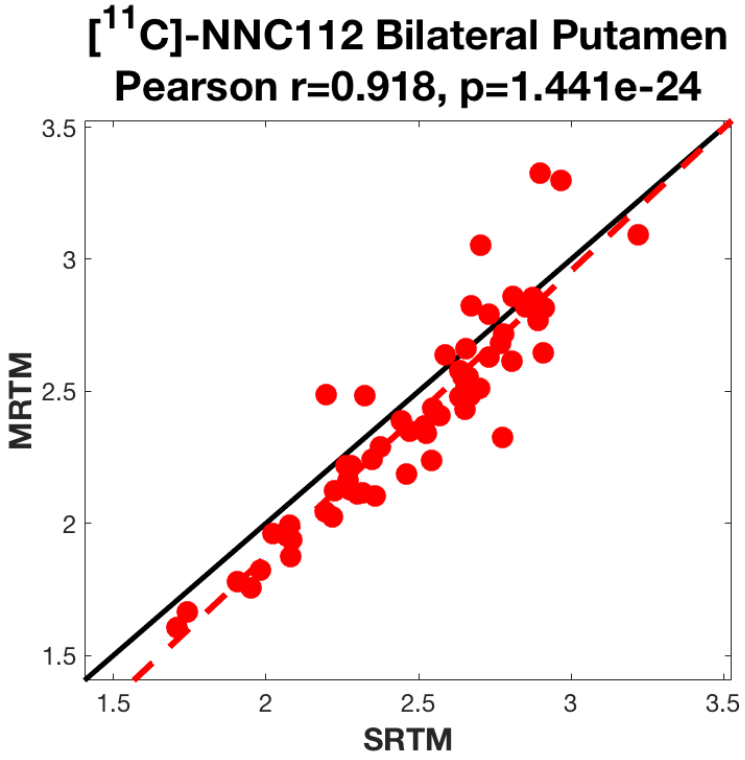


***Figure 65**. Correlation between SRTM and MRTM methods for [^{11}C]-NNC112 (59 subjects). Pearson r=0.918, p=1.441e-24. Plotted values are the binding potentials for the bilateral putamen region of interest. The red dotted line is the best fit line of the data and the black solid line is the depiction of a perfectly linear relationship between the values.*

B.3 Validity of the SRTM Model for [^{18}F]-Fallypride

Like [^{11}C]-NNC112, the use of the SRTM for analyzing [^{18}F]-Fallypride data was validated in an early study that collected arterial blood from a cohort of healthy controls and compared the binding potential values from a two-tissue compartment model (2TC) with an arterial input function to reference region

methods such as the SRTM [254]. Specifically, this early study found a very strong correlation between striatal binding potential values obtained using the 2TC and SRTM methods ($r=0.95$, $p<0.01$), which is even higher than the correlation for [^{11}C]-Raclopride ($r=0.91$, $p<0.01$), the tracer for which the SRTM was initially developed. This suggests that the kinetics of [^{18}F]-Fallypride data are such that the calculated binding potential values are not biased by any potential violations in the assumptions of the SRTM model. Numerous subsequently published [^{18}F]-Fallypride studies have also used the SRTM model [255-260].

Furthermore, comparing binding potential values from other reference region methods (that do not have the assumption of the tissue of interest being adequately modeled as a 1-tissue compartment) has yielded very consistent results. Specifically, Siessmeier et al. found that striatal binding potential values calculated using the SRTM method correlated very well with those calculated using the Logan plot method ($r=0.99$, $p<0.005$) [248] and the simple ratio method ($r=0.88$, $p<0.005$) [254]. In addition, Vernaleken et al. tested data from 100 subjects comparing the transient equilibrium method (TEM) [261] with the SRTM and found a high correspondence between SRTM and TEM BP_{ND} values in multiple brain regions (linear regression analysis for putamen: slope = 0.852, r^2 = 0.80, $p<0.0001$; thalamus: slope = 0.965, r^2 = 0.94, $p<0.0001$; inferior temporal cortex: slope = 0.841, r^2 = 0.87, $p<0.0001$) [262]. In our sample of 49 subjects, we compared BP_{ND} values in the putamen using the MRTM and SRTM methods since the MRTM model does not have that assumption of the bound and

unbound tracer being adequately modeled with a single tissue compartment. We found very good correspondence between these two methods (Pearson r=0.769, p=1.059e-10; see **Figure 66**).

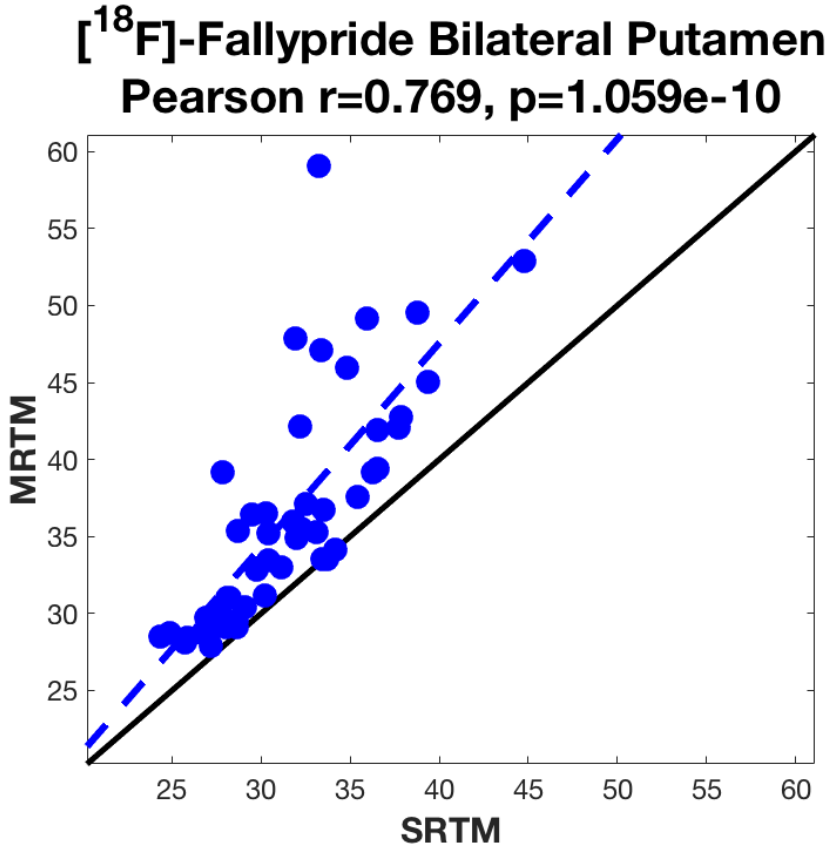


***Figure 66**. Correlation between SRTM and MRTM methods for [^{18}F]-Fallypride (49 subjects). Pearson r=0.769, p=1.059e-10. Plotted values are the binding potentials for the bilateral putamen region of interest. The red dotted line is the best fit line of the data and the black solid line is the depiction of a perfectly linear relationship between the values.*

References

[1] E. L. Charnov, "Optimal foraging, the marginal value theorem," *Theoretical population biology,* vol. 9, no. 2, pp. 129-136, 1976.

[2] W. Schultz, P. Dayan, and P. R. Montague, "A Neural Substrate of Prediction and Reward," *Science,* vol. 275, no. 5306, pp. 1593-1599, 1997.

[3] P. N. Tobler, C. D. Fiorillo, and W. Schultz, "Adaptive coding of reward value by dopamine neurons," *Science,* vol. 307, no. 5715, pp. 1642-1645, 2005.

[4] J. A. Waltz, M. J. Frank, B. M. Robinson, and J. M. Gold, "Selective Reinforcement Learning Deficits in Schizophrenia Support Predictions from Computational Models of Striatal-Cortical Dysfunction," *Biological Psychiatry,* vol. 62, no. 7, pp. 756-764, 2007.

[5] S. Grant, C. Contoreggi, and E. D. London, "Drug abusers show impaired performance in a laboratory test of decision making," *Neuropsychologia,* vol. 38, no. 8, pp. 1180-1187, 2000.

[6] G. F. Koob, "Dopamine, addiction and reward," *Seminars in Neuroscience,* vol. 4, no. 2, pp. 139-148, 1992.

[7] L. Deserno *et al.*, "Ventral striatal dopamine reflects behavioral and neural signatures of model-based control during sequential decision making," *Proceedings of the National Academy of Sciences of the United States of America,* vol. 112, no. 5, pp. 1595-1600, 2015.

[8] B. B. Doll, K. G. Bath, N. D. Daw, and M. J. Frank, "Variability in Dopamine Genes Dissociates Model-Based and Model-Free Reinforcement Learning," *The Journal of Neuroscience,* vol. 36, no. 4, p. 1211, 2016.

[9] K. Wunderlich, P. Smittenaar, and Raymond J. Dolan, "Dopamine Enhances Model-Based over Model-Free Choice Behavior," *Neuron,* vol. 75, no. 3, pp. 418-424, 2012.

[10] M. F. S. Rushworth and T. E. J. Behrens, "Choice, uncertainty and value in prefrontal and cingulate cortex," *Nat Neurosci,* vol. 11, no. 4, pp. 389-397, 2008.

[11] L. T. Hunt, N. Kolling, A. Soltani, M. W. Woolrich, M. F. Rushworth, and T. E. Behrens, "Mechanisms underlying cortical activity during value-guided choice," *Nature neuroscience,* vol. 15, no. 3, pp. 470-476, 2012.

[12] G. Jocham, A. Constantinescu, A. Ianni, M. Kahn, and T. E. J. Behrens, "Separable parallel mechanisms for reward-guided learning," in *Organization for Human Brain Mapping*, Seattle, WA, 2013.

[13] E. A. Murray, S. P. Wise, and S. E. V. Rhodes, "What Can Different Brains Do with Reward?," *Neurobiology of sensation and reward,* 2011.

[14] G. Jocham *et al.*, "Reward-Guided Learning with and without Causal Attribution," *Neuron,* vol. 90, no. 1, pp. 177-190, 2016.
[15] M. E. Walton, T. E. J. Behrens, M. J. Buckley, P. H. Rudebeck, and M. F. S. Rushworth, "Separable Learning Systems in the Macaque Brain and the Role of Orbitofrontal Cortex in Contingent Learning," *Neuron,* vol. 65, no. 6, pp. 927-939, 2010.
[16] Suzanne N. Haber and Timothy E. J. Behrens, "The Neural Network Underlying Incentive-Based Learning: Implications for Interpreting Circuit Disruptions in Psychiatric Disorders," *Neuron,* vol. 83, no. 5, pp. 1019-1039, 2014.
[17] J. Olds and P. Milner, "Positive reinforcement produced by electrical stimulation of septal area and other regions of rat brain," *Journal of comparative and physiological psychology,* vol. 47, no. 6, p. 419, 1954.
[18] A. E. Kelley and K. C. Berridge, "The Neuroscience of Natural Rewards: Relevance to Addictive Drugs," *The Journal of Neuroscience,* vol. 22, no. 9, p. 3306, 2002.
[19] W. A. Carlezon Jr, R. A. Wise, and W. A. Carlezon Jr, "Microinjections of phencyclidine (PCP) and related drugs into nucleus accumbens shell potentiate medial forebrain bundle brain stimulation reward," *Psychopharmacology,* vol. 128, no. 4, pp. 413-420, 1996.
[20] Ilana B. Witten *et al.*, "Recombinase-Driver Rat Lines: Tools, Techniques, and Optogenetic Application to Dopamine-Mediated Reinforcement," *Neuron,* vol. 72, no. 5, pp. 721-733, 2011.
[21] J. P. Aggleton, *The functional effects of amygdala lesions in humans: A comparison with findings from monkeys*. Wiley-Liss, 1992.
[22] H. Klüver and P. C. Bucy, "Preliminary analysis of functions of the temporal lobes in monkeys," *Archives of Neurology & Psychiatry,* vol. 42, no. 6, pp. 979-1000, 1939.
[23] Erie D. Boorman, Vani G. Rajendran, Jill X. O'Reilly, and Tim E. Behrens, "Two Anatomically and Computationally Distinct Learning Signals Predict Changes to Stimulus-Outcome Associations in Hippocampus," *Neuron,* vol. 89, no. 6, pp. 1343-1354, 2016.
[24] M. P. Noonan, R. B. Mars, and M. F. S. Rushworth, "Distinct roles of three frontal cortical areas in reward-guided behavior," *The Journal of Neuroscience,* vol. 31, no. 40, pp. 14399-14412, 2011.
[25] Matthew F. S. Rushworth, MaryAnn P. Noonan, Erie D. Boorman, Mark E. Walton, and Timothy E. Behrens, "Frontal Cortex and Reward-Guided Learning and Decision-Making," *Neuron,* vol. 70, no. 6, pp. 1054-1069, 2011.
[26] M. E. Walton, T. E. J. Behrens, M. P. Noonan, and M. F. S. Rushworth, "Giving credit where credit is due: orbitofrontal cortex and valuation in an uncertain world," *Annals of the New York Academy of Sciences,* vol. 1239, no. 1, pp. 14-24, 2011.
[27] E. D. Boorman, M. F. Rushworth, and T. E. Behrens, "Ventromedial prefrontal and anterior cingulate cortex adopt choice and default reference

frames during sequential multi-alternative choice," *The Journal of Neuroscience,* vol. 33, no. 6, pp. 2242-2253, 2013.
[28] T. E. Behrens, M. W. Woolrich, M. E. Walton, and M. F. Rushworth, "Learning the value of information in an uncertain world," *Nature neuroscience,* vol. 10, no. 9, pp. 1214-1221, 2007.
[29] N. Kolling, T. E. J. Behrens, R. B. Mars, and M. F. S. Rushworth, "Neural mechanisms of foraging," *Science,* vol. 336, no. 6077, pp. 95-98, 2012.
[30] B. Y. Hayden, J. M. Pearson, and M. L. Platt, "Neuronal basis of sequential foraging decisions in a patchy environment," *Nature neuroscience,* vol. 14, no. 7, pp. 933-939, 2011.
[31] W. Schultz, "Getting formal with dopamine and reward," *Neuron,* vol. 36, no. 2, pp. 241-263, 2002.
[32] S. N. Haber, "11 Neuroanatomy of Reward: A View from the Ventral Striatum," *Neurobiology of sensation and reward,* p. 235, 2011.
[33] K. Kobayashi, "Role of Catecholamine Signaling in Brain and Nervous System Functions: New Insights from Mouse Molecular Genetic Study," *Journal of Investigative Dermatology Symposium Proceedings,* vol. 6, no. 1, pp. 115-121, 2001.
[34] S. J. Russo and E. J. Nestler, "The brain reward circuitry in mood disorders," *Nat Rev Neurosci,* Review vol. 14, no. 9, pp. 609-625, 2013.
[35] G. E. Alexander, M. R. DeLong, and P. L. Strick, "Parallel organization of functionally segregated circuits linking basal ganglia and cortex," *Annual review of neuroscience,* vol. 9, no. 1, pp. 357-381, 1986.
[36] S. N. Haber and R. Calzavara, "The cortico-basal ganglia integrative network: The role of the thalamus," *Brain Research Bulletin,* vol. 78, no. 2, pp. 69-74, 2009.
[37] A. A. Grace, S. B. Floresco, Y. Goto, and D. J. Lodge, "Regulation of firing of dopaminergic neurons and control of goal-directed behaviors," *Trends in Neurosciences,* vol. 30, no. 5, pp. 220-227, 2007.
[38] S. N. Haber and M. J. Gdowski, "CHAPTER 21 - The Basal Ganglia A2 - PAXINOS, GEORGE," in *The Human Nervous System (Second Edition)*, J. K. Mai, Ed. San Diego: Academic Press, 2004, pp. 676-738.
[39] A. A. Grace and B. S. Bunney, "The control of firing pattern in nigral dopamine neurons: burst firing," *The Journal of Neuroscience,* vol. 4, no. 11, p. 2877, 1984.
[40] A. A. Grace and B. S. Bunney, "The control of firing pattern in nigral dopamine neurons: single spike firing," *The Journal of Neuroscience,* vol. 4, no. 11, p. 2866, 1984.
[41] W. Schultz, P. Apicella, and T. Ljungberg, "Responses of monkey dopamine neurons to reward and conditioned stimuli during successive steps of learning a delayed response task," *The Journal of Neuroscience,* vol. 13, no. 3, p. 900, 1993.
[42] P. N. Tobler, A. Dickinson, and W. Schultz, "Coding of Predicted Reward Omission by Dopamine Neurons in a Conditioned Inhibition Paradigm," *The Journal of Neuroscience,* vol. 23, no. 32, p. 10402, 2003.

[43] S. B. Floresco, A. R. West, B. Ash, H. Moore, and A. A. Grace, "Afferent modulation of dopamine neuron firing differentially regulates tonic and phasic dopamine transmission," *Nat Neurosci,* vol. 6, no. 9, pp. 968-973, 2003.

[44] Y. Goto, S. Otani, and A. A. Grace, "The Yin and Yang of dopamine release: a new perspective," *Neuropharmacology,* vol. 53, no. 5, pp. 583-587, 2007.

[45] Pamela F. Marcott, Aphroditi A. Mamaligas, and Christopher P. Ford, "Phasic Dopamine Release Drives Rapid Activation of Striatal D2-Receptors," *Neuron,* vol. 84, no. 1, pp. 164-176, 2014.

[46] E. K. Richfield, J. B. Penney, and A. B. Young, "Anatomical and affinity state comparisons between dopamine D 1 and D 2 receptors in the rat central nervous system," *Neuroscience,* vol. 30, no. 3, pp. 767-777, 1989.

[47] J. M. Liebman and L. L. Butcher, "Comparative involvement of dopamine and noradrenaline in rate-free self-stimulation in substantia nigra, lateral hypothalamus, and mesencephalic central gray," *Naunyn-Schmiedeberg's Archives of Pharmacology,* vol. 284, no. 2, pp. 167-194, 1974.

[48] R. A. Yokel and R. A. Wise, "Increased lever pressing for amphetamine after pimozide in rats: implications for a dopamine theory of reward," *Science,* vol. 187, no. 4176, p. 547, 1975.

[49] R. A. Wise, J. Spindler, H. deWit, and G. J. Gerberg, "Neuroleptic-induced "anhedonia" in rats: pimozide blocks reward quality of food," *Science,* vol. 201, no. 4352, pp. 262-264, 1978.

[50] J. W. Kebabian and D. B. Calne, "Multiple receptors for dopamine," *Nature,* vol. 277, no. 5692, pp. 93-96, 1979.

[51] C. A. Marsden, "Dopamine: the rewarding years," *British Journal of Pharmacology,* vol. 147, no. Suppl 1, pp. S136-S144, 2006.

[52] J. J. Day, M. F. Roitman, R. M. Wightman, and R. M. Carelli, "Associative learning mediates dynamic shifts in dopamine signaling in the nucleus accumbens," *Nat Neurosci,* Article vol. 10, no. 8, pp. 1020-1028, 2007.

[53] Y. K. Takahashi *et al.*, "Expectancy-related changes in firing of dopamine neurons depend on orbitofrontal cortex," *Nature neuroscience,* vol. 14, no. 12, pp. 1590-1597, 2011.

[54] J. Tian and N. Uchida, "Habenula Lesions Reveal that Multiple Mechanisms Underlie Dopamine Prediction Errors," *Neuron,* vol. 87, no. 6, pp. 1304-1316, 2015.

[55] N. Eshel, M. Bukwich, V. Rao, V. Hemmelder, J. Tian, and N. Uchida, "Arithmetic and local circuitry underlying dopamine prediction errors," *Nature,* Letter vol. 525, no. 7568, pp. 243-246, 2015.

[56] E. E. Steinberg, R. Keiflin, J. R. Boivin, I. B. Witten, K. Deisseroth, and P. H. Janak, "A causal link between prediction errors, dopamine neurons and learning," *Nat Neurosci,* Article vol. 16, no. 7, pp. 966-973, 2013.

[57] C. Y. Chang, G. R. Esber, Y. Marrero-Garcia, H.-J. Yau, A. Bonci, and G. Schoenbaum, "Brief optogenetic inhibition of dopamine neurons mimics endogenous negative reward prediction errors," *Nature neuroscience,* vol. 19, no. 1, pp. 111-116, 2016.

[58] A. A. Grace, "Phasic versus tonic dopamine release and the modulation of dopamine system responsivity: A hypothesis for the etiology of schizophrenia," *Neuroscience,* vol. 41, no. 1, pp. 1-24, 1991.
[59] Y. Niv, N. Daw, D. Joel, and P. Dayan, "Tonic dopamine: opportunity costs and the control of response vigor", *Psychopharmacology,* vol. 191, no. 3, pp. 507-520, 2007.
[60] M. D. Humphries, M. Khamassi, and K. Gurney, "Dopaminergic control of the exploration-exploitation trade-off via the basal ganglia," *Frontiers in Neuroscience,* vol. 6, 2012.
[61] J. A. Obeso *et al.*, "Functional organization of the basal ganglia: Therapeutic implications for Parkinson's disease," *Movement Disorders,* vol. 23, no. S3, pp. S548-S559, 2008.
[62] A. V. Kravitz, L. D. Tye, and A. C. Kreitzer, "Distinct roles for direct and indirect pathway striatal neurons in reinforcement," *Nature neuroscience,* vol. 15, no. 6, pp. 816-818, 2012.
[63] M. J. Frank, A. A. Moustafa, H. M. Haughey, T. Curran, and K. E. Hutchison, "Genetic triple dissociation reveals multiple roles for dopamine in reinforcement learning," *Proceedings of the National Academy of Sciences,* vol. 104, no. 41, pp. 16311-16316, 2007.
[64] S. M. L. Cox *et al.*, "Striatal D1 and D2 signaling differentially predict learning from positive and negative outcomes," *NeuroImage,* 2015.
[65] E. E. Steinberg, J. R. Boivin, B. T. Saunders, I. B. Witten, K. Deisseroth, and P. H. Janak, "Positive Reinforcement Mediated by Midbrain Dopamine Neurons Requires D1 and D2 Receptor Activation in the Nucleus Accumbens," *PLoS ONE,* vol. 9, no. 4, p. e94771, 2014.
[66] L. H. Schneider, J. Gibbs, and G. P. Smith, "Selective D-1 or D-2 receptor antagonists inhibit sucrose sham feeding in rats," 1986, vol. 7, pp. 294-295: ACADEMIC PRESS LTD 24-28 OVAL RD, LONDON, ENGLAND NW1 7DX.
[67] D. Clark and F. J. White, "Review: D1 dopamine receptor—the search for a function: A critical evaluation of the D1/D2 dopamine receptor classification and its functional implications," *Synapse,* vol. 1, no. 4, pp. 347-388, 1987.
[68] Y. Goto and A. A. Grace, "Dopaminergic modulation of limbic and cortical drive of nucleus accumbens in goal-directed behavior," *Nat Neurosci,* 10.1038/nn1471 vol. 8, no. 6, pp. 805-812, 2005.
[69] S. Yawata, T. Yamaguchi, T. Danjo, T. Hikida, and S. Nakanishi, "Pathway-specific control of reward learning and its flexibility via selective dopamine receptors in the nucleus accumbens," *Proceedings of the National Academy of Sciences,* vol. 109, no. 31, pp. 12764-12769, 2012.
[70] L. Hernandez and B. G. Hoebel, "Food reward and cocaine increase extracellular dopamine in the nucleus accumbens as measured by microdialysis," *Life Sciences,* vol. 42, no. 18, pp. 1705-1712, 1988.
[71] V. Bassareo and G. Di Chiara, "Differential responsiveness of dopamine transmission to food-stimuli in nucleus accumbens shell/core compartments," *Neuroscience,* vol. 89, no. 3, pp. 637-641, 1999.

[72] A. Hajnal, G. P. Smith, and R. Norgren, "Oral sucrose stimulation increases accumbens dopamine in the rat," *American Journal of Physiology - Regulatory, Integrative and Comparative Physiology,* vol. 286, no. 1, p. R31, 2003.
[73] Edward H. Nieh *et al.*, "Decoding Neural Circuits that Control Compulsive Sucrose Seeking," *Cell,* vol. 160, no. 3, pp. 528-541, 2015.
[74] T. T. Hills, "Animal Foraging and the Evolution of Goal-Directed Cognition," *Cognitive Science,* vol. 30, no. 1, pp. 3-41, 2006.
[75] M. S. Szczypka, R. J. Mandel, B. A. Donahue, R. O. Snyder, S. E. Leff, and R. D. Palmiter, "Viral Gene Delivery Selectively Restores Feeding and Prevents Lethality of Dopamine-Deficient Mice," *Neuron,* vol. 22, no. 1, pp. 167-178, 1999.
[76] M. Piel, I. Vernaleken, and F. Rösch, "Positron Emission Tomography in CNS Drug Discovery and Drug Monitoring," *Journal of Medicinal Chemistry,* vol. 57, no. 22, pp. 9232-9258, 2014.
[77] L.-H. Shen, M.-H. Liao, and Y.-C. Tseng, "Recent advances in imaging of dopaminergic neurons for evaluation of neuropsychiatric disorders," *BioMed Research International,* vol. 2012, 2012.
[78] N. D. Volkow *et al.*, "PET Evaluation of the Dopamine System of the Human Brain," *Journal of Nuclear Medicine,* vol. 37, no. 7, pp. 1242-1256, 1996.
[79] O. Prante, S. Maschauer, and A. Banerjee, "Radioligands for the dopamine receptor subtypes," *Journal of Labelled Compounds and Radiopharmaceuticals,* vol. 56, no. 3-4, pp. 130-148, 2013.
[80] A. Gjedde, "Calculation of cerebral glucose phosphorylation from brain uptake of glucose analogs in vivo: A re-examination," *Brain Research Reviews,* vol. 4, no. 2, pp. 237-274, 1982.
[81] C. S. Patlak, R. G. Blasberg, and J. D. Fenstermacher, "Graphical Evaluation of Blood-to-Brain Transfer Constants from Multiple-Time Uptake Data," *J Cereb Blood Flow Metab,* vol. 3, no. 1, pp. 1-7, 1983.
[82] A. A. Lammertsma and S. P. Hume, "Simplified Reference Tissue Model for PET Receptor Studies," *NeuroImage,* vol. 4, no. 3, pp. 153-158, 1996.
[83] Y. Benjamini and Y. Hochberg, "Controlling the false discovery rate: a practical and powerful approach to multiple testing," *Journal of the royal statistical society. Series B (Methodological),* pp. 289-300, 1995.
[84] C. R. Genovese, N. A. Lazar, and T. Nichols, "Thresholding of Statistical Maps in Functional Neuroimaging Using the False Discovery Rate," *NeuroImage,* vol. 15, no. 4, pp. 870-878, 2002.
[85] T. Nichols and S. Hayasaka, "Controlling the familywise error rate in functional neuroimaging: a comparative review," *Statistical Methods in Medical Research,* vol. 12, no. 5, pp. 419-446, 2003.
[86] W. H. O. (WHO), "Obesity and Overweight (Fact sheet no. 311)," ed, 2015.
[87] M. Ng *et al.*, "Global, regional, and national prevalence of overweight and obesity in children and adults during 1980–2013: a systematic analysis for

the Global Burden of Disease Study 2013," *The Lancet,* vol. 384, no. 9945, pp. 766-781, 2014.
[88] N. D. Volkow, G.-J. Wang, D. Tomasi, and R. D. Baler, "The Addictive Dimensionality of Obesity," *Biological Psychiatry,* vol. 73, no. 9, pp. 811-818, 2013.
[89] V. K. Doan, Y.-H. Choi, A. W. Kinyua, S. H. Moh, and K. W. Kim, "Leptin and Insulin Signaling in Dopaminergic Neurons: Relationship between Energy Balance and Reward System," (in English), *Frontiers in Psychology,* Review vol. 5, 2014.
[90] J. J. Cone, J. E. McCutcheon, and M. F. Roitman, "Ghrelin Acts as an Interface between Physiological State and Phasic Dopamine Signaling," *The Journal of Neuroscience,* vol. 34, no. 14, pp. 4905-4913, 2014.
[91] I. S. Farooqi, E. Bullmore, J. Keogh, J. Gillard, S. O'Rahilly, and P. C. Fletcher, "Leptin Regulates Striatal Regions and Human Eating Behavior," *Science,* vol. 317, no. 5843, pp. 1355-1355, 2007.
[92] M. M. Meguid *et al.*, "Hypothalamic dopamine and serotonin in the regulation of food intake," *Nutrition,* vol. 16, no. 10, pp. 843-857, 2000.
[93] S. O. Fetissov, M. M. Meguid, T. Sato, and L.-H. Zhang, "Expression of dopaminergic receptors in the hypothalamus of lean and obese Zucker rats and food intake," *American Journal of Physiology - Regulatory, Integrative and Comparative Physiology,* vol. 283, no. 4, pp. R905-R910, 2002.
[94] P. Martel and M. Fantino, "Mesolimbic dopaminergic system activity as a function of food reward: A microdialysis study," *Pharmacology Biochemistry and Behavior,* vol. 53, no. 1, pp. 221-226, 1996.
[95] P. J. Kenny, "Reward Mechanisms in Obesity: New Insights and Future Directions," *Neuron,* vol. 69, no. 4, pp. 664-679, 2011.
[96] J. M. Richard, D. C. Castro, A. G. DiFeliceantonio, M. J. F. Robinson, and K. C. Berridge, "Mapping brain circuits of reward and motivation: In the footsteps of Ann Kelley," *Neuroscience & Biobehavioral Reviews,* vol. 37, no. 9, Part A, pp. 1919-1931, 2013.
[97] N. D. Volkow, G.-J. Wang, and R. D. Baler, "Reward, dopamine and the control of food intake: implications for obesity," *Trends in cognitive sciences,* vol. 15, no. 1, pp. 37-46, 2011.
[98] G.-J. Wang *et al.*, "Brain dopamine and obesity," *The Lancet,* vol. 357, no. 9253, pp. 354-357, 2001.
[99] E. Stice, S. Spoor, C. Bohon, M. Veldhuizen, and D. Small, "Relation of Reward from Food Intake and Anticipated Food Intake to Obesity: A Functional Magnetic Resonance Imaging Study," *Journal of abnormal psychology,* vol. 117, no. 4, pp. 924-935, 2008.
[100] P. M. Johnson and P. J. Kenny, "Dopamine D2 receptors in addiction-like reward dysfunction and compulsive eating in obese rats," *Nat Neurosci,* vol. 13, no. 5, pp. 635-641, 2010.
[101] K. E. Demos, T. F. Heatherton, and W. M. Kelley, "Individual Differences in Nucleus Accumbens Activity to Food and Sexual Images Predict Weight

Gain and Sexual Behavior," *The Journal of Neuroscience,* vol. 32, no. 16, pp. 5549-5552, 2012.
[102] S. Yokum, C. N. Marti, A. Smolen, and E. Stice, "Relation of the multilocus genetic composite reflecting high dopamine signaling capacity to future increases in BMI," *Appetite,* vol. 87, no. 0, pp. 38-45, 2015.
[103] P. Y. Geha, K. Aschenbrenner, J. Felsted, S. S. O'Malley, and D. M. Small, "Altered hypothalamic response to food in smokers," *The American Journal of Clinical Nutrition,* vol. 97, no. 1, pp. 15-22, 2013.
[104] X. Sun *et al.*, "Basolateral Amygdala Response to Food Cues in the Absence of Hunger Is Associated with Weight Gain Susceptibility," *The Journal of Neuroscience,* vol. 35, no. 20, pp. 7964-7976, 2015.
[105] S. Nolan-Poupart, M. G. Veldhuizen, P. Geha, and D. M. Small, "Midbrain response to milkshake correlates with ad libitum milkshake intake in the absence of hunger," *Appetite,* vol. 60, pp. 168-174, 2013.
[106] K. P. Cosgrove, M. G. Veldhuizen, C. M. Sandiego, E. D. Morris, and D. M. Small, "Opposing relationships of BMI with BOLD and dopamine D2/3 receptor binding potential in the dorsal striatum," *Synapse,* pp. 2015.
[107] R. K. Babbs, X. Sun, J. Felsted, F. Chouinard-Decorte, M. G. Veldhuizen, and D. M. Small, "Decreased caudate response to milkshake is associated with higher body mass index and greater impulsivity," *Physiology & Behavior,* vol. 121, no. 0, pp. 103-111, 2013.
[108] Y. Rothemund *et al.*, "Differential activation of the dorsal striatum by high-calorie visual food stimuli in obese individuals," *NeuroImage,* vol. 37, no. 2, pp. 410-421, 2007.
[109] J. Ng, E. Stice, S. Yokum, and C. Bohon, "An fMRI study of obesity, food reward, and perceived caloric density. Does a low-fat label make food less appealing?," *Appetite,* vol. 57, no. 1, pp. 65-72, 2011.
[110] D. S. N. T. Le *et al.*, "Less activation of the left dorsolateral prefrontal cortex in response to a meal: a feature of obesity," *The American Journal of Clinical Nutrition,* vol. 84, no. 4, pp. 725-731, 2006.
[111] D. S. N. T. Le *et al.*, "Less activation in the left dorsolateral prefrontal cortex in the reanalysis of the response to a meal in obese than in lean women and its association with successful weight loss," *The American Journal of Clinical Nutrition,* vol. 86, no. 3, pp. 573-579, 2007.
[112] L. E. Martin *et al.*, "Neural Mechanisms Associated With Food Motivation in Obese and Healthy Weight Adults," *Obesity,* vol. 18, no. 2, pp. 254-260, 2010.
[113] J. J. Hendrikse, R. L. Cachia, E. J. Kothe, S. McPhie, H. Skouteris, and M. J. Hayden, "Attentional biases for food cues in overweight and individuals with obesity: a systematic review of the literature," *Obesity Reviews,* vol. 16, no. 5, pp. 424-432, 2015.
[114] S. Yokum, J. Ng, and E. Stice, "Attentional Bias to Food Images Associated With Elevated Weight and Future Weight Gain: An fMRI Study," *Obesity (Silver Spring, Md.),* vol. 19, no. 9, pp. 1775-1783, 2011.

[115] A. S. Bruce *et al.*, "Obese children show hyperactivation to food pictures in brain networks linked to motivation, reward and cognitive control," *International Journal Of Obesity,* Pediatric Highlight vol. 34, p. 1494, 2010.
[116] L. Batterink, S. Yokum, and E. Stice, "Body mass correlates inversely with inhibitory control in response to food among adolescent girls: An fMRI study," *NeuroImage,* vol. 52, no. 4, pp. 1696-1703, 2010.
[117] W. D. S. Killgore and D. A. Yurgelun-Todd, "Body mass predicts orbitofrontal activity during visual presentations of high-calorie foods," *Neuroreport,* vol. 16, no. 8, pp. 859-863, 2005.
[118] A. DelParigi, K. Chen, A. D. Salbe, E. M. Reiman, and P. A. Tataranni, "Sensory experience of food and obesity: a positron emission tomography study of the brain regions affected by tasting a liquid meal after a prolonged fast," *NeuroImage,* vol. 24, no. 2, pp. 436-443, 2005.
[119] S. Davids *et al.*, "Increased dorsolateral prefrontal cortex activation in obese children during observation of food stimuli," *International Journal Of Obesity,* Original Article vol. 34, p. 94, 2009.
[120] N. Medic *et al.*, "Increased body mass index is associated with specific regional alterations in brain structure," *Int J Obes,* Original Article vol. 40, no. 7, pp. 1177-1182, 2016.
[121] B. A. de Weijer *et al.*, "Lower striatal dopamine D(2/3) receptor availability in obese compared with non-obese subjects," *EJNMMI Research,* vol. 1, pp. 37-37, 2016
[122] L. T. Haltia *et al.*, "Effects of intravenous glucose on dopaminergic function in the human brain in vivo," *Synapse,* vol. 61, no. 9, pp. 748-756, 2007.
[123] G.-J. Wang *et al.*, "Enhanced Striatal Dopamine Release During Food Stimulation in Binge Eating Disorder," *Obesity,* vol. 19, no. 8, pp. 1601-1608, 2011.
[124] S. A. Eisenstein *et al.*, "A comparison of D2 receptor specific binding in obese and normal-weight individuals using PET with (N-[11C]methyl)benperidol," *Synapse,* vol. 67, no. 11, pp. 748-756, 2013.
[125] H. K. Karlsson *et al.*, "Obesity Is Associated with Decreased μ-Opioid But Unaltered Dopamine D2 Receptor Availability in the Brain," *The Journal of Neuroscience,* vol. 35, no. 9, pp. 3959-3965, 2015.
[126] S. A. Eisenstein *et al.*, "Emotional Eating Phenotype is Associated with Central Dopamine D2 Receptor Binding Independent of Body Mass Index," *Scientific Reports,* Article vol. 5, p. 11283, 2015.
[127] E. C. Gaiser *et al.*, "Elevated Dopamine D(2/3) Receptor Availability in Obese Individuals: A PET Imaging Study with [(11)C](+)PHNO," *Neuropsychopharmacology,* vol. 41, no. 13, pp. 3042-3050, 2016
[128] L. C. Dang, G. R. Samanez-Larkin, J. J. Castrellon, S. F. Perkins, R. L. Cowan, and D. H. Zald, "Associations between dopamine D2 receptor availability and BMI depend on age," *NeuroImage,* vol. 138, pp. 176-183, 2016.
[129] F. Caravaggio, S. Raitsin, P. Gerretsen, S. Nakajima, A. Wilson, and A. Graff-Guerrero, "Ventral Striatum Binding of a Dopamine D2/3 Receptor

Agonist But Not Antagonist Predicts Normal Body Mass Index," *Biological Psychiatry,* 2013.

[130] J. Guo, W. K. Simmons, P. Herscovitch, A. Martin, and K. D. Hall, "Striatal dopamine D2-like receptor correlation patterns with human obesity and opportunistic eating behavior," *Mol Psychiatry,* Immediate Communication vol. 19, no. 10, pp. 1078-1084, 2014.

[131] K. Blum, P. K. Thanos, and M. S. Gold, "Dopamine and glucose, obesity, and reward deficiency syndrome," *Frontiers in Psychology,* vol. 5, p. 919, 2014

[132] K. Blum *et al.*, "The D2 dopamine receptor gene as a determinant of reward deficiency syndrome," *Journal of the Royal Society of Medicine,* vol. 89, no. 7, pp. 396-400, 1996.

[133] B. M. Geiger, M. Haburcak, N. M. Avena, M. C. Moyer, B. G. Hoebel, and E. N. Pothos, "Deficits of mesolimbic dopamine neurotransmission in rat dietary obesity," *Neuroscience,* vol. 159, no. 4, pp. 1193-1199, 2009.

[134] E. Stice, S. Yokum, K. S. Burger, L. H. Epstein, and D. M. Small, "Youth at Risk for Obesity Show Greater Activation of Striatal and Somatosensory Regions to Food," *The Journal of Neuroscience,* vol. 31, no. 12, pp. 4360-4366, 2011.

[135] T. E. Robinson and K. C. Berridge, "The psychology and neurobiology of addiction: an incentive–sensitization view," *Addiction,* vol. 95, no. 8s2, pp. 91-117, 2000.

[136] M. First, M. Gibbon, R. Spitzer, and J. Williams, "User's Guide for the SCID-I for DSM-IV Axis I Disorders - Research Version," ed. New York: Biometrics Research, 1996.

[137] M. M. Meguid, Z.-J. Yang, and M. Koseki, "Eating induced rise in LHA-dopamine correlates with meal size in normal and bulbectomized rats," *Brain Research Bulletin,* vol. 36, no. 5, pp. 487-490, 1995.

[138] M. M. Meguid, Z.-J. Yang, and A. Laviano, "Meal size and number: relationship to dopamine levels in the ventromedial hypothalamic nucleus," *American Journal of Physiology-Regulatory, Integrative and Comparative Physiology,* vol. 272, no. 6, pp. R1925-R1930, 1997.

[139] M. Orosco, C. Rough, M. J. Meile, and S. Nicolaidis, "Spontaneous feeding-related monoamine changes in rostromedial hypothalamus of the obese Zucker rat: A microdialysis study," *Physiology & Behavior,* vol. 57, no. 6, pp. 1103-1106, 1995.

[140] Z.-J. Yang and M. M. Meguid, "LHA dopaminergic activity in obese and lean Zucker rats," *Neuroreport: An International Journal for the Rapid Communication of Research in Neuroscience,* 1995.

[141] K. C. Berridge and E. S. Valenstein. (1991). *What psychological process mediates feeding evoked by electrical stimulation of the lateral hypothalamus? (1 ed.)*

[142] G. Hernandez, H. Rajabi, J. Stewart, A. Arvanitogiannis, and P. Shizgal, "Dopamine tone increases similarly during predictable and unpredictable administration of rewarding brain stimulation at short inter-train intervals," *Behavioural Brain Research,* vol. 188, no. 1, pp. 227-232, 2008.

[143] V. M. André *et al.*, "Dopamine modulation of excitatory currents in the striatum is dictated by the expression of D1 or D2 receptors and modified by endocannabinoids," *European Journal of Neuroscience,* vol. 31, no. 1, pp. 14-28, 2010.
[144] E. P. Bello *et al.*, "Cocaine supersensitivity and enhanced motivation for reward in mice lacking dopamine D2 autoreceptors," *Nat Neurosci,* vol. 14, no. 8, pp. 1033-1038, 2011.
[145] K. C. Berridge, "'Liking' and 'wanting' food rewards: Brain substrates and roles in eating disorders," *Physiology & behavior,* vol. 97, no. 5, pp. 537-550, 2009.
[146] D. M. Small, R. J. Zatorre, A. Dagher, A. C. Evans, and M. Jones-Gotman, "Changes in brain activity related to eating chocolate," *Brain,* vol. 124, no. 9, pp. 1720-1733, 2001.
[147] N. M. Avena, P. Rada, N. Moise, and B. G. Hoebel, "Sucrose sham feeding on a binge schedule releases accumbens dopamine repeatedly and eliminates the acetylcholine satiety response," *Neuroscience,* vol. 139, no. 3, pp. 813-820, 2006.
[148] E. Stice, K. S. Burger, and S. Yokum, "Relative ability of fat and sugar tastes to activate reward, gustatory, and somatosensory regions," *The American Journal of Clinical Nutrition,* vol. 98, no. 6, pp. 1377-1384, 2013.
[149] D. M. Small, M. Jones-Gotman, and A. Dagher, "Feeding-induced dopamine release in dorsal striatum correlates with meal pleasantness ratings in healthy human volunteers," *NeuroImage,* vol. 19, no. 4, pp. 1709-1715, 2003.
[150] J. G. Ferreira, L. A. Tellez, X. Ren, C. W. Yeckel, and I. E. de Araujo, "Regulation of fat intake in the absence of flavour signalling," *The Journal of Physiology,* vol. 590, no. 4, pp. 953-972, 2012.
[151] N. Medic *et al.*, "Dopamine Modulates the Neural Representation of Subjective Value of Food in Hungry Subjects," *The Journal of Neuroscience,* vol. 34, no. 50, p. 16856, 2014.
[152] E. Stice, S. Spoor, J. Ng, and D. H. Zald, "Relation of obesity to consummatory and anticipatory food reward," *Physiology & Behavior,* vol. 97, no. 5, pp. 551-560, 2009.
[153] E. Stice, K. S. Burger, and S. Yokum, "Reward Region Responsivity Predicts Future Weight Gain and Moderating Effects of the TaqIA Allele," *The Journal of Neuroscience,* vol. 35, no. 28, pp. 10316-10324, 2015.
[154] J. A. Felsted, X. Ren, F. Chouinard-Decorte, and D. M. Small, "Genetically Determined Differences in Brain Response to a Primary Food Reward," *The Journal of Neuroscience,* vol. 30, no. 7, pp. 2428-2432, 2010.
[155] K. C. Berridge, C.-Y. Ho, J. M. Richard, and A. G. DiFeliceantonio, "The tempted brain eats: Pleasure and desire circuits in obesity and eating disorders," *Brain Research,* vol. 1350, pp. 43-64, 2010.
[156] S. Yokum, A. N. Gearhardt, J. L. Harris, K. D. Brownell, and E. Stice, "Individual Differences in Striatum Activity to Food Commercials Predict Weight Gain in Adolescents," *Obesity (Silver Spring, Md.),* vol. 22, no. 12, pp. 2544-2551, 2014.

[157] R. J. Cowie, "Optimal foraging in great tits (Parus major)," *Nature,* vol. 268, no. 5616, pp. 137-139, 1977.
[158] S. Constantino and N. Daw, "Learning the opportunity cost of time in a patch-foraging task," , *Cognitive, Affective, & Behavioral Neuroscience,* pp. 1-17, 2015.
[159] S. W. Kennerley, M. E. Walton, T. E. J. Behrens, M. J. Buckley, and M. F. S. Rushworth, "Optimal decision making and the anterior cingulate cortex," *Nat Neurosci,* vol. 9, no. 7, pp. 940-947, 2006.
[160] S. Constantino and N. D. Daw, "The neural mechanism of opportunity cost," in *Reinforcement Learning and Decision Making*, Princeton, NJ, 2013.
[161] Miriam C. Klein-Flügge, Laurence T. Hunt, Dominik R. Bach, Raymond J. Dolan, and Timothy E. J. Behrens, "Dissociable Reward and Timing Signals in Human Midbrain and Ventral Striatum," *Neuron,* vol. 72, no. 4, pp. 654-664, 2011.
[162] Yuji K. Takahashi, Angela J. Langdon, Y. Niv, and G. Schoenbaum, "Temporal Specificity of Reward Prediction Errors Signaled by Putative Dopamine Neurons in Rat VTA Depends on Ventral Striatum," *Neuron,* vol. 91, no. 1, pp. 182-193, 2016.
[163] N. R. Draper and H. Smith, *Applied Regression Analysis*. Hoboken, NJ: Wiley-Interscience.
[164] C. A. Altar, W. C. Boyar, E. Oei, and P. L. Wood, "Dopamine autoreceptors modulate the in vivo release of dopamine in the frontal, cingulate and entorhinal cortices," *Journal of Pharmacology and Experimental Therapeutics,* vol. 242, no. 1, pp. 115-120, 1987.
[165] F. Hefti, E. Melamed, B. J. Sahakian, and R. J. Wurtman, "Circling behavior in rats with partial, unilateral nigro-striatal lesions: effect of amphetamine, apomorphine, and DOPA," *Pharmacology Biochemistry and Behavior,* vol. 12, no. 2, pp. 185-188, 1980.
[166] Y. Agid, F. Javoy, and J. Glowinski, "Hyperactivity of remaining dopaminergic neurones after partial destruction of the nigro-striatal dopaminergic system in the rat," *Nature,* vol. 245, no. 144, pp. 150-151, 1973.
[167] I. Creese, D. R. Burt, and S. H. Snyder, "Dopamine receptor binding enhancement accompanies lesion-induced behavioral supersensitivity," *Science,* vol. 197, no. 4303, pp. 596-598, 1977.
[168] M. J. Zigmond, T. W. Berger, A. A. Grace, and E. M. Stricker, "Compensatory responses to nigrostriatal bundle injury," *Molecular and Chemical Neuropathology,* vol. 10, no. 3, pp. 185-200, 1989.
[169] J. Schweimer and W. Hauber, "Dopamine D1 receptors in the anterior cingulate cortex regulate effort-based decision making," *Learning & Memory,* vol. 13, no. 6, pp. 777-782, 2006.
[170] C. P. Ford, "The role of D2-autoreceptors in regulating dopamine neuron activity and transmission," *Neuroscience,* vol. 282, pp. 13-22, 2014.
[171] J. Hahn, P. H. M. Kullmann, J. P. Horn, and E. S. Levitan, "D2 Autoreceptors Chronically Enhance Dopamine Neuron Pacemaker

Activity," *The Journal of Neuroscience,* vol. 26, no. 19, pp. 5240-5247, 2006.
[172] A. Oster, P. Faure, and B. S. Gutkin, "Mechanisms for multiple activity modes of VTA dopamine neurons," *Frontiers in Computational Neuroscience,* vol. 9, p. 95, 2015.
[173] K. Ikemoto *et al.*, "Tyrosine hydroxylase and aromatic l-amino acid decarboxylase do not coexist in neurons in the human anterior cingulate cortex," *Neuroscience Letters,* vol. 269, no. 1, pp. 37-40, 1999.
[174] V. L. Cropley *et al.*, "Pre- and post-synaptic dopamine imaging and its relation with frontostriatal cognitive function in Parkinson disease: PET studies with [11C]NNC 112 and [18F]FDOPA," *Psychiatry Research: Neuroimaging,* vol. 163, no. 2, pp. 171-182, 2008.
[175] G. Aston-Jones and J. D. Cohen, "AN INTEGRATIVE THEORY OF LOCUS COERULEUS-NOREPINEPHRINE FUNCTION: Adaptive Gain and Optimal Performance," *Annual Review of Neuroscience,* vol. 28, no. 1, pp. 403-450, 2005.
[176] P. S. Goldman-Rakic, M. S. Lidow, J. F. Smiley, and M. S. Williams, "The anatomy of dopamine in monkey and human prefrontal cortex," in *Advances in Neuroscience and Schizophrenia*, vol. 36, A. H. Tuma, E. M. Stricker, and S. Gershon, Eds. Journal of Neural Transmission. Springer Vienna, 1992, pp. 163-177.
[177] A. F. T. Arnsten, J. X. Cai, B. L. Murphy, and P. S. Goldman-Rakic, "Dopamine D1 receptor mechanisms in the cognitive performance of young adult and aged monkeys," *Psychopharmacology,* vol. 116, no. 2, pp. 143-151, 1994.
[178] G. V. Williams and P. S. Goldman-Rakic, "Modulation of memory fields by dopamine Dl receptors in prefrontal cortex," *Nature,* vol. 376, no. 6541, pp. 572-575, 1995.
[179] A. Abi-Dargham *et al.*, "Increased prefrontal cortical D1 receptors in drug naïve patients with schizophrenia: a PET study with [11C]NNC112," *Journal of Psychopharmacology,* vol. 26, no. 6, pp. 794-805, June 1, 2012 2012.
[180] R. Z. Goldstein and N. D. Volkow, "Dysfunction of the prefrontal cortex in addiction: neuroimaging findings and clinical implications," *Nat Rev Neurosci,* vol. 12, no. 11, pp. 652-669, 2011.
[181] T. E. Robinson, G. Gorny, E. Mitton, and B. Kolb, "Cocaine self-administration alters the morphology of dendrites and dendritic spines in the nucleus accumbens and neocortex," *Synapse,* vol. 39, no. 3, pp. 257-266, 2001.
[182] M. S. Lidow, J. D. Elsworth, and P. S. Goldman-Rakic, "Down-Regulation of the D1 and D5 Dopamine Receptors in the Primate Prefrontal Cortex by Chronic Treatment with Antipsychotic Drugs," *Journal of Pharmacology and Experimental Therapeutics,* vol. 281, no. 1, p. 597, 1997.
[183] V. Bisagno, B. González, and F. J. Urbano, "Cognitive enhancers versus addictive psychostimulants: The good and bad side of dopamine on

prefrontal cortical circuits," *Pharmacological Research,* vol. 109, pp. 108-118, 2016.
[184] M. Soret, S. L. Bacharach, and I. Buvat, "Partial-Volume Effect in PET Tumor Imaging," *Journal of Nuclear Medicine,* vol. 48, no. 6, pp. 932-945, 2007.
[185] H. Zaidi and A. Alavi, "Current Trends in PET and Combined (PET/CT and PET/MR) Systems Design," *PET Clinics,* vol. 2, no. 2, pp. 109-123, 2007.
[186] O. Rousset, A. Rahmim, A. Alavi, and H. Zaidi, "Partial Volume Correction Strategies in PET," *PET Clinics,* vol. 2, no. 2, pp. 235-249, 2007.
[187] H. W. Müller-Gärtner *et al.*, "Measurement of Radiotracer Concentration in Brain Gray Matter Using Positron Emission Tomography: MRI-Based Correction for Partial Volume Effects," *Journal of Cerebral Blood Flow & Metabolism,* vol. 12, no. 4, pp. 571-583, 1992.
[188] M. Quarantelli *et al.*, "Integrated Software for the Analysis of Brain PET/SPECT Studies with Partial-Volume-Effect Correction," *Journal of Nuclear Medicine,* vol. 45, no. 2, pp. 192-201, 2004.
[189] D. N. Greve *et al.*, "Cortical surface-based analysis reduces bias and variance in kinetic modeling of brain PET data," *NeuroImage,* vol. 92, pp. 225-236, 2014.
[190] D. N. Greve *et al.*, "Different partial volume correction methods lead to different conclusions: An 18F-FDG-PET study of aging," *NeuroImage,* vol. 132, pp. 334-343, 2016.
[191] V. Beliveau, C. Svarer, V. G. Frokjaer, G. M. Knudsen, D. N. Greve, and P. M. Fisher, "Functional connectivity of the dorsal and median raphe nuclei at rest," *NeuroImage,* vol. 116, pp. 187-195, 2015.
[192] J. M. DuBois *et al.*, "Metabotropic Glutamate Receptor Type 5 (mGluR5) Cortical Abnormalities in Focal Cortical Dysplasia Identified In Vivo With [11C]ABP688 Positron-Emission Tomography (PET) Imaging," *Cerebral Cortex,* vol. 26, no. 11, pp. 4170-4179, 2016.
[193] E. Herranz *et al.*, "Neuroinflammatory component of gray matter pathology in multiple sclerosis," *Annals of Neurology,* vol. 80, no. 5, pp. 776-790, 2016.
[194] V. Beliveau *et al.*, "A High-Resolution In Vivo Atlas of the Human Brain's Serotonin System," *The Journal of Neuroscience,* vol. 37, no. 1, p. 120, 2017.
[195] D. H. Salat *et al.*, "Thinning of the Cerebral Cortex in Aging," *Cerebral Cortex,* vol. 14, no. 7, pp. 721-730, 2004.
[196] B. Fischl *et al.*, "Whole Brain Segmentation: Automated Labeling of Neuroanatomical Structures in the Human Brain," *Neuron,* vol. 33, no. 3, pp. 341-355, 2002.
[197] A. M. Dale, B. Fischl, and M. I. Sereno, "Cortical Surface-Based Analysis: I. Segmentation and Surface Reconstruction," *NeuroImage,* vol. 9, no. 2, pp. 179-194, 1999.
[198] Z. S. Saad and R. C. Reynolds, "SUMA," *NeuroImage,* vol. 62, no. 2, pp. 768-773, 2012.

[199] G. Rajkowska and P. S. Goldman-Rakic, "Cytoarchitectonic Definition of Prefrontal Areas in the Normal Human Cortex: II. Variability in Locations of Areas 9 and 46 and Relationship to the Talairach Coordinate System," *Cerebral Cortex,* vol. 5, no. 4, pp. 323-337, 1995.
[200] B. Fischl *et al.*, "Automatically Parcellating the Human Cerebral Cortex," *Cerebral Cortex,* vol. 14, no. 1, pp. 11-22, 2004.
[201] B. Fischl and A. M. Dale, "Measuring the thickness of the human cerebral cortex from magnetic resonance images," *Proceedings of the National Academy of Sciences,* vol. 97, no. 20, pp. 11050-11055, 2000.
[202] M. S. Lidow, P. S. Goldman-Rakic, D. W. Gallager, and P. Rakic, "Distribution of dopaminergic receptors in the primate cerebral cortex: Quantitative autoradiographic analysis using [3H]raclopride, [3H]spiperone and [3H]SCH23390," *Neuroscience,* vol. 40, no. 3, pp. 657-671, 1991.
[203] M. Bentivoglio and M. Morelli, "Chapter I The organization and circuits of mesencephalic dopaminergic neurons and the distribution of dopamine receptors in the brain," *Handbook of Chemical Neuroanatomy,* vol. 21, pp. 1-107, 2005.
[204] M. Slifstein *et al.*, "[11C]NNC 112 Selectivity for Dopamine D1 and Serotonin 5-HT2A Receptors: A PET Study in Healthy Human Subjects," *Journal of Cerebral Blood Flow & Metabolism,* vol. 27, no. 10, pp. 1733-1741, 2007.
[205] A. Pazos, A. Probst, and J. M. Palacios, "Serotonin receptors in the human brain—IV. Autoradiographic mapping of serotonin-2 receptors," *Neuroscience,* vol. 21, no. 1, pp. 123-139, 1987.
[206] H. Hall, G. Sedvall, O. Magnusson, J. Kopp, C. Halldin, and L. Farde, "Distribution of D1- and D2-Dopamine Receptors, and Dopamine and Its Metabolites in the Human Brain," *Neuropsychopharmacology,* vol. 11, p. 245, 1994.
[207] D. H. Anderson, *Compartmental modeling and tracer kinetics*. Springer Science & Business Media, 1983.
[208] A. Gjedde *et al.*, "Dopa decarboxylase activity of the living human brain," *Proceedings of the National Academy of Sciences,* vol. 88, no. 7, pp. 2721-2725, 1991.
[209] E. D. Morris, C. J. Endres, K. C. Schmidt, B. T. Christian, R. F. Muzic, and R. E. Fisher, "Kinetic modeling in positron emission tomography," *Emission Tomography: The Fundamentals of PET and SPECT. Academic, San Diego,* 2004.
[210] M. Schain, K. Varnäs, Z. Cselényi, C. Halldin, L. Farde, and A. Varrone, "Evaluation of Two Automated Methods for PET Region of Interest Analysis," *Neuroinformatics,* vol. 12, no. 4, pp. 551-562, 2014.
[211] P. Razifar, H. Engler, A. Ringheim, S. Estrada, A. Wall, and B. Långström, "An Automated Method for Delineating a Reference Region Using Masked Volumewise Principal-Component Analysis in 11C-PIB PET," *Journal of Nuclear Medicine Technology,* vol. 37, no. 1, pp. 38-44, 2009.
[212] E. Rissanen *et al.*, "Automated Reference Region Extraction and Population-Based Input Function for Brain [11C]TMSX PET Image

Analyses," *Journal of Cerebral Blood Flow & Metabolism,* vol. 35, no. 1, pp. 157-165, 2014.
[213] Kenhub, "Arteries of the Brain - Anatomy and Clinical Notes," ed, 2017. © Kenhub (www.kenhub.com)
[214] Kenhub, "Veins of the Brain," ed, 2017. © Kenhub (www.kenhub.com)
[215] J. A. Nelder and R. Mead, "A Simplex Method for Function Minimization," *The Computer Journal,* vol. 7, no. 4, pp. 308-313, 1965.
[216] C. A. Schneider, W. S. Rasband, and K. W. Eliceiri, "NIH Image to ImageJ: 25 years of image analysis," *Nat Meth,* vol. 9, no. 7, pp. 671-675, 2012.
[217] N. A. Karakatsanis, E. Fokou, and C. Tsoumpas, "Dosage optimization in positron emission tomography: state-of-the-art methods and future prospects," *American Journal of Nuclear Medicine and Molecular Imaging,* vol. 5, no. 5, pp. 527-547, 2015.
[218] P. F. Watson and A. Petrie, "Method agreement analysis: A review of correct methodology," *Theriogenology,* vol. 73, no. 9, pp. 1167-1179, 2010.
[219] C. R. Denegar and D. W. Ball, "Assessing reliability and precision of measurement: an introduction to intraclass correlation and standard error of measurement," *Journal of sport rehabilitation,* vol. 2, no. 1, pp. 35-42, 1993.
[220] K. O. McGraw and S. P. Wong, "Forming inferences about some intraclass correlation coefficients," *Psychological methods,* vol. 1, no. 1, p. 30, 1996.
[221] D. V. Cicchetti, "Guidelines, criteria, and rules of thumb for evaluating normed and standardized assessment instruments in psychology," *Psychological assessment,* vol. 6, no. 4, p. 284, 1994.
[222] D. P. Eisenberg *et al.*, "Brain-derived neurotrophic factor (BDNF) Val66Met polymorphism differentially predicts hippocampal function in medication-free patients with schizophrenia," *Mol Psychiatry,* Original Article vol. 18, no. 6, pp. 713-720, 2013.
[223] K. Ishibashi, C. L. Robertson, M. A. Mandelkern, A. T. Morgan, and E. D. London, "The Simplified Reference Tissue Model with (18)F-fallypride PET: Choice of Reference Region," *Molecular imaging,* vol. 12, no. 8, 2013.
[224] L. Descarries, B. Lemay, G. Doucet, and B. Berger, "Regional and laminar density of the dopamine innervation in adult rat cerebral cortex," *Neuroscience,* vol. 21, no. 3, pp. 807-824, 1987.
[225] V. Sossi, J. E. Holden, R. de la Fuente-Fernandez, T. J. Ruth, and A. J. Stoessl, "Effect of dopamine loss and the metabolite 3-O-methyl-[18F] fluoro-dopa on the relation between the 18F-fluorodopa tissue input uptake rate constant Kocc and the [18F] fluorodopa plasma input uptake rate constant Ki," *Journal of Cerebral Blood Flow & Metabolism,* vol. 23, no. 3, pp. 301-309, 2003.
[226] A. L. Whone, D. L. Bailey, P. Remy, N. Pavese, and D. J. Brooks, "A Technique for Standardized Central Analysis of 6-18F-Fluoro-l-DOPA PET

Data from a Multicenter Study," *Journal of Nuclear Medicine,* vol. 45, no. 7, pp. 1135-1145, 2004.
[227] A. Egerton, A. Demjaha, P. McGuire, M. A. Mehta, and O. D. Howes, "The test-retest reliability of 18F-DOPA PET in assessing striatal and extrastriatal presynaptic dopaminergic function," *NeuroImage,* vol. 50, no. 2, pp. 524-531, 2010.
[228] E. Aflaki, W. Westbroek, and E. Sidransky, "The Complicated Relationship between Gaucher Disease and Parkinsonism: Insights from a Rare Disease," *Neuron,* vol. 93, no. 4, pp. 737-746.
[229] H.-C. Cheng, C. M. Ulane, and R. E. Burke, "Clinical Progression in Parkinson's Disease and the Neurobiology of Axons," *Annals of neurology,* vol. 67, no. 6, pp. 715-725, 2010.
[230] P. Zanotti-Fregonara, K. Chen, J.-S. Liow, M. Fujita, and R. B. Innis, "Image-derived input function for brain PET studies: many challenges and few opportunities," *Journal of Cerebral Blood Flow & Metabolism,* vol. 31, no. 10, pp. 1986-1998, 2011.
[231] D. W. Marquardt, "An algorithm for least-squares estimation of nonlinear parameters," *Journal of the society for Industrial and Applied Mathematics,* vol. 11, no. 2, pp. 431-441, 1963.
[232] C. I. Mosier, "I. Problems and Designs of Cross-Validation 1," *Educational and Psychological Measurement,* vol. 11, no. 1, pp. 5-11, 1951.
[233] H. Abdi and L. J. Williams, "Principal component analysis," *Wiley Interdisciplinary Reviews: Computational Statistics,* vol. 2, no. 4, pp. 433-459, 2010.
[234] R. Bro, K. Kjeldahl, A. K. Smilde, and H. A. L. Kiers, "Cross-validation of component models: A critical look at current methods," *Analytical and Bioanalytical Chemistry,* vol. 390, no. 5, pp. 1241-1251, 2008.
[235] F. Zhang *et al.*, "Optogenetics in Freely Moving Mammals: Dopamine and Reward," *Cold Spring Harbor Protocols,* vol. 2015, no. 8, 2015.
[236] S. M. Ferguson *et al.*, "Transient neuronal inhibition reveals opposing roles of indirect and direct pathways in sensitization," *Nat Neurosci,* vol. 14, no. 1, pp. 22-24, 2011.
[237] P. J. Kenny, G. Voren, and P. M. Johnson, "Dopamine D2 receptors and striatopallidal transmission in addiction and obesity," *Current Opinion in Neurobiology,* vol. 23, no. 4, pp. 535-538, 2013.
[238] W. Schultz, "Updating dopamine reward signals," *Current Opinion in Neurobiology,* vol. 23, no. 2, pp. 229-238, 2013.
[239] P. W. Glimcher, "Understanding dopamine and reinforcement learning: The dopamine reward prediction error hypothesis," *Proceedings of the National Academy of Sciences,* vol. 108, no. Supplement 3, pp. 15647-15654, 2011.
[240] O. G. Rousset, Y. Ma, and A. C. Evans, "Correction for Partial Volume Effects in PET: Principle and Validation," *Journal of Nuclear Medicine,* vol. 39, no. 5, pp. 904-911, 1998.
[241] Y. Ma and A. C. Evans, "Analytical modeling of PET imaging with correlated functional and structural images," in *1996 IEEE Nuclear*

Science Symposium. Conference Record, 1996, vol. 3, pp. 1817-1821 vol.3.

[242] Y. Ma, M. Kamber, and A. C. Evans, "3D simulation of pet brain images using segmented MRI data and positron tomograph characteristics," *Computerized Medical Imaging and Graphics,* vol. 17, no. 4, pp. 365-371, 1993.

[243] A. A. Lammertsma *et al.*, "Comparison of Methods for Analysis of Clinical [11C]Raclopride Studies," *Journal of Cerebral Blood Flow & Metabolism,* vol. 16, no. 1, pp. 42-52, 1996.

[244] R. Buchert and F. Thiele, "The simplified reference tissue model for SPECT/PET brain receptor studies - Interpretation of its parameters," *Nuklearmedizin,* vol. 47, no. 4, pp. 167-174, 2008.

[245] D. Wooten *et al.*, "Occupancy and functional response to D1 receptor ligands assessed by concurrent PET/fMRI," *Journal of Nuclear Medicine,* vol. 55, no. supplement 1, pp. 30-30, 2014.

[246] D. M. Cannon, J. M. Klaver, S. A. Peck, D. Rallis-Voak, K. Erickson, and W. C. Drevets, "Dopamine Type-1 Receptor Binding in Major Depressive Disorder Assessed using Positron Emission Tomography and [(11)C]NNC-112," *Neuropsychopharmacology : official publication of the American College of Neuropsychopharmacology,* vol. 34, no. 5, pp. 1277-1287, 2009.

[247] M. Ichise *et al.*, "Linearized Reference Tissue Parametric Imaging Methods: Application to [11C]DASB Positron Emission Tomography Studies of the Serotonin Transporter in Human Brain," *J Cereb Blood Flow Metab,* vol. 23, no. 9, pp. 1096-1112, 2003.

[248] J. Logan *et al.*, "Graphical Analysis of Reversible Radioligand Binding from Time—Activity Measurements Applied to [N-11C-Methyl]-(−)-Cocaine PET Studies in Human Subjects," *Journal of Cerebral Blood Flow & Metabolism,* vol. 10, no. 5, pp. 740-747, 1990.

[249] A. Abi-Dargham *et al.*, "Measurement of Striatal and Extrastriatal Dopamine D1 Receptor Binding Potential With [11C]NNC 112 in Humans: Validation and Reproducibility," *Journal of Cerebral Blood Flow & Metabolism,* vol. 20, no. 2, pp. 225-243, 2000.

[250] M. Slifstein *et al.*, "COMT genotype predicts cortical-limbic D1 receptor availability measured with [11C]NNC112 and PET," *Mol Psychiatry,* vol. 13, no. 8, pp. 821-827, 2008.

[251] A. M. Catafau *et al.*, "Imaging cortical dopamine D(1) receptors using [(11)C]NNC112 and ketanserin blockade of the 5-HT(2A) receptors," *Journal of Cerebral Blood Flow and Metabolism: Official Journal of the International Society of Cerebral Blood Flow and Metabolism,* vol. 30, no. 5, pp. 985-993, 2010.

[252] M. Slifstein, R. F. Suckow, J. A. Javitch, T. Cooper, J. Lieberman, and A. Abi-Dargham, "Characterization of in vivo pharmacokinetic properties of the dopamine D1 receptor agonist DAR-0100A in nonhuman primates using PET with [(11)C] NNC112 and [(11)C] raclopride," *Journal of Cerebral Blood Flow & Metabolism,* vol. 31, no. 1, pp. 293-304, 2011.

[253] J. Ekelund *et al.*, "In Vivo DA D1 Receptor Selectivity of NNC 112 and SCH 23390," *Molecular Imaging and Biology,* vol. 9, no. 3, p. 117, 2007.
[254] T. Siessmeier *et al.*, "Parametric Mapping of Binding in Human Brain of D2 Receptor Ligands of Different Affinities," *Journal of Nuclear Medicine,* vol. 46, no. 6, pp. 964-972, 2005.
[255] C. Y. Sander, B. M. Joseph, W. Hsiao-Ying, C. Ciprian, M. H. Jacob, and R. R. Bruce, "Effects of flow changes on radiotracer binding: Simultaneous measurement of neuroreceptor binding and cerebral blood flow modulation," *Journal of Cerebral Blood Flow & Metabolism,* 2017.
[256] M. Slifstein *et al.*, "Striatal and extrastriatal dopamine release measured with PET and [(18)F]fallypride," *Synapse (New York, N.Y.),* vol. 64, no. 5, pp. 350-362, 2010.
[257] R. M. Kessler *et al.*, "Dopamine D2 Receptor Levels in Striatum, Thalamus, Substantia Nigra, Limbic Regions, and Cortex in Schizophrenic Subjects," *Biological Psychiatry,* vol. 65, no. 12, pp. 1024-1031, 2009.
[258] G. Gründer *et al.*, "The Striatal and Extrastriatal D2/D3 Receptor-Binding Profile of Clozapine in Patients with Schizophrenia," *Neuropsychopharmacology,* Original Article vol. 31, p. 1027, 2005.
[259] I. Vernaleken *et al.*, "Striatal and Extrastriatal D2/D3-Receptor-Binding Properties of Ziprasidone: A Positron Emission Tomography Study With [18F]Fallypride and [11C]Raclopride (D2/D3-Receptor Occupancy of Ziprasidone)," *Journal of Clinical Psychopharmacology,* vol. 28, no. 6, 2008.
[260] I. Vernaleken *et al.*, "Dopamine D2/3 receptor occupancy by quetiapine in striatal and extrastriatal areas," *International Journal of Neuropsychopharmacology,* vol. 13, no. 7, pp. 951-960, 2010.
[261] L. Farde, L. Eriksson, G. Blomquist, and C. Halldin, "Kinetic Analysis of Central [11C]Raclopride Binding to D2-Dopamine Receptors Studied by PET—A Comparison to the Equilibrium Analysis," *Journal of Cerebral Blood Flow & Metabolism,* vol. 9, no. 5, pp. 696-708, 1989.
[262] I. Vernaleken *et al.*, "The applicability of SRTM in [(18)F]fallypride PET investigations: impact of scan durations," *Journal of Cerebral Blood Flow & Metabolism,* vol. 31, no. 9, pp. 1958-1966, 2011.